Modélisation des supraconducteurs de type II : implémentation avec FreeFem

Cyril Tain

To cite this version:

Cyril Tain. Modélisation des supraconducteurs de type II : implémentation avec FreeFem. Analysis of PDEs [math.AP]. Normandie Université, 2023. English. NNT : 2023NORMIR40 . tel-04546205

HAL Id: tel-04546205

https://theses.hal.science/tel-04546205

Submitted on 15 Apr 2024

THÈSE

Pour obtenir le diplôme de doctorat

Spécialité **MATHEMATIQUES**

Préparée au sein de l'**INSA Rouen Normandie**

Modelling of type II superconductors: implementation with FreeFEM.

Présentée et soutenue par

CYRIL TAIN

Thèse soutenue le 21/12/2023

devant le jury composé de :

M. JEAN-GUY CAPUTO	MAITRE DE CONFERENCES DES UNIVERSITES HDR - INSA de Rouen Normandie	Directeur de thèse
M. IONUT DANAILA	PROFESSEUR DES UNIVERSITÉS - Université de Rouen Normandie	Co-directeur de thèse
M. ETIENNE SANDIER	PROFESSEUR DES UNIVERSITÉS - Université Paris-Est - Créteil Val-de-Marne	Président du jury
M. KEVIN BERGER	MAÎTRE DE CONFÉRENCES - Université de Lorraine	Membre
MME LAURA GOZZELINO	ASSOCIATE PROFESSOR - Politecnico di Torino, Italy	Membre
M. NIKOLAOS PROUKAKIS	PROFESSEUR - Newcastle University, Royaume-Uni	Membre
M. MADS PETER SORENSEN	PROFESSEUR - Technical University of Denmark	Rapporteur

Thèse dirigée par **JEAN-GUY CAPUTO** (LABORATOIRE DE MATHEMATIQUES DE L'INSA) et **IONUT DANAILA** (Technical University of Denmark)

Abstract

In this thesis we present four models for type II superconductors: the London model, the time dependent Ginzburg-Landau (TDGL) model, the steady state Ginzburg-Landau model and an Abelian-Higgs model. For the London model a problem with cylindrical symmetry was considered. A hydrodynamic formulation of the problem was established through the introduction of a stream function. Well-posedness of the problem was proved. The external magnetic field was computed for 2D and 3D domains. In 3D, a boundary element method was implemented using a recent feature of FreeFEM. For the TDGL model two codes based on two variational formulations were proposed and tested on classical benchmarks of the literature in 2D and 3D. In the steady state GL model, a Sobolev gradient technique was used to find the equilibrium state. The results were compared with the ones given by the TDGL model. In the Abelian-Higgs model, a 1D finite differences code written in Fortran was developed and tested with the construction of a manufactured system. The model was used to retrieve some of the properties of magnetization of superconductors.

Keywords : superconductor, London, Ginzburg-Landau, Abelian-Higgs, convergence order, mixed scheme, FreeFEM.

MODÉLISATION DES SUPRACONDUCTEURS DE TYPE II. IMPLÉMENTATION AVEC FREEFEM.

Résumé

Nous présentons dans cette étude quatre modèles pour les supraconducteurs de type II : le modèle de London, le modèle de Ginzburg-Landau dépendant du temps (TDGL), le modèle de Ginzburg-Landau stationnaire et un modèle de type Abelian-Higgs. Pour le modèle de London, nous avons étudié un problème à symétrie cylindrique. Nous avons établi une formulation hydrodynamique du modèle grâce à l'introduction d'une fonction courant. Le caractère bien posé du problème a été prouvé. Le champ magnétique extérieur a été calculé pour des domaines 2D et 3D. En 3D une méthode par éléments frontières a été implémentée en utilisant une fonctionalité récente de FreeFEM. Pour le modèle TDGL deux codes fondés sur deux formulations variationnelles ont été implémentées et validées sur des cas tests classiques de la littérature en 2D et 3D. Pour le modèle GL stationnaire, une méthode de gradient de Sobolev a été utilisée pour trouver l'état d'équilibre. Ces résultats ont été comparés avec ceux du modèle TDGL. Pour le modèle Abelian-Higgs un code Fortran différences finies en 1D a été développé et validé par la construction d'un système manufacturé. Ce modèle a été utilisé pour retrouver certaines propriétés de magnétisation des supraconducteurs.

Mots-clefs : supraconducteur, London, Ginzburg-Landau, Abelian-Higgs, ordre de convergence, schéma mixte, FreeFEM.

Acknowledgements

First and foremost I would like to thank my two advisors Jean-Guy Caputo and Ionut Danaila. Jean-Guy Caputo was a great source of inspiration and a wonderful teacher. Ionut Danaila helped me overcoming all the challenges of doing a thesis; it would not have been possible without his constant support.

I was still a high school teacher when Ionut Danaila suggested I should do a PhD on superconductivity. He achieved the tour de force of hiring me as a PhD student. It was like starting from $-\infty$ and reach $+\infty$ he said to me one day.

I gratefully acknowledge the INSA Rouen Normandie for the funding sources. I enjoyed the time I spent at the LMI (Laboratoire de Mathématiques de l'INSA). I deeply appreciated the calm and serenity of my office there.

I wish to address special thanks to my colleagues from LMRS: George Sadaka, Corentin Lothodé, Francky Luddenz. I was lucky to be surrounded by such exceptional colleagues.

I thank my doctoral school EDMIIS. It never failed to bring me financial support each time I was travelling.

Two trips will in particular stay engraved in my memory: the first one in Japan and the second one in Singapore. I thank the Japanese group led by Professor Takashi Sakajo for their warm welcome in Kyoto. It was a genuine pleasure to speak with them and I hope our path will meet again in the future. My special thanks to Professor Weizhu Bao for letting me participate in an international conference at the IMS (Institute of Mathematics of Singapore). I have spent marvellous moments there. It was a rich and fertile experience both from a scientific and a human point of view.

I would also like to address my warmest thanks to Marc Brachet for his outstanding physical expertise and sense of pedagogy. I enjoyed very much my discussions with him. I am also grateful to Pierre-Henri Tournier who has been teaching me many secrets of FreeFEM with an exceptional kindness and patience.

Cyril Tain

Contents

1. Introduction

1.1. Key notions in superconductivity

We introduce here the main features and concepts of superconductivity. Throughout the manuscript we often refer to these notions. All units are SI units.

1.1.1. Meissner effect, penetration depth and coherence length

We begin with two experimental observations.

1. If a conductor is cooled to a given temperature, called *critical temperature* and denoted by T_c, a state of perfect conductivity (zero resistance to electric current) appears. Moreover if an external magnetic field is applied during this cooling (*Field Cooled* process or FC), its properties will be unaffected.
2. If an external field is raised from 0 to some value after the cooling of the superconductor below T_c (*Zero Field Cooling* process or ZFC), then shielding currents (called *supercurrents*) are flowing in the material with zero electrical resistance. This results in the complete expulsion of the magnetic flux as long as the applied field is kept below a critical value denoted by B_c.

Table (1.1) reproduced from en Science (2011) shows for different compounds the critical temperature and the maximum critical field denoted by B_c^{max} (it means that the superconductivity is destroyed beyond this value). $B_c^{max} = B_c$ for type I superconductors only; for type II B_c^{max} is greater than B_c.

We have the following relation (Kittel, 2005):

$$f_n(T) - f_s(T) = \frac{B_c^2(T)}{2\mu_0}, \tag{1.1}$$

where f_n (resp. f_s) is the free energy per unit volume of the normal phase (resp. superconducting phase). The difference $f_n(T) - f_s(T)$ is called the *condensation energy*. We also have an empirical relation for B_c:

$$B_c(T) \approx B_c(0)\left(1 - \left(\frac{T}{T_c}\right)^2\right). \tag{1.2}$$

The complete expulsion of flux is called the *Meissner effect*. It was first discovered by Meissner and Ochsenfeld in 1933. In 1935 Fritz and Heinz London brothers explained this phenomena and thus founded the eponymous model. Basically it states that the supercurrent density $\mathbf{J}_s$ is directly proportional to the vector magnetic potential:

$$\mathbf{A} = -\mu_0\lambda^2\mathbf{J}_s, \tag{1.3}$$

Family	Examples	T_c (K)	Type	B_c^{max} (T)	ξ (nm)	λ (nm)
Metals	Hg	4.1K	I	up to 0.1T	$\approx$ 1000	65
Alloys	Nb_3Sn	18K	II	24T	3	65
Diborure de magnesium	MgB_2	39K	II	up to 50 T	15	50
Fullerenes	K_3C_{60}	40K	II	up to 30T	3	240
Cuprate	$YBa_2Cu_3O_7$	92K	II	115T	0.5 to 2.5	150 to 500
Pnictide	$Ba(Fe_{1-x}Co_x)_2As_2$	56K	II	60T	a few nm	A few hundred

Table 1.1. *Main quantities characterizing some superconductors.*

where

$$\begin{aligned} \mathbf{B} &= \nabla \times \mathbf{A}, \\ \lambda^2 &= \frac{\epsilon_0 mc^2}{ne^2}, \end{aligned} \tag{1.4}$$

with ϵ_0, μ_0 being the vacuum permittivity and permeability respectively; c the velocity of light; n is the density of electrons, m and e the mass and charge of the electron respectively. Taking the curl on both sides of (1.3) and using $(1.4)_1$ we deduce the London equation:

$$\mathbf{B} = -\mu_0 \lambda^2 \nabla \times \mathbf{J}_s. \tag{1.5}$$

Formula (1.5) accounts for the Meissner effect in the sense that it does not allow a uniform field **B** to be a solution.

Experimental values for λ in pure metals appear to differ considerably from formula $(1.4)_2$. Pippard and Bragg (1953) introduced a new length called *coherence length* and denoted ξ to explain the experiments. Ginzburg-Landau theory of superconductivity provides the following expression for ξ:

$$\xi = \frac{\hbar}{\sqrt{2m(-\alpha)}}, \tag{1.6}$$

where α is a negative coefficient which appear in the expression of the energy density of a superconductor (see Section 3.1, Eq. (3.1)).

Remark 1.1.1. *Formula (1.6) actually coincides with Pippard results only for pure metals and well below T_c (for more details see Tinkham (2004), chapter 4).*

In superconductivity the London length and the coherence length play a fundamental role in classifying the types of superconductors (I or II). The central concept of the wall energy is presented in the next section.

1.1.2. Intermediate state and wall energy

In a superconductor we find two phases, *superconducting* (denoted by S in the sequel) and *normal* (denoted by N). The boundary between the two is called the *wall interface*. The phase N corresponds to the penetration of the magnetic flux and the absence of supercurrents ($n = 0$); whereas the phase S corresponds to the presence of supercurrents ($n > 0$) and absence of magnetic flux. Figure 1.1 shows this interface schematically.

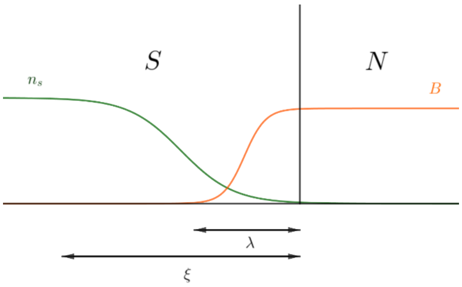

Figure 1.1. *Wall interface between the S (superconducting) and N (normal) phase.*

The concept of wall energy and the role played by the London length λ and the coherence length ξ were first explained by Ginzburg and Landau (1950). We outline below their ideas. At the interface, n cannot actually fall abruptly to 0 but vanishes within a distance of the order of the coherence length ξ. The same goes for the magnetic flux B within a distance of the order of the London length λ. This results in the following wall energy contribution of the interface to the free energy of the whole system

$$\mathcal{F}_{\text{interface}} = \frac{B_c^2}{2\mu_0}\left(\xi - \lambda\right). \tag{1.7}$$

As a result, when $\xi > \lambda$, the wall energy is positive and the superconductor tends to minimize the surface between N and S; large N domains mix with S domains in an intricate manner (Fig. 1.2 left panel). The superconductor is named *type I*.

When $\xi < \lambda$ the wall energy is negative and the superconductor tends to multiply interfaces. We observe well-ordered flux tubes: these tubes are called *vortices* and the vortex pattern is called a *flux-line lattice* (Fig. 1.2 right panel). The superconductor is named *type II*. The amount of magnetic flux in each tube is the same: it is called the *quantum flux* or *fluxoid* or *fluxon* and is denoted by ϕ_0. We have

$$\phi_0 = \frac{h}{2e} \approx 2.0678 \times 10^{-15}\ \mathrm{T\ m}^2. \tag{1.8}$$

The magnetic field generated by Earth is 5×10^{-6} T and ϕ_0 is very small in comparison.

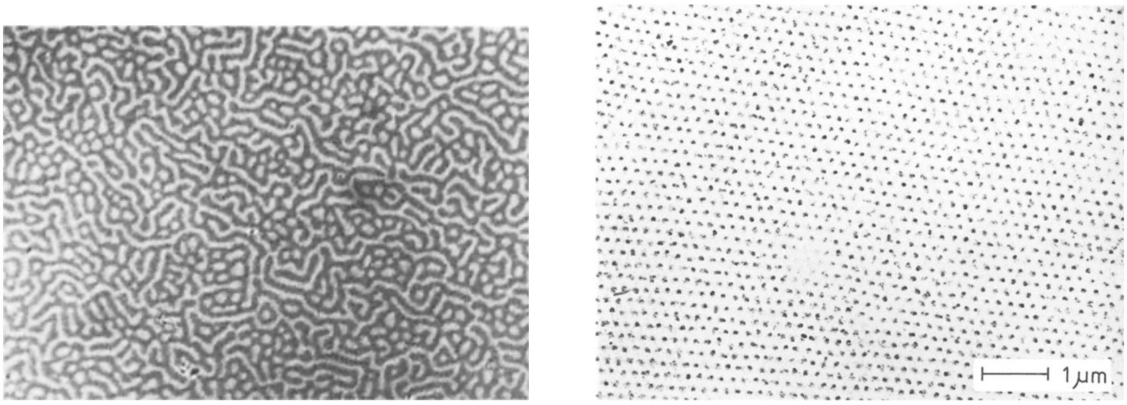

Figure 1.2. *Intermediate state in a Pb film in a perpendicular magnetic field (left). Flux-line lattice in Nb in a perpendicular magnetic field (right).*

1.1.3. Special case of superconductors of type II

Formula (1.7) is actually qualitative. A quantitative calculation conducted originally by Ginzburg and Landau (1950) shows that the separation between type I and type II is given by the line $\kappa = \dfrac{1}{\sqrt{2}}$ where $\kappa := \dfrac{\lambda(T)}{\xi(T)}$. κ is dimensionless and is called the *Ginzburg-Landau parameter*.

In type I superconductors, in the case of ZFC, the expulsion of the flux is total until the critical value B_c is reached. At B_c a first order phase transition occurs, i.e. the flux enters completely the sample and destroys superconductivity. The magnetisation curve $\mathbf{M} = \dfrac{1}{\mu_0}(\mathbf{B} - \mathbf{B}_{\text{applied}})$ shown in Fig. 1.3 (left) reflects this behaviour.

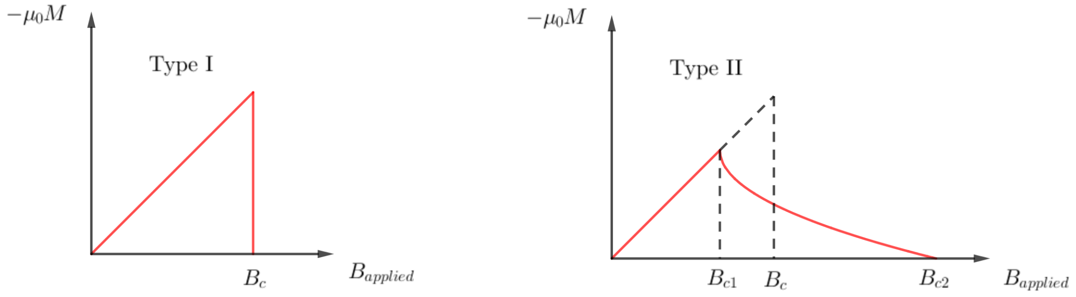

Figure 1.3. *Magnetisation curve of a type I superconductor (left) and of a type II superconductor (right).*

In type II superconductors there exists a first critical field denoted by $B_{c1} < B_c$ where the magnetic flux starts to enter the domain. However superconductivity remains in the sense that currents are still flowing with no resistance. The phase transition at B_{c1} is called second order. The superconductivity is eventually destroyed when the applied field reaches a second critical field denoted B_{c2} that may be well above B_{c1} (it corresponds to the value B_c^{max} reported in Tab. 1.1). The magnetisation curve of a type II superconductor is shown in Fig. 1.3 (right).

An interesting consequence of the London theory is the quantization of the magnetic flux through a superconducting ring. The effect is described in a very elegant manner in Feynman et al. (1971). From quantum mechanics, we can describe the superconducting particle by a complex wave function $\psi(\mathbf{r}) = \rho(\mathbf{r})e^{i\theta(\mathbf{r})}$. The velocity $\mathbf{v}_s$ of the particle is defined by

$$\mathbf{v}_s := \frac{1}{m_s}(\hbar\nabla\theta - e_s\mathbf{A}) := \frac{1}{e_s\rho^2}|\mathbf{J}_s|, \tag{1.9}$$

where e_s (resp. m_s) denotes the charge (resp. the mass) of the superconducting charge carrier. e_s (resp m_s) are *a priori* different from the electron charge e (resp. mass m). It is actually a current of probabilistic nature, fundamentally different from the electrical current which induces a resistance. It is known from London theory (see Chapter 2) that currents flow only on the surface of the material within a typical distance of λ. As a result, if we integrate (1.9) on a path Γ (see Fig. 1.4) passing through the centre of each cross-section (on Γ we have $J_s = 0$ if the sample is sufficiently thick) we find

$$\int_\Gamma \nabla\theta \cdot \mathbf{ds} = 2\pi q = \frac{e_s}{\hbar}\Phi, \tag{1.10}$$

where Φ denotes the total amount of flux passing through the ring and q is an integer. The formula (1.10) was stated by London and Onsager with e_s the charge of the electron. The first experimental evidence by Deaver Jr and Fairbank (1961) showed that e_s is actually twice the charge of the electron: in superconductivity, the current is due to a pair of electrons called a *Cooper pair*.

Feynman (1998) has introduced a model for superconductivity. In Appendix A.1 of this thesis we present this model.

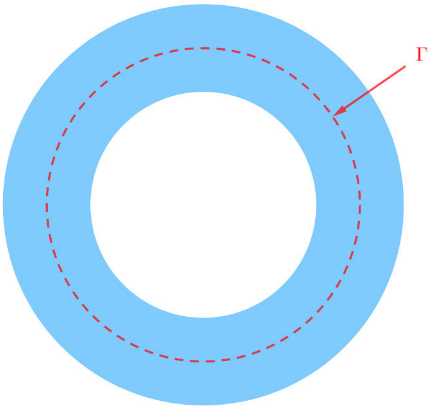

Figure 1.4. *Superconducting ring.*

Remark 1.1.2. *By convention the mass m_s is taken equal to $2m$ (see Tinkham (2004) for a discussion). Hence, if we denote by n_s the density of the superconducting particles, we have $n = 2n_s$ and we see that*

$$\frac{m_s}{n_s e_s^2} = \frac{m}{ne^2}. \tag{1.11}$$

As a consequence, the formula $(1.4)_2$ for λ is invariant considering electrons or superconducting particles.

1.1.4. Classification of models

We can classify the various models in three categories: phenomenological models, semi-phenomenological models, and microscopic ones.

Phenomenological models need experiments to adjust their parameters so that it fits each particular case. They rely on their simplicity and good agreement with experimental data. In particular, they are reliable tools to describe the behaviour of high T_c superconductors (e.g. cuprates or pnictides), for which no microscopic theory is available. They were pioneered by Bean in the 60's (Bean, 1964). He introduced a phenomenological law for describing supercurrents inside the material. Basically it states that the values for $\mathbf{J}_s$ have to be $\pm J_c$ or 0. J_c is adjusted experimentally and is called the *critical current density*. After the work of Bean, many refinements of the theory have been done by suggesting other laws for the supercurrent or assuming dependencies of J_c with the local magnetic flux $\mathbf{B}$ or the temperature. For a review of these models see Ainslie and Fujishiro (2019). The general name for these models is *critical state models*. They are studied for describing the macroscopic features of a superconductor. Of particular interest for applications is the so called *trapped flux*, i.e. the amount of the magnetic flux that a superconductor can store without losing the perfect conductivity property. The trapped flux property is the basis for applications such as magnetic levitation (Bernstein and Noudem, 2020) or MRI (Magnetic Resonance Imagery). However such models cannot resolve fluxoids or the dynamics of N/S phases. In that case we need to use semi-phenomenological models.

Semi-phenomenological models stem from quantum mechanics. London model and its generalizations (see Huebener (2001) for a review) describe accurately the Meissner effect and superconductors of type II in the limit $\lambda \gg \xi$. Ginzburg-Landau (GL) models were pioneered by Ginzburg and Landau (1950). Their model was an extension to superconductors of Landau's theory of second order phase transition. Later in 1959, Gorkov (1959) was able to derive the GL model from first principles of quantum mechanics but within a limited range of temperature near T_c. Several models have been derived to include time dynamics (Gorkov and Eliashburg, 1968; Schmid, 1966; Caroli and Maki, 1967; Maki, 1969). However the theory is valid under highly restricted conditions: the temperature has to be close to T_c where the order parameter ψ is small; moreover, time and spatial variations of ψ should not be too slow. For a detailed discussion of these issues we refer the reader to Huebener (2001) or Cyrot (1973). In this manuscript we consider the set of equations established by Gorkov and Eliashburg (1968) for a gapless superconductor which can be obtained by adding for example magnetic impurities.

The only microscopic theory up to this date is the BCS theory (Bardeen et al., 1957). It explains superconductivity for materials with low T_c such as metals or alloys but fails to explain high T_c superconductivity in cuprates or pnictides, for example. Basically it states that the electrons arrange in pairs called *Cooper pairs*. We do not detail the theory and refer to Tinkham (2004) for an introduction or de Gennes (1966) for a complete description.

1.2. State of art in numerical simulations

In this section, we provide references for the London model, the TDGL model and the steady state GL model. The cited articles are related to the material found in this thesis. Du (2005) gives a review of numerical techniques used to solve GL models.

For the London theory, analytic solutions are known for the infinite slab or cylinder in parallel $\mathbf{H}$, and for the sphere (see Brandt and Mikitik (2000) and the references cited therein). Fiolhais and Essén (2014) have reported exact solutions for the infinite cylinder in transversal $\mathbf{H}$. Caputo et al. (2013) have made 2D simulations of the London equations for a cylindrical problem: a similar approach is used in this thesis. Prozorov (2021) have made a quantitative description of the magnetic susceptibility of the circular cylinder of finite length; the author also provides simulations of the 3D London equations using a finer mesh near the edges of the superconductor; the computations are made for various London lengths. A time dependent approach of the London model with moving vortices has also been developed (Prozorov and Kogan, 2018; Kogan and Nakagawa, 2022).

For the TDGL model, early simulations used finite difference methods. In particular, the link variable method has proved successful (Frahm et al., 1991; Kato et al., 1993; Gropp et al., 1996; Winiecki and Adams, 2002). These methods are still used extensively by the physical community. Barba-Ortega et al. (2010) have reported 2D simulations in circular geometries; they take into account material properties by using De Gennes boundary conditions (de Gennes, 1966). Barba-Ortega et al. (2015) have made 3D simulations in a rectangular geometry. Sadovskyy et al. (2015) have reported a technological breakthrough. The authors have simulated the TDGL model in a square of size $4096\xi_0^2$, which is roughly the size of an experimental 2D superconducting film. They use an implicit Crank-Nicolson scheme in time, and suppose $\kappa \gg 1$, so that the field is supposed homogenous. Subsequently, Sadovskyy et al. (2016) have computed critical currents (maximum electric current a superconductor can maintain without resistance) in 3D domain of macroscopic size; in particular, they showed the influence of defects on vortex dynamics. Willa et al. (2017) show impressive 3D pinning landscapes. Progress have been made as regards the numerical properties of the TDGL model in its simplest form (without defect and with homogenous boundary conditions). Richardson et al. (2004), using a finite difference scheme, have studied the influence of the size of the mesh on TDGL numerical solutions. Besides finite difference methods, finite element methods have been investigated, mostly by the mathematical community. Algorithms for the temporal gauge have been proposed by Du (1994a), Mu and Huang (1998), Yang (2014). To deal with some numerical issues (in particular abnormal values at corners), Gao and Sun (2015) have proposed a mixed finite element scheme (for more on these techniques see Boffi et al. (2013)). The method has proved successful (Gao and Sun, 2016; Gao, 2017). Li and Zhang (2017) have reported another approach using the Helmholtz decomposition of the vector potential; this method apply in 2D only, but allows the use of Lagrange finite elements. Recently, Gao and Xie (2023) have proposed an algorithm to solve the TDGL system under the Coulomb gauge. Hong et al. (2023) have used the Newton method to solve the TDGL model under the temporal gauge; the authors use a GMRES algorithm and build a time independent preconditioner. Finally, TDGL model can be solved by finite element solvers such as COMSOL (Zimmerman, 2006). Alstrom et al. (2011) have reported a now classical benchmark: a disk with a boundary defect. This example leads to numerical issues that prompted the finding of other methods such as the mixed finite element formulation.

The steady state GL model have been tackled by the mathematical community. In particular Sobolev gradient methods have been developed (Neuberger, 2009). These methods have been used to find critical points of the GL energy (Neuberger and Renka, 1998, 2000, 2003; Kazemi, 2008). Kazemi and Renka (2013) provide a Sobolev gradient algorithm using a trust region method.

1.3. Presentation of the free software FreeFEM

FreeFEM (Hecht, 2012) is a 2D and 3D partial differential equations solver. It offers an easy way to write variational formulations of physical problems. The unknown fields (e.g. the density, the vector potential, the magnetic field, currents, ...) are approximated by *finite elements* (FEs). FreeFEM provides a large choice of FEs. In the next section we introduce Lagrange FE, Raviart-Thomas FE and Nedelec FE.

1.3.1. Examples of finite elements

Our goal here is to give some intuition about the FEs used in the thesis. For a complete exposition of the theory, we refer the reader for example to Ciarlet (2002). We denote the computational domain by Ω. Let $\mathcal{T}_h$ a triangulation of Ω, h being the typical size of a triangle in 2D (or a tetrahedron in 3D). Let v be a physical quantity to be approximated on $\mathcal{T}_h$. Given a choice of a FE, v can be decomposed in a discrete space, often denoted by V_h, called the *interpolation space*. Let $(\phi)_i$ a basis of V_h, then we have

$$v = \sum_{i=1}^{N} v_i \phi_i, \tag{1.12}$$

where N is the dimension of V_h called the number of *degrees of freedom*.

If v is a scalar field, Lagrange FE can be used. In the case of linear Lagrange FE denoted by P^1, we have

$$v_i = v(a_i), \tag{1.13}$$

where (a_i) are the vertices of each triangle in 2D or tetrahedron in 3D (see Fig. 1.5). Hence v is approximated by a linear function on each triangle or tetrahedron. In the case of piecewise quadratic Lagrange FE, v is approximated by a polynomial of degree 2 on each triangle or tetrahedron.

If v is a vector field, we can use Raviart-Thomas FE or Nedelec FE. In the case of Raviart-Thomas FE of degree 0 denoted by $RT0$, we have

$$v_i = \int_{F_i} \mathbf{v} \cdot \mathbf{n}_i, \tag{1.14}$$

where $\mathbf{n}_i$ is the normal of the edge (respectively face) F_i of a triangle (respectively tetrahedron). In the case of Nedelec FE of degree 0 denoted by $N0$, we have

$$v_i = \int_{e_i} \mathbf{v} \cdot \mathbf{t}_i, \tag{1.15}$$

where $\mathbf{t}_i$ is the tangent of the edge e_i of a triangle in 2D or a tetrahedron in 3D.

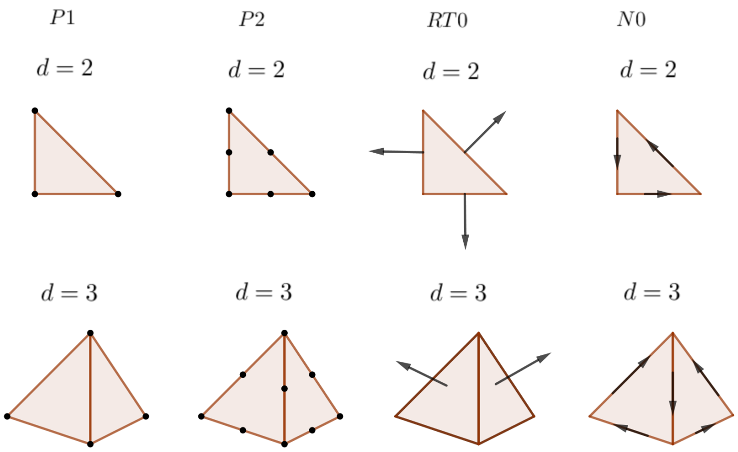

Figure 1.5. *From left to right: Lagrange FEs P^1, P^2, Raviart-Thomas $RT0$, and Nedelec $N0$ in 2D and in 3D.*

In the next section, we show how to solve a Poisson problem with FreeFEM and illustrate the use of Raviart-Thomas FE.

1.3.2. Two ways to solve a Poisson problem

We want to solve the following Poisson problem

$$\begin{aligned} &-\Delta u = f \quad \text{in } \Omega, \\ &u = 0 \quad \text{on } \Gamma_1 \cup \Gamma_2 \cup \Gamma_3, \\ &\nabla u \cdot \mathbf{n} = 0 \quad \text{on } \Gamma_4. \end{aligned} \tag{1.16}$$

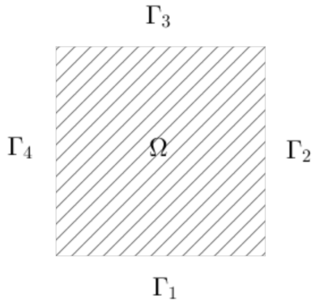

Figure 1.6. *Computational domain* Ω

The variational formulation of (1.16) is obtained by multiplying by a test function v which vanishes on $\Gamma_1 \cup \Gamma_2 \cup \Gamma_3$; then we integrate by parts. Noticing that the surface term vanishes, we obtain the following variational formulation:

$$\begin{aligned} &\text{find } u \in V \text{ such that,} \\ &\int_\Omega \nabla u \cdot \nabla v - \int_\Omega f v = 0 \quad \forall v \in V, \end{aligned} \tag{1.17}$$

where $V = \{u \in H^1(\Omega) \text{ such that } u = 0 \text{ on } \Gamma_1 \cup \Gamma_2 \cup \Gamma_3\}$.

The FreeFEM syntax to solve the problem (1.17) is

Listing 1.1 `Poisson equation with Lagrange FE`

```
int M = 100; // mesh size
func f = 4.; // right hand side

mesh Th = square(M,M,[2*x-1, 2*y-1]); // build the mesh
fespace Vh(Th,P1); // Lagrange FE space
Vh u,v; // FE unknown and test function

problem laplace2d(u,v) =
  int2d(Th)(dx(u)*dx(v)+dy(u)*dy(v))
  + int2d(Th)(-f*v)
  + on(1,2,3,u=0); // variational formulation

laplace2d; // solve the problem

plot(u,wait=1,fill = 1,value = true); // plot the solution
```

In physics, the interesting quantity is often the gradient of the unknown ∇u. Hence the idea of a *mixed* form of problem (1.16). The variable $\boldsymbol{\sigma} := \nabla u$ is introduced as a supplementary unknown. Problem (1.16) becomes:

$$\begin{aligned} &-\operatorname{div}(\boldsymbol{\sigma}) = f \quad \text{in } \Omega, \\ &\boldsymbol{\sigma} = \nabla u \quad \text{in } \Omega, \\ &u = 0 \quad \text{on } \Gamma_1 \cup \Gamma_2 \cup \Gamma_3, \\ &\boldsymbol{\sigma} \cdot \mathbf{n} = 0 \quad \text{on } \Gamma_4. \end{aligned} \tag{1.18}$$

The variational formulation of (1.18) is

$$\begin{aligned}&\text{Find } \boldsymbol{\sigma} \in H(\operatorname{div}) \text{ and } u \in L^2 \text{ such that,}\\ &\int_\Omega \operatorname{div} \boldsymbol{\sigma} v + \int_\Omega f v = 0 \quad \forall v \in L^2,\\ &\int_\Omega \boldsymbol{\sigma} \cdot \boldsymbol{\chi} + \int_\Omega u \cdot \operatorname{div} \boldsymbol{\chi} = 0 \quad \forall \boldsymbol{\chi} \in H(\operatorname{div}) \text{ such that } \boldsymbol{\chi} \cdot \mathbf{n} = 0 \text{ on } \Gamma_4,\end{aligned} \tag{1.19}$$

where $H(\operatorname{div}) := \{u \in L^2(\Omega), \operatorname{div} u \in L^2(\Omega)\}$.

The FreeFEM syntax to solve the variational problem (1.19) is

Listing 1.2 `Poisson equation with Raviart-Thomas FE`

```
int M = 100; // mesh size
func f = 4.; // right hand side

mesh Th = square(M,M,[2*x-1, 2*y-1]); // build the mesh

fespace Vh(Th,RT0); // Raviart-Thomas FE space
fespace Ph(Th,P0);

Vh [sigma,sigmay],[chi,chiy];
Ph u,v;

problem laplaceMixte([sigma,sigmay,u],[chi,chiy,v]) =
  int2d(Th)( sigma*chi + sigmay*chiy + u*(dx(chi)+dy(chiy)) + (dx(sigma)+dy(sigmay))*v )
  + int2d(Th)(f*v)
  + on(4,sigma=0,sigmay=0); // variational formulation

laplaceMixte; // solve the problem

plot([sigma,sigmay],coef=0.1,wait=1,value=true);
plot(u,wait=1,fill = 1,value = true);  // plot the solution
```

Figure 1.7 shows the solution of problem (1.16) computed with the two methods.

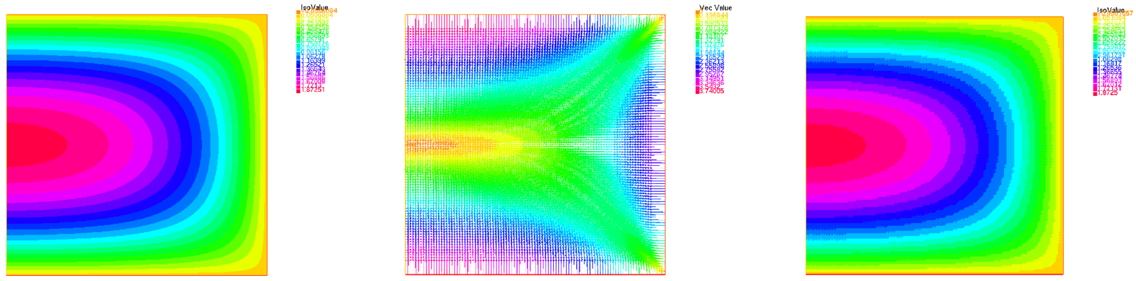

Figure 1.7. *Solution of the Poisson problem* (1.16) *with the standard formulation* (1.17) *(left), the mixed formulation* (1.19) *(middle: $\boldsymbol{\sigma}$, right: u).*

Remark 1.3.1. *Raviart-Thomas FEs are used to deal with the boundary condition $\boldsymbol{\sigma} \cdot \boldsymbol{n} = 0$. The transposition of this condition with FreeFEM is simply* `on(4,sigma=0,sigmay=0)`*.*

1.4. Outline of the thesis

Our goal is to study different models for type II superconductors and build efficient codes and algorithms written with FreeFEM.

Chapter 2 is devoted to the London theory. We focus here on a superconductor in the Meissner state. We derive the model from the energy as originally done in de Gennes (1966). We study the problem of existence and uniqueness of the model in 2D and 3D. To this purpose a stream function is introduced as done in Danaila et al. (2021) in the context of vortex ring theory. We present numerical results in 2D and 3D. We end the chapter by considering an unbounded domain in 3D. We exploit a recent feature of FreeFEM (boundary elements) to couple the interior and the exterior of the superconductor.

Chapter 3 is devoted to the time dependent Ginzburg-Landau theory (TDGL). The TDGL model in its simplest form is considered (no defects and homogenous boundary conditions). An important characteristic of the model is the gauge invariance. We define gauges in the TDGL framework and in particular the ω-gauge which is extensively used in the last section. We outline several mathematical results about the well-posedness of the model; we mainly rely on the pioneering work by Du (1994b). Our goal is to familiarize the reader with the variational formulation of the model. We describe two numerical schemes based on two variational formulations and give the main ingredients to implement them with FreeFEM. Many examples, both in 2D and 3D, are treated. We close the chapter by a convergence study in the general framework of the ω-gauge.

Chapter 4 is devoted to the steady state GL model. The earliest mathematical results on superconductors were obtained using this model. We present mathematical properties of the steady state equations. We solve numerically the equations by using a steepest descent algorithm based on a Sobolev gradient. We finally show results in 2D and draw a comparison with the TDGL model.

Chapter 5 is devoted to an Abelian-Higgs model originally introduced by Nielsen and Olesen (1973). We derive the equations of motion and a 1D model. We construct a manufactured problem to demonstrate the validity of our finite difference code. Our goal is to recover some classical features of magnetisation of superconductors.

In Appendix A, we first establish formal links between three equations: the Feynman's point of view from Feynman (1998), the Ginzburg-Landau equation for ψ and the Gross-Pitaevskii (GP) equation. The GP equation is used to model superfluids (Pitaevskii and Stringari, 2003); vortex pattern can be observed in a very similar manner as in type II superconductors (Yarmchuk et al., 1979; Tilley, 2019). Then, as a complement, we show that the weighted Sobolev space $H^1(\omega)$ introduced in Chapter 2 is a Hilbert space.

2. London model

The London model was established by Fritz and Heinz London in 1935. It is valid when the coherence length ξ is much smaller than the London penetration depth λ. In transition metals or intermetallic compound (Wb3Sn, V3Ga), London theory applies well in weak fields.

The London model explains the Meissner effect, i.e. the total expulsion of the magnetic flux from the interior of the superconductor. This effect is accompanied by a demagnetizing field. Our goal is to capture numerically the magnetic field outside the sample.

2.1. Derivation of the London model

The presentation below follows de Gennes (1966). The free energy $\mathcal{F}$ of a sample can be written as

$$\begin{aligned} \mathcal{F} &= \int_{\mathcal{S}} F_s \mathbf{dr} + E_{kin} + E_{mag}, \\ E_{kin} &= \int_{\mathcal{S}} \frac{1}{2} m v_s^2 n_s \mathbf{dr}, \\ E_{mag} &= \int_{\mathcal{S}} \frac{1}{2\mu_0} B^2 \mathbf{dr}, \end{aligned} \tag{2.1}$$

where F_s denotes the energy density of the superconducting phase, E_{kin} the kinetic energy density due to currents, E_{mag} the magnetic energy density; $\mathbf{v}_s$ is the velocity and n_s the density of the electrons. By definition of the Maxwell-Ampere equation in quasi-static approximation

$$\nabla \times \mathbf{B} = \mu_0 \mathbf{J}_s. \tag{2.2}$$

and since $\mathbf{J}_s = n_s e \mathbf{v}_s$, we deduce that

$$\mathcal{F} = E_0 + \frac{1}{2\mu_0} \int_{\mathcal{S}} \left[B^2 + \lambda^2 |\nabla \times \mathbf{B}|^2 \right] \mathbf{dr}. \tag{2.3}$$

We have $E_0 = \int_{\mathcal{S}} F_s \mathbf{dr}$ and $\lambda = \left(\frac{m}{\mu_0 n_s e^2} \right)^{\frac{1}{2}}$ is the London length.

Now, we introduce a small variation $\delta\mathbf{B}$:

$$\begin{aligned} \delta B^2 &= 2\mathbf{B} \cdot \delta\mathbf{B}, \\ \delta |\nabla \times \mathbf{B}|^2 &= 2\nabla \times \delta\mathbf{B} \cdot \nabla \times \mathbf{B}. \end{aligned} \tag{2.4}$$

Then

$$\delta\mathcal{F} = \frac{1}{\mu_0} \int_{\mathcal{S}} \left[\mathbf{B} + \lambda^2 \nabla \times \nabla \times \mathbf{B} \right] \cdot \delta\mathbf{B}\mathbf{dr} = 0. \tag{2.5}$$

Finally we obtain the equation for the magnetic field **B** in the domain $\mathcal{S}$ of the superconductor

$$\mathbf{B} + \lambda^2 \nabla \times \nabla \times \mathbf{B} = 0 \quad \text{in } \mathcal{S}. \tag{2.6}$$

Let us get some intuition about (2.6). We consider a semi-infinite superconductor occupying the half space $x > 0$ as in Fig. 2.1.

- First case: $\mathbf{B} \parallel (Ox)$.

  From $\operatorname{div} \mathbf{B} = 0$ we deduce $\dfrac{\partial B}{\partial x} = 0$, then $B(x)$ is constant. Since the current $\mathbf{J}_s$ is proportional to $\nabla \times \mathbf{B}$, hence there is no current inside $\mathcal{S}$. This case actually cannot happen.

- Second case: $\mathbf{B} \parallel (Oz)$.

  Equation (2.6) reads

  $$\frac{\mathrm{d}^2 B}{\mathrm{d}z^2} = \frac{1}{\lambda^2} B, \tag{2.7}$$

  and the solution is

  $$B(z) = B(0) \exp\left(-\frac{z}{\lambda}\right). \tag{2.8}$$

  Figure 2.2 illustrates this case. Eq. (2.8) explains the Meissner effect. It corresponds to an exponential decay of the magnetic flux inside the superconductor within a length scale equal to the London length λ.

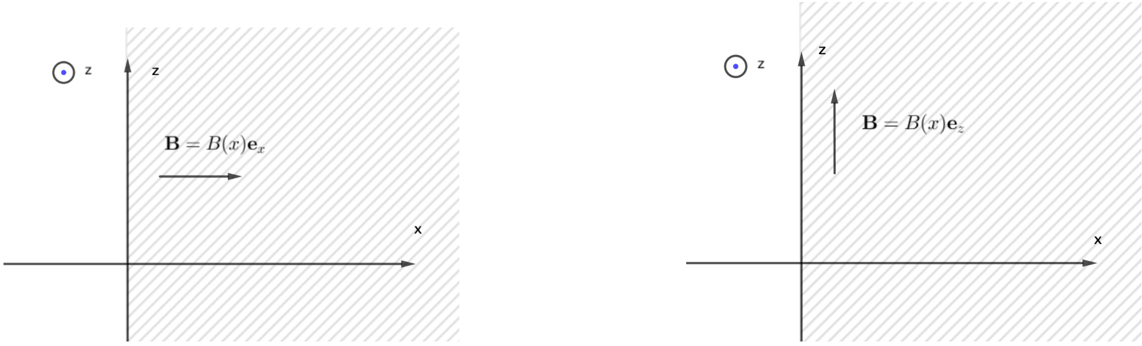

Figure 2.1. *Case **B** $\parallel (Ox)$ (left) and case **B** $\parallel (Oz)$ (right).*

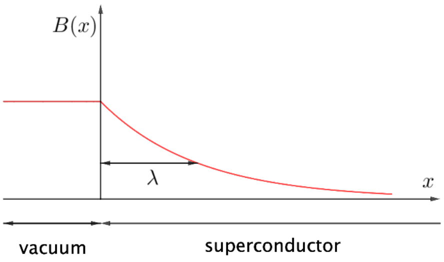

Figure 2.2. *Amplitude B of the magnetic field in the case **B** $\parallel (Oz)$.*

We can formulate (2.6) using the vector potential $\mathbf{A}$ such that $\nabla \times \mathbf{A} = \mathbf{B}$. We have

$$\nabla \times \mathbf{A} + \lambda^2 \nabla \times (\nabla \times \nabla \times \mathbf{A}) = \mathbf{0}. \tag{2.9}$$

From (2.9) the rotational of $\mathbf{A} + \lambda^2 \nabla \times \nabla \times \mathbf{A}$ vanishes. If we make the Coulomb gauge choice $\operatorname{div} \mathbf{A} = 0$ then the divergence of $\mathbf{A} + \lambda^2 \nabla \times \nabla \times \mathbf{A}$ also vanishes. We conclude that

$$\mathbf{A} + \lambda^2 \nabla \times \nabla \times \mathbf{A} = \mathbf{0}. \tag{2.10}$$

Moreover since $\nabla \times \nabla \times \mathbf{A} = \nabla \operatorname{div} \mathbf{A} - \Delta \mathbf{A} = -\Delta \mathbf{A}$, we deduce that

$$-\Delta \mathbf{A} + \frac{1}{\lambda^2} \mathbf{A} = \mathbf{0}. \tag{2.11}$$

Equation (2.11) is valid for a constant and uniform applied magnetic field. In the general case, we need to consider the Gibbs free energy $\mathcal{G} := \mathcal{F} - \int_{\mathcal{S}} \mathbf{B} \cdot \mathbf{H}$, where H is called the *thermodynamic field*. It is known (de Gennes, 1966) that $\mathbf{H}$ can be identified with the external field produced for instance by a coil. Considering (2.2) and (2.3) we have

$$\mathcal{G} = E_0 + \frac{1}{2\mu_0} \int_{\mathcal{S}} \left[B^2 + \lambda^2 |\nabla \times \mathbf{B}|^2 \right] \mathrm{d}\mathbf{r} - \int_{\mathcal{S}} \mathbf{B} \cdot \mathbf{H}. \tag{2.12}$$

From (2.10) and (2.2) we have $\mathbf{J}_s = -\frac{1}{\mu_0 \lambda^2} \mathbf{A}$ and

$$\mathcal{G} = E_0' + \frac{1}{2\mu_0} \int_{\mathcal{S}} \left[|\nabla \times \mathbf{A} - \mu_0 \mathbf{H}|^2 + \frac{A^2}{\lambda^2} \right] \mathrm{d}\mathbf{r}. \tag{2.13}$$

Varying this expression with respect to $\mathbf{A}$ gives

$$\int_{\mathcal{S}} \left[\nabla \times (\mathbf{A} - \mu_0 \mathbf{H}) \cdot \nabla \times \delta \mathbf{A} + \frac{1}{\lambda^2} \mathbf{A} \cdot \delta \mathbf{A} \right] \mathrm{d}\mathbf{r} = 0. \tag{2.14}$$

After integrating by parts we obtain

$$\int_{\mathcal{S}} \left[\nabla \times (\nabla \times \mathbf{A} - \mu_0 \mathbf{H}) + \frac{1}{\lambda^2} \mathbf{A} \right] \cdot \delta \mathbf{A} \mathrm{d}\mathbf{r} = 0. \tag{2.15}$$

Assuming the Coulomb gauge, we end up with the following equation for $\mathbf{A}$ in $\mathcal{S}$:

$$-\Delta \mathbf{A} + \frac{1}{\lambda^2} \mathbf{A} = \mu_0 \nabla \times \mathbf{H}. \tag{2.16}$$

Since outside $\mathcal{S}$ we have that $\nabla \times \mathbf{B} = \mu_0 \nabla \times \mathbf{H}$ and denoting by $\mathbb{1} := \mathbb{1}_{\mathcal{S}}$ the indicator function of $\mathcal{S}$ we can generalize (2.16) for both the interior and exterior:

$$-\Delta \mathbf{A} + \mathbb{1} \frac{1}{\lambda^2} \mathbf{A} = \mu_0 \nabla \times \mathbf{H}. \tag{2.17}$$

2.2. Existence and uniqueness of solutions in a cylindrical problem

2.2.1. 3D case

In this section we consider a 3D problem of geometry shown in Fig. 2.3. An external cylinder $\mathcal{O}$ of radius R_{max} and half height Z_{max} encloses a cylindrical superconductor of radius R_s and half height Z_s. We suppose the sample is in the Meissner state and obeys the London model (2.17). We assume cylindrical symmetry and thus $\mathbf{A} = A\mathbf{e}_\theta$. A uniform and static magnetic field $\mathbf{B}_0 = \mathrm{B}_0\mathbf{e}_z$ is applied. Moreover we assume that $R_{max} \gg R_s$ and $Z_{max} \gg Z_s$, so that the magnetic field on $\partial\mathcal{O}$ is equal to $\mathbf{B}_0$. From $\nabla \times \mathbf{A} = \mathbf{B}$ and applying Stokes formula on a disk D of radius $r = R_{max}$ as in Fig. 2.4 we have

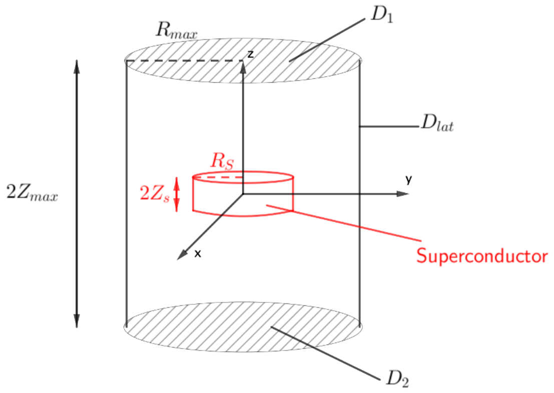

Figure 2.3. *Three dimensional domain with cylindrical symmetry.*

$$\int_D \mathbf{B} \cdot \mathbf{n}\mathbf{da} = A|_{r=R_{max}} \times 2\pi R_{max}. \tag{2.18}$$

Moreover the divergence of the magnetic field is zero so that the integral on the left hand side in (2.18) does not depend on the disk chosen. Hence, if we choose $D = D_1$ for example, we obtain $\int_D \mathbf{B} \cdot \mathbf{n}\mathbf{da} = \mathrm{B}_0 4\pi R_{max}^2$ since the field is uniform on D_1. Finally we deduce the value of A on D_{lat}

$$A|_{D_{lat}} = \mathrm{B}_0 \frac{R_{max}}{2}. \tag{2.19}$$

We also easily get that $A|_{D_1 \cup D_2} = \mathrm{B}_0 \frac{r}{2}$.

In conclusion the London model amounts to solve the following non-homogenous Dirichlet bound-

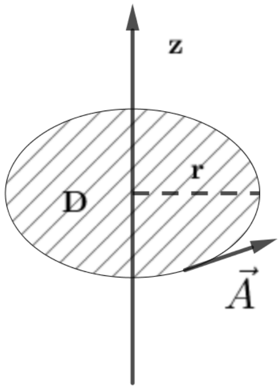

Figure 2.4. *Disk of radius r in the (xOy) plane.*

ary value problem:

$$\begin{cases} -\Delta \mathbf{A} + \mathbb{1}\dfrac{\mathbf{A}}{\lambda^2} = 0 \quad \text{in } \mathcal{O}, \\ A|_{D_1 \cup D_2} = \mathrm{B}_0 \dfrac{r}{2}, \\ A|_{D_{lat}} = \mathrm{B}_0 \dfrac{R_{max}}{2}. \end{cases} \tag{2.20}$$

Equation (2.20) can be rewritten in Cartesian coordinates

$$\begin{cases} -\Delta \mathbf{A} + \mathbb{1}\dfrac{\mathbf{A}}{\lambda^2} = 0 \quad \text{in } \mathcal{O}, \\ A_x = -\mathrm{B}_0 \dfrac{y}{2} \quad \text{on } \partial\mathcal{O}, \\ A_y = \mathrm{B}_0 \dfrac{x}{2} \quad \text{on } \partial\mathcal{O}, \\ A_z = 0 \quad \text{on } \partial\mathcal{O}. \end{cases} \tag{2.21}$$

The variational formulation of (2.21) is

$$\begin{cases} \text{Find } A_i \in H^1(\mathcal{O}) \text{ such that,} \\ \displaystyle\int_{\mathcal{O}} \nabla A_i \cdot \nabla v + \int_{\mathcal{O}} \mathbb{1}\frac{A_i}{\lambda^2} v = 0 \quad \forall v \text{ in } H_0^1(\mathcal{O}). \end{cases} \tag{2.22}$$

It is known from classical results (Cioranescu et al., 2018) that (2.22) has a unique solution.

2.2.2. 2D case

In this section we study the problem (2.20) in a radial cross-section of the cylinder $\mathcal{O}$ denoted by $\Omega :=]0, R_{max}[\times]0, Z_{max}[$. Since $\mathbf{A} = A\mathbf{e}_\theta$ we know that in cylindrical coordinates

$$\Delta \mathbf{A} = \Delta A - \frac{A}{r^2}, \tag{2.23}$$

where $\Delta A = \dfrac{\partial^2 A}{\partial z^2} + \dfrac{\partial^2 A}{\partial r^2} + \dfrac{1}{r}\dfrac{\partial A}{\partial r}$. Therefore problem (2.20) in Ω becomes:

$$\begin{cases} -\Delta A + \dfrac{A}{r^2} + \mathbb{1}\dfrac{1}{\lambda^2} A = 0, \\ A|_{\partial\Omega} = \mathrm{B}_0 \dfrac{r}{2}. \end{cases} \tag{2.24}$$

Remark 2.2.1. *In the previous section, we have seen that* $A = B_0 \frac{r}{2}$ *far from the superconductor. However in problem* (2.24) *we have made the stronger hypothesis that* $A(z, 0) = 0$ *for all* z*, i.e.* A *vanishes on the (Oz) axis. This is actually a direct consequence of* (2.18) *applied to an arbitrary disk perpendicular to the* z *axis; we have*

$$\int_D \boldsymbol{B} \cdot \boldsymbol{n} \boldsymbol{da} = A(r, z) 2\pi r. \tag{2.25}$$

Moreover the left hand side in (2.25) *is bounded by* $\pi r^2 sup_D B$*. Hence*

$$|A(z, r)| \leq \frac{r}{2} sup_D B. \tag{2.26}$$

We conclude that $A \underset{r \to 0}{\longrightarrow} 0$.

Equation (2.24) corresponds to the London model of a cylindrical superconductor. It can actually be cast in a simpler form using a the stream function $\Psi = rA$ as is done in Danaila et al. (2021) in the context of vortex ring theory.

Observing that $\dfrac{\partial}{\partial r}\left(\dfrac{1}{r}\dfrac{\partial(Ar)}{\partial r}\right) = \dfrac{\partial A}{\partial r}\left(\dfrac{\partial}{\partial r} + \dfrac{A}{r}\right) = \dfrac{\partial^2 A}{\partial r^2} + \dfrac{1}{r}\dfrac{\partial A}{\partial r} - \dfrac{A}{r^2}$, we have

$$\Delta A - \frac{A}{r^2} = \frac{\partial}{\partial z}\left(\frac{1}{r}\frac{\partial(Ar)}{\partial z}\right) + \frac{\partial}{\partial r}\left(\frac{1}{r}\frac{\partial(Ar)}{\partial r}\right). \tag{2.27}$$

Setting $\Psi = rA$, (2.24) has the form

$$\begin{cases} -\bar{\nabla} \cdot (\dfrac{1}{r}\bar{\nabla}\Psi) + \mathbb{1}\dfrac{1}{\lambda^2}\dfrac{\Psi}{r} = 0 \quad \text{in } \Omega, \\ \Psi = \mathrm{B}_0 \dfrac{r^2}{2} \quad \text{on } \partial\Omega, \end{cases} \tag{2.28}$$

where $\bar{\nabla} = \begin{pmatrix} \dfrac{\partial}{\partial x} \\ \dfrac{\partial}{\partial y} \end{pmatrix}$ denotes the 2D nabla operator. If we make the change of variable

$$\tilde{\Psi} = \Psi - \mathrm{B}_0 \frac{r^2}{2}, \tag{2.29}$$

we see that $\tilde{\Psi}$ verifies the following homogenous Dirichlet problem:

$$\begin{cases} -\bar{\nabla} \cdot (\dfrac{1}{r}\bar{\nabla}\Psi) + \mathbb{1}\dfrac{1}{\lambda^2}\dfrac{\Psi}{r} = f, \\ \Psi = 0, \quad \text{on } \partial\Omega, \end{cases} \tag{2.30}$$

where $f = \mathbb{1}\frac{\mathrm{B}_0}{\lambda^2}\frac{r^2}{2}$. In the sequel we study existence and uniqueness for the system (2.30) where f is a function in $L^2(\Omega)$.

Remark 2.2.2. *we could have also formulate a homogenous Dirichlet problem for the vector potential. If we make the change of variable*

$$\tilde{A} = A - B_0\frac{r}{2}, \tag{2.31}$$

we see that (2.24) *becomes*

$$\begin{cases} -\Delta\tilde{A} + \tilde{A}\left(\mathbb{1}\frac{1}{\lambda^2} + \frac{1}{r^2}\right) = \frac{B_0}{2}\left(\mathbb{1}\frac{1}{\lambda^2} - \frac{1}{r}\right), \\ \tilde{A}|_{\partial\Omega} = 0. \end{cases} \tag{2.32}$$

The right hand side of (2.32) *is not in* L^1. *This prevents the use of the classical Lax-Milgram theory. However, the model* (2.30) *with the stream function can be solved with the Lax-Milgram theorem as we show below.*

We consider two different domains Ω. The first, $\Omega =]\varepsilon, R_{max}[\times]0, Z_{max}[$ is the simplest since the singularity introduced by the axis is avoided. The other $\Omega =]0, R_{max}[\times]0, Z_{max}[$ is more difficult since classical results do not apply.

- Case of Fig. 2.5 : $\Omega =]\varepsilon, R_{max}[\times]0, Z_{max}[$.

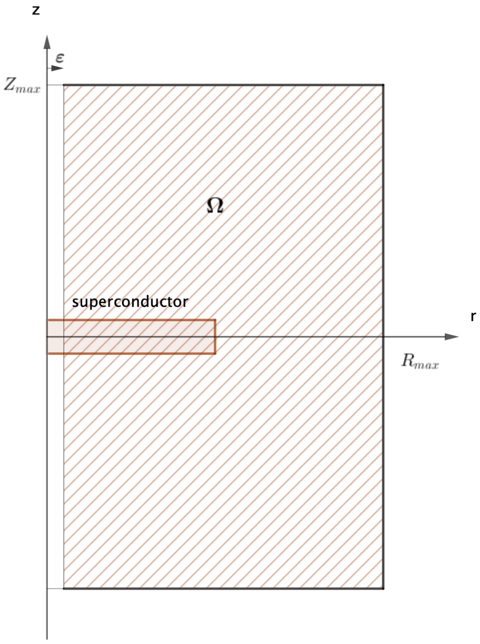

Figure 2.5. *Domain* $\Omega =]\varepsilon, R_{max}[\times] - Z_{max}, Z_{max}[$.

The variational formulation corresponding to (2.30) is

$$\begin{cases} \text{find } \Psi \in H_0^1(\Omega) \text{ such that,} \\ \forall v \in D(\Omega), \int_\Omega \frac{1}{r}\bar{\nabla}\Psi\bar{\nabla}v + \int_\Omega \mathbb{1}\frac{1}{\lambda^2}\frac{\Psi}{r}v = \int_\Omega fv. \end{cases} \tag{2.33}$$

We remark that $-\bar{\nabla}\cdot(\frac{1}{r}\bar{\nabla}\Psi) = -\bar{\nabla}\cdot(M\bar{\nabla}\Psi)$ where M is the matrix $\begin{pmatrix} \frac{1}{r} & 0 \\ 0 & \frac{1}{r} \end{pmatrix}$.

If λ is a vector in $\mathbb{R}^2$, we observe that $A\lambda\cdot\lambda \geq \frac{1}{R_{max}}|\lambda|^2$ and $|A\lambda| \leq \frac{1}{\varepsilon}|\lambda|$. As a consequence, we can use the Lax-Milgram theorem (Cioranescu et al., 2018) and the above problem admits a unique solution.

- Case of fig (2.6): $\Omega =]0, R_{max}[\times] - Z_{max}, Z_{max}[$.

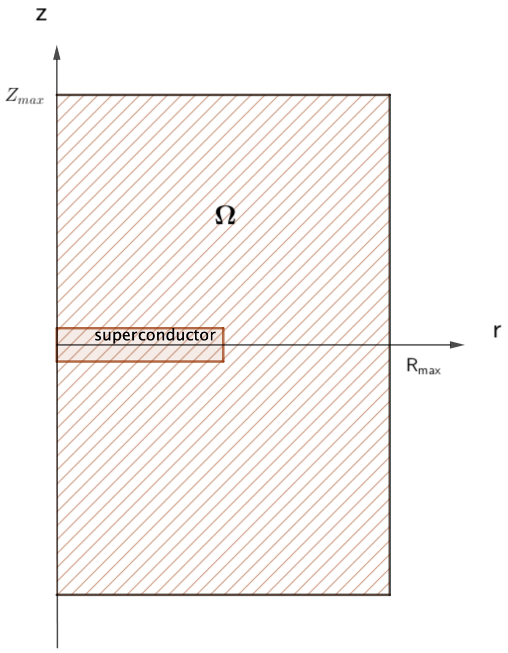

Figure 2.6. *Domain* $\Omega =]0, R_{max}[\times] - Z_{max}, Z_{max}[$.

One notice that the weight $\frac{1}{r}$ is not bounded in Ω. To give a meaning to integrals in (2.30) we require that $\frac{1}{r}\Psi$ and $\frac{1}{r}\bar{\nabla}\Psi$ belong to L^2; or equivalently that Ψ and $\bar{\nabla}\Psi$ belong to L^2_ω defined as

$$L^2_\omega := \left\{ u \text{ mesurable } \Omega \to \mathbb{R}, \int_\Omega |u|^2\omega < \infty \right\}, \tag{2.34}$$

where $\omega = \frac{1}{r}$ is called a *weight* (Rudin, 1987).

Firstly one can see easily that $L^2_\omega \subset L^1_{loc}$; indeed let B a ball compactly included in Ω and u in L^2_ω; then by Hölder inequality

$$\int_B u = \int_B u\frac{1}{\sqrt{\omega}}\sqrt{\omega} \leq \int_B u^2\omega \times \int_B \frac{1}{\omega} < \infty. \tag{2.35}$$

As a result we can define weak derivatives of any function in L^2_ω. Hence the following definition makes sense

$$H^1(\omega) := \{u \in L^2_\omega, \nabla u \in L^2_\omega\}. \tag{2.36}$$

$H^1(\omega)$ is called a *weighted Sobolev space*. We show in Appendix A.2 that it is a Hilbert space for the scalar product

$$(\Phi, \Psi)_{H^1(\omega)} := \int_\Omega \frac{1}{r}\Phi\Psi + \int_\Omega \frac{1}{r}\nabla\Phi \cdot \nabla\Psi. \tag{2.37}$$

The associated norm is

$$||\Psi||_{H^1(\omega)} := \left(||\psi||^2_{L^2_\omega} + ||\bar{\nabla}\psi||^2_{L^2_\omega}\right)^{\frac{1}{2}}. \tag{2.38}$$

We denote $H^1_0(\omega)$ the closure of compactly supported functions in $H^1(\omega)$ for the norm (2.38). It is also a Hilbert space since it is a closed subspace of $H^1(\omega)$.

We are now ready to define the variational formulation associated to (2.30):

$$\left\{\begin{array}{l} \text{find } \Psi \in H^1_0(\omega) \text{ such that,} \\ \displaystyle\int_\Omega \frac{1}{r}\bar{\nabla}\Psi\bar{\nabla}v + \int_\Omega \mathbb{1}\frac{1}{\lambda^2}\frac{\Psi}{r}v = \int_\Omega fv \quad \forall v \in H^1_0(\omega). \end{array}\right. \tag{2.39}$$

To show that problem (2.39) has a unique solution, we apply the classical Lax-Milgram theory.

Let a denote the bilinear form on $H^1_0(\omega)$ given by

$$a(\Psi, v) = \int_\Omega \frac{1}{r}\bar{\nabla}\Psi\bar{\nabla}v + \int_\Omega \mathbb{1}\frac{1}{\lambda^2}\frac{\Psi}{r}v. \tag{2.40}$$

Applying Cauchy-Schwarz inequality and the definition (2.38) we have

$$\begin{aligned} |a(\Psi, v)| &\leq ||\bar{\nabla}\Psi||_{L^2_\omega}||\bar{\nabla}v||_{L^2_\omega} + \frac{1}{\lambda^2}||\Psi||_{L^2_\omega}||v||_{L^2_\omega} \\ &\leq \max(1, \frac{1}{\lambda^2})||\Psi||_{H^1_0(\omega)}||v||_{H^1_0(\omega)}. \end{aligned} \tag{2.41}$$

To prove $H^1_0(\omega)$-ellipticity we need the following Poincaré inequality in $H^1_0(\omega)$:

Proposition 2.2.3. *There exists a constant K which depends only on Ω such that for all Ψ in $H^1_0(\omega)$*

$$||\Psi||_{L^2_\omega} \leq K\|\bar{\nabla}\Psi\|_{L^2_\omega}. \tag{2.42}$$

Using (2.42) we have

$$||\Psi||^2_{H^1_0(\omega)} = ||\Psi||^2_{L^2_\omega} + ||\bar{\nabla}\Psi||^2_{L^2_\omega} \leq (1 + K^2)||\bar{\nabla}\Psi||^2_{L^2_\omega}. \tag{2.43}$$

From inequality (2.43) we get

$$|a(\Psi, \Psi)| \geq ||\bar{\nabla}\Psi||^2_{L^2_\omega} \geq \frac{1}{1 + K^2}||\Psi||^2_{H^1_0(\omega)}, \tag{2.44}$$

which means that a is $H^1_0(\omega)$-elliptic.

We now prove the Poincaré inequality (2.42).

Proof. Let u in $\mathcal{D}(\Omega)$. From the fundamental theorem of integration we have:

$$u(r,z) = \int_0^z \frac{\partial u}{\partial z}(r,t)\mathrm{d}t. \tag{2.45}$$

From Cauchy-Schwartz inequality, we obtain:

$$\begin{aligned}\left|\int_0^z \frac{\partial u}{\partial z}(r,t)\mathrm{d}t\right|^2 &\leq \left(\int_0^z \left|\frac{\partial u}{\partial z}(r,t)\right| \mathrm{d}t\right)^2 \\ &\leq \int_0^{Z_{max}} \mathrm{d}t \int_0^{Z_{max}} \left|\frac{\partial u}{\partial z}(r,t)\right|^2 \mathrm{d}t \\ &\leq Z_{max} \int_0^{Z_{max}} \left|\frac{\partial u}{\partial z}(r,t)\right|^2 \mathrm{d}t.\end{aligned} \tag{2.46}$$

We deduce:

$$|u(r,z)|^2 \leq Z_{max} \int_0^{Z_{max}} \left|\frac{\partial u}{\partial z}(r,t)\right|^2 \mathrm{d}t. \tag{2.47}$$

The bound on the right being independent with z. Then we multiply (2.47) by ω and integrate over Ω to obtain:

$$\begin{aligned}&\int_\Omega \omega\,|u| \leq \int_0^{R_{max}} \int_0^{Z_{max}} \left[\omega Z_{max} \int_0^{Z_{max}} \left|\frac{\partial u}{\partial z}(r,t)\right|^2 \mathrm{d}t\right] \mathrm{d}r\mathrm{d}z \\ &\leq Z_{max}^2 \int_\Omega \left[\omega \left|\frac{\partial u}{\partial z}(r,t)\right|^2\right] \mathrm{d}r\mathrm{d}t \\ &\leq Z_{max}^2 \int_\Omega \omega\,|\nabla u|^2 .\end{aligned} \tag{2.48}$$

We have proved that for all $u \in \mathcal{D}(\Omega)$ there exist a generic constant C independent of u such that

$$||u||_{L^2_\omega} \leq C||\nabla u||_{L^2_\omega}. \tag{2.49}$$

Since by definition $\mathcal{D}(\Omega)$ is dense in $H^1_0(\omega)$ the proof is complete. □

Remark 2.2.4. *The Poincaré inequality* (2.42) *happens to be true for a general class of weight* ω *belonging to a class called the Muckenhoupt class and denoted by* A_2 *(Fabes et al., 1982). It implies in particular that* $\int_B \omega$ *has to be bounded independently of a closed ball* $B \subset \Omega$*. In our case* $\omega = \dfrac{1}{r}$ *does not verify the latter condition, hence classical results on weighted Sobolev spaces (Turesson, 2000) do not apply. What makes the Poincaré inequality works in this simple case is that* ω *depends only on one variable.*

2.3. An integral formulation for the stream function in the London 2D stationary problem

In this section we establish an integral formula for the stream function Ψ solution of (2.30). The equation to solve is

$$-\bar{\nabla} \cdot \left(\frac{1}{r}\bar{\nabla}\psi\right) + \mathbb{1}\frac{1}{\lambda^2}\frac{\psi}{r} = -\mathbb{1}\frac{\mathrm{B}_0}{\lambda^2}\frac{r}{2} \quad \text{in } \Omega. \tag{2.50}$$

It can be rewritten

$$\left(\frac{\partial^2}{\partial r^2}+\frac{1}{r}\frac{\partial}{\partial r}-\frac{1}{r^2}+\frac{\partial^2}{\partial z^2}\right)\left(\frac{\psi}{r}\right)=\mathbb{1}\frac{\mathrm{B}_0}{\lambda^2}\frac{r}{2}-\mathbb{1}\frac{1}{\lambda^2}\frac{\psi}{r}. \tag{2.51}$$

Here we consider the cylindrical superconductor of Fig. 2.3 as a superposition of ”Circular Vortex Filament” (CVF). This terminology is borrowed from the vortex dynamics (Danaila et al., 2021). A CVF is characterized by its radius $\rho_s \in [0, R_s]$ and its altitude $\zeta_s \in [-Z_s, Z_s]$ (see Fig. 2.7).

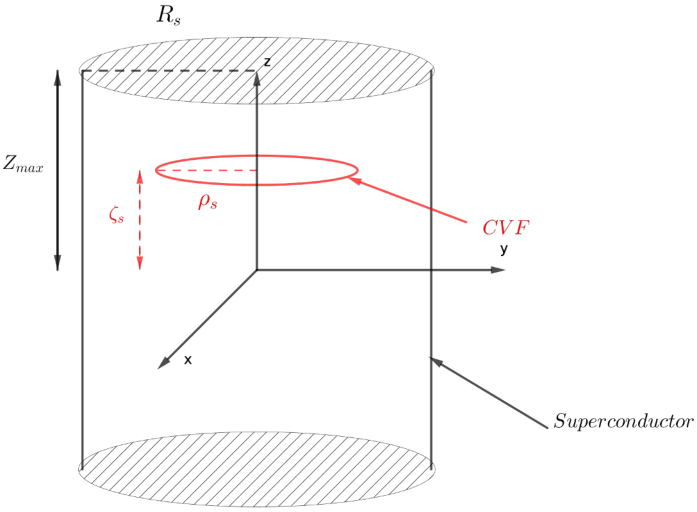

Figure 2.7. *The Circular Vortex Filament*

Equation (2.51) for a CVF is

$$\left(\frac{\partial^2}{\partial r^2}+\frac{1}{r}\frac{\partial}{\partial r}-\frac{1}{r^2}+\frac{\partial^2}{\partial z^2}\right)\left(\frac{\psi}{r}\right)=\delta(r-\rho_s)\delta(|z|-\zeta_s)\left[\frac{\mathrm{B}_0\rho_s}{2\lambda^2}-\frac{1}{\lambda^2}\frac{\psi(\rho_s,\zeta_s)}{\rho_s}\right]. \tag{2.52}$$

Equation (2.52) is identical to the stream function of a CVF in vortex theory (Danaila et al., 2021). It is known that

$$\psi_{CVF}(r,z)=\Gamma_0(\rho_s,\zeta_s)\frac{\sqrt{r\rho_s}}{2\pi}\left[\left(\frac{2}{\kappa}-\kappa\right)K(\kappa)-\frac{2}{\kappa}E(\kappa)\right], \tag{2.53}$$

where $\Gamma_0(\rho_s,\zeta_s)=\frac{\mathrm{B}_0\rho_s}{2\lambda^2}-\frac{1}{\lambda^2}\frac{\psi(\rho_s,\zeta_s)}{\rho_s}$ is the strength of the vortex and $\kappa=\frac{4r\rho_s}{z^2+(r+\rho_s)^2}$. $E(k)$ and $K(k)$ are elliptic integrals of the first and second kind respectively (see Eqs. (2.70)).

By superposition we deduce a formula for the solution of (2.51):

$$\psi(r,z)=\int_{\rho_s\in[0,R_s],\zeta_s\in[0,Z_s]}\Gamma_0(\rho_s,\zeta_s)\left[\left(\frac{2}{\kappa}-\kappa\right)K(\kappa)-\frac{2}{\kappa}E(\kappa)\right]. \tag{2.54}$$

2.4. Numerical results

In this section we model a cylindrical superconductor using the London model (2.16). In the first paragraph we study the 2D case from two different points of view. We compute the induced magnetic field either with the vector potential or by a stream function. We show the agreement between the two methods. The first point of view has been treated by Caputo et al. (2013), the second is original. We conclude the paragraph by considering a non homogenous applied field created by a coil. In the third paragraph we study the 3D case. First we compute the magnetic field inside a bounded external box; then we consider the more general case of an unbounded external domain; to this purpose we introduce a boundary element method. Finally, we compare the results with the bounded case.

2.4.1. 2D study

We consider a cylindrical superconductor enclosed in a cylindrical box as in Fig. 2.3. The goal of this section is to compute the vector potential $\mathbf{A} = A\mathbf{e}_\theta$ solution of (2.24). Due to the symmetry of the problem, it is sufficient to consider the domain $\Omega = [0, R_{max}] \times [-Z_{max}, Z_{max}]$ shown in Fig 2.8. We denote $\mathcal{S} = [0, R_s] \times [-Z_s, Z_s]$ the superconducting domain.

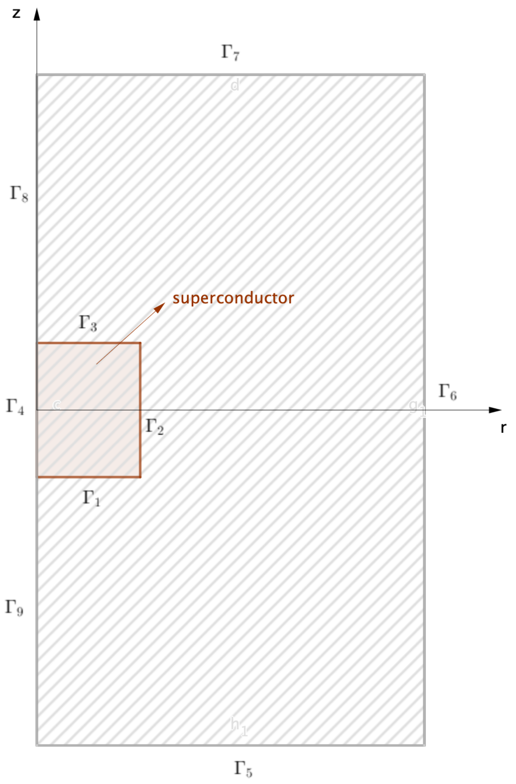

Figure 2.8. *Computational domain* Ω *and boundaries* Γ_i, $i = 1..9$.

The problem to solve is

$$\begin{cases} -\Delta A + \dfrac{A}{r^2} + \mathbb{1}\dfrac{1}{\lambda^2}A = 0 \text{ in } \Omega, \\ A = 0 \text{ on } \cup_{i\in\{4,8,9\}} \Gamma_i, \\ A = \mathrm{B}_0\dfrac{r}{2} \text{ on } \cup_{i\in\{5,6,7\}} \Gamma_i. \end{cases} \tag{2.55}$$

In the sequel we use the following values for parameters (in SI units):

$$\begin{cases} R_{max} = 37.5 \times 10^{-3}, Z_{max} = 32.5 \times 10^{-3}, \\ R_s = 1 \times 10^{-2}, Z_s = 6.5 \times 10^{-3}, \\ \lambda = 1.6 \times 10^{-7}, \\ \mathrm{B}_0 = 1, \\ M = 40. \end{cases} \tag{2.56}$$

where M refers to the number of nodes on the length R_{max}.

Variational formulation and discretization

We use a finite element method to discretize numerically the problem (2.55). To this aim we need to work in relevant normed spaces called *Sobolev spaces*. Then we write the variational formulation of the problem (for a precise definition see Cioranescu et al. (2018)).

We use the following definitions for the Sobolev spaces:

$$\begin{aligned} &H^1(\Omega) := \{u \in L_2(\Omega), \nabla u \in L_2(\Omega)\}, \\ &H_0^1(\Omega) := \{u \in L_2(\Omega), \nabla u \in L_2(\Omega), u = 0 \text{ on } \partial\Omega\}, \\ &V := \{u \in H^1(\Omega), u = 0 \text{ on } \Gamma_4 \cup \Gamma_8 \cup \Gamma_6 \cup \Gamma_7\}. \end{aligned} \tag{2.57}$$

To find the variational formulation, we multiply Eq. (2.55) by a function called a *test* function v and integrate by parts; we end up with an integral formulation of the problem with only first order derivatives. The variational form of (2.55) is to find A in $H^1(\Omega)$ such that for all v in V

$$\int_\Omega \bar{\nabla} A \cdot \bar{\nabla} v - \int_\Omega \frac{1}{r}\frac{\partial A}{\partial r} v + \int_\Omega \frac{1}{r^2} A v + \int_\Omega \mathbb{1}\frac{1}{\lambda^2} A v = 0, \tag{2.58}$$

where $\bar{\nabla} = \begin{pmatrix} \dfrac{\partial}{\partial x} \\ \dfrac{\partial}{\partial y} \end{pmatrix}$ denotes the 2D nabla operator.

To discretize the variational formulation (2.58) we use the standard piecewise quadratic Lagrange FE P^2. FreeFEM allows a straightforward coding of (2.58):

```
varf Vpot(A,v)  = int2d(Th)(dx(A)*dx(v)+dy(A)*dy(v)
                - int2d(Th)(dx(A)*v/x)
          + int2d(Th)(A*v/x^2)
          + int2d(Th)(Indicatrix/lambda^2*A*v)
          + on(4, 8, 9, 5, 6, 7, A = 0);
```

The magnetic field $\mathbf{B}(B_r, B_z, B_\theta)$ is computed by the formula $\mathbf{B} = \nabla \times \mathbf{A}$ which, in cylindrical coordinates, becomes

$$\begin{cases} B_r = -\dfrac{\partial A}{\partial z}, \\ B_z = \dfrac{1}{r}\dfrac{\partial (rA)}{\partial r} = \dfrac{\partial A}{\partial r} + \dfrac{A}{r}, \\ B_\theta = 0. \end{cases} \tag{2.59}$$

The implementation of (2.59) with FreeFEM is made by a variational formulation:

```
//===== Br component
varf champBr(Br,v) = int2d(Th)(Br*v)
  + on(4,5,6,7,8,9, Br=0);
varf Brbc(Br,v) =  int2d(Th)(-1.*dy(A)*v)
  + on(4,5,6,7,8,9, Br=0); // right hand side
//===== Bz component
varf champBz(Bz,v) = int2d(Th)(Bz*v)
  + on(5,6,7,Bz=B0);
varf Bzbc(Bz,v) =  int2d(Th)(A*v/x)
  + int2d(Th)(dx(A)*v)
  + on(5,6,7,Bz=B0); // right hand side
```

Figures 2.10-2.11 show the vector potential and the magnetic field computed on the uniform mesh Fig. 2.9. We observe an enhancement of the field near the edge Γ_2: it is the classical demagnetization effect due on the one hand to the divergencefree nature of the magnetic field and, on the other hand to its expulsion from the bulk of the superconductor. Similar effects are observed near the edges of an obstacle immersed in a potential flow with zero viscosity.

In Fig. 2.10 we observe a sharp variation of the magnetic field near Γ_2. To better capture the solution we use mesh adaptivity, a standard function in FreeFEM (Hecht, 1998). The mesh is refined where a specified function varies sharply. In this case the function is B_z. Figure 2.11 shows the adapted mesh and the magnetic field on the new mesh. The values of the magnetic field near the edges are computed more accurately. Indeed, The mesh adaptation strategy is to compute the best mesh with respect to a given numerical error (Loseille and Alauzet, 2011). Moreover this optimization process keeps the number of triangles approximately constant. Hence the new linear system to solve is of the same size than the one with a uniform mesh.

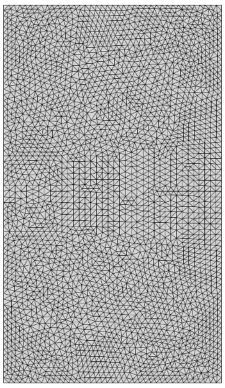

Figure 2.9. *London model in 2D. Uniform mesh.*

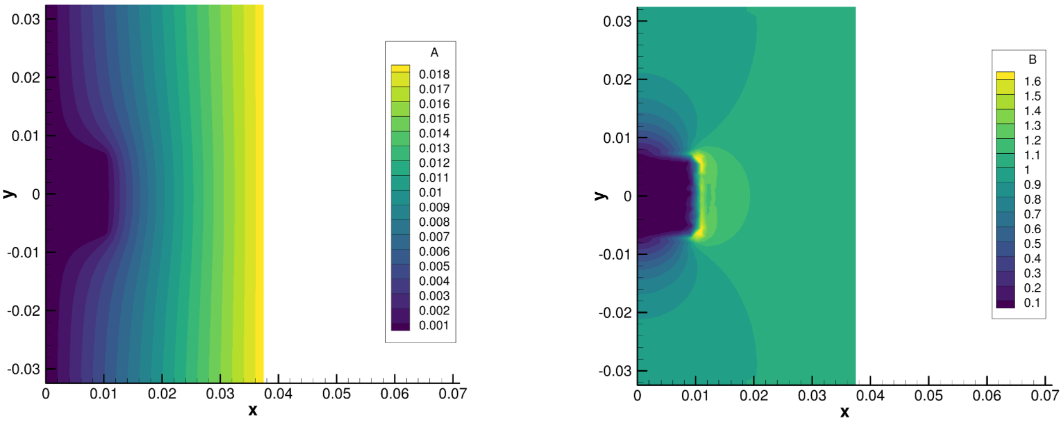

Figure 2.10. *London model in 2D. Stationary solution for the vector potential (left), for the magnetic field* $||\boldsymbol{B}||$ *(right).*

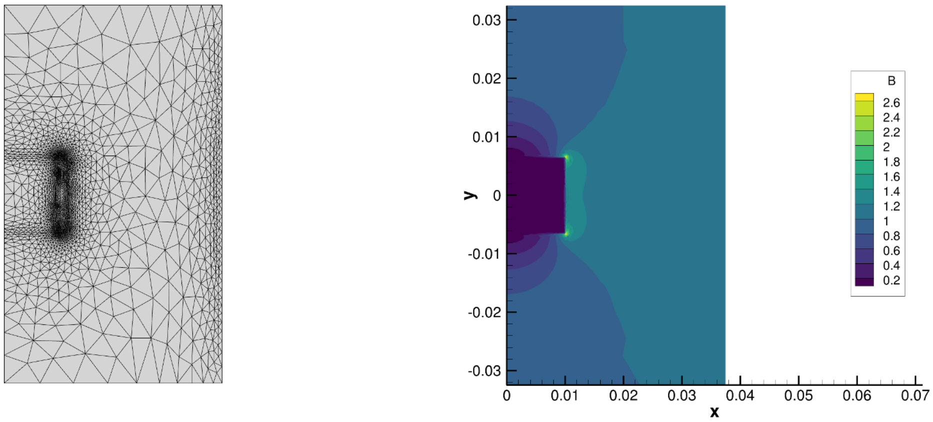

Figure 2.11. *London model in 2D. Mesh after anisotropic adaptation (left), magnetic field on the adapted mesh* $||\boldsymbol{B}||$ *(right).*

Alternative formulation using a stream function

In this section we study the alternative formulation (2.30) of problem (2.55). The system to solve is

$$\begin{cases} -\bar{\nabla}\cdot\left(\frac{1}{r}\bar{\nabla}\Psi\right)+\mathbb{1}\frac{1}{\lambda^2}\frac{\Psi}{r} = -\mathbb{1}\frac{\mathrm{B}_0}{\lambda^2}\frac{r}{2} \text{ in } \Omega,\\ \Psi = 0 \text{ on } \partial\Omega. \end{cases} \tag{2.60}$$

The variational formulation of (2.60) is to find Ψ in $H^1(\Omega)$ such that for all v in $H_0^1(\Omega)$ we have

$$\int_\Omega \frac{1}{r}\bar{\nabla}\Psi \cdot \bar{\nabla} v + \int_\Omega \mathbb{1}\frac{1}{\lambda^2}\frac{\Psi}{r}v + \int_\Omega \mathbb{1}\frac{\mathrm{B}_0}{\lambda^2}\frac{r}{2}v = 0. \tag{2.61}$$

Implementing (2.61) with FreeFEM gives

```
varf VPsi(Psi,v)= int2d(Th)((dx(Psi)*dx(v)+dy(Psi)*dy(v))/x)
  +int2d(Th)(Indicatrix/lambda^2*Psi/x*v)
  +on(4,5,6,7,8,9,Psi=0);  // matrix
varf VrhsPsi(Psi,v)= - int2d(Th)(Indicatrix/lambda^2*B0*x/2*v)
  + on(4,5,6,7,8,9,Psi=0); // right hand side
```

From the change of variables (2.29), we have $A = \dfrac{1}{r}\left(\Psi + \mathrm{B}_0\dfrac{r}{2}\right)$; hence the magnetic field is deduced from formula (2.59)

$$\left\{\begin{aligned} B_r &= -\frac{1}{r}\frac{\partial \Psi}{\partial z}, \\ B_z &= \frac{1}{r}\frac{\partial \Psi}{\partial r} + \mathrm{B}_0, \\ B_\theta &= 0. \end{aligned}\right. \tag{2.62}$$

Figure 2.12 (left) shows the stream function Ψ. It resembles the vorticity distribution in a vortex ring we can find in Danaila et al. (2021). It is not surprising since we have seen in (2.3) that the superconductor can be viewed as a superposition of circular vortex filaments.

The magnetic field on Fig. 2.12 (middle) is visually close to the one computed with the vector potential (2.10). More precisely, Fig. 2.12 (right) shows the norm $||\mathbf{B}_\psi - \mathbf{B}_A||$ of the difference between magnetic fields computed with the two methods. The agreement is very good.

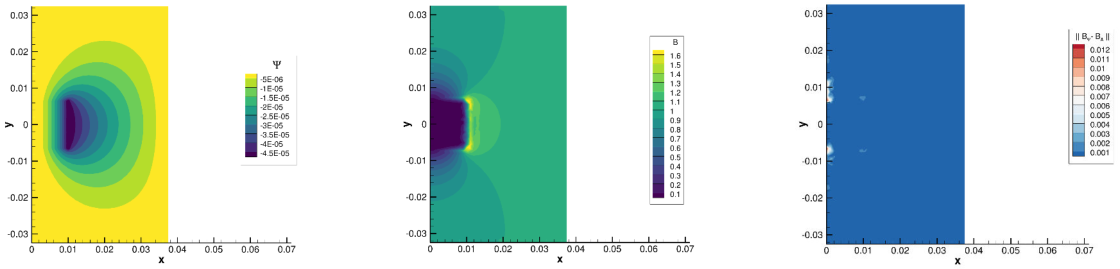

Figure 2.12. *London model in 2D. Stream function (left), magnetic field $||\boldsymbol{B}||$ (middle), error $||\boldsymbol{B}_\psi - \boldsymbol{B}_A||$ between the two methods (2.61) and (2.58) (right).*

London problem coupled with the finite solenoid

The goal of this section is to compute the magnetic field resulting from the interaction between a coil of finite length and a superconductor in the Meissner state. First we recall the formulae used to compute the vector potential and the magnetic field created by a finite solenoid. Then we solve the London equation when a non-uniform magnetic field is applied, in particular the one generated by a coil.

We consider a finite solenoid of length L along the z axis and radius a along the r axis (see Fig. 2.13).

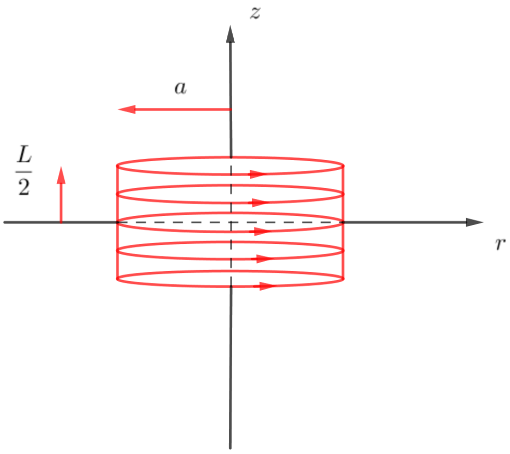

Figure 2.13. *Solenoid of finite length L and radius a.*

We suppose that the solenoid is constituted of N turns of wire and i is the current circulating in the wire. We denote $I = Ni$ the total current carried by the coil. Then the surface current density $\mathbf{K}$ can be written

$$\mathbf{K} = \frac{I}{L}\delta(r-a)\mathbf{e}_\theta, \tag{2.63}$$

where δ is the Dirac function.

By the Ampere's law of magnetostatic we know that $\nabla \times \mathbf{B} = \mu_0 \mathbf{K}$. Since $\mathbf{B} = \nabla \times \mathbf{A}$ we deduce

$$\nabla \times \nabla \times \mathbf{A} = \mu_0 \mathbf{K}. \tag{2.64}$$

By cylindrical symmetry $\mathbf{A} = A(r,z)\mathbf{e}_\theta$, hence div $\mathbf{A} = 0$. As a result $\nabla \times \nabla \times \mathbf{A} = -\Delta \mathbf{A}$ and we end up with the Laplace equation:

$$-\Delta \mathbf{A} = \mu_0 \mathbf{K}. \tag{2.65}$$

The solution of (2.65) is well known:

$$A(r,z) = \frac{\mu_0}{4\pi}\int_{\mathbb{R}^3} \frac{K(\mathbf{x}')}{|\mathbf{x}-\mathbf{x}'|}\mathrm{d}\mathbf{x}', \tag{2.66}$$

where $\mathbf{x} = (r,z,\theta)$ is the point of observation and $K = \frac{I}{L}\delta(r'-a)$.

Formula (2.66) can be made explicit using special functions (Jackson, 1999):

$$A(r,z) = -\frac{\mu_0}{4\pi}\frac{I}{L}\sqrt{\frac{a}{r}}\left[\zeta k\left(\frac{k^2+h^2-h^2k^2}{h^2k^2}K(k) - \frac{1}{k^2}E(k) + \frac{h^2-1}{h^2}\Pi(h,k)\right)\right]_{\zeta_-}^{\zeta_+}, \tag{2.67}$$

where

$$\begin{aligned}
&\zeta_\pm = z \mp \frac{L}{2},\\
&k^2 = \frac{4ar}{\zeta^2+(a+r)^2},\\
&h^2 = \frac{4ar}{(a+r)^2},\\
&K(k), E(k), \Pi(h,k), \text{ are the first, second and third elliptic integral, respectively.}
\end{aligned} \tag{2.68}$$

Thanks to the formula (2.59), we can calculate the magnetic field which is contained in the (z,r) plane:

$$\begin{aligned}
B_r &= -\frac{\mu_0}{2\pi}\frac{I}{L}\sqrt{\frac{a}{r}}\left[\frac{k^2-2}{k}K(k) + \frac{2}{k}E(k)\right]_{\zeta_-}^{\zeta_+},\\
B_z &= -\frac{\mu_0}{2\pi}\frac{I}{L}\frac{1}{2\sqrt{ar}}\left[\zeta k\left(K(k) + \frac{a-r}{a+r}\Pi(h,k)\right)\right]_{\zeta_-}^{\zeta_+}.
\end{aligned} \tag{2.69}$$

FreeFEM offers a practical way to compute the elliptic integrals. We recall that by definition

$$\begin{aligned}
E(k) &= \int_0^{\frac{\pi}{2}} \sqrt{1-k^2\sin^2\theta}\,\mathrm{d}\theta,\\
K(k) &= \int_0^{\frac{\pi}{2}} \frac{\mathrm{d}\theta}{\sqrt{1-k^2\sin^2\theta}},\\
\Pi(h,k) &= \int_0^{\frac{\pi}{2}} \frac{\mathrm{d}\theta}{\sqrt{1-k^2\sin^2\theta}(1-h^2\sin^2\theta)}.
\end{aligned} \tag{2.70}$$

The segment $\left[0,\frac{\pi}{2}\right]$ is partitioned using the $meshL$ type:

```
meshL Th = segment(100, [pi/2.*x, y]);
```

The trigonometric functions under the integral signs are discretized using a standard linear Lagrange FE P^1; then the integral is computed in one line. For example the macro for $E(k)$ is

```
macro secondKind(k) int1d(Th)(sqrt(1. - (k*sin(x))*(k*sin(x))))//
```

Figure 2.14 shows the vector potential and the magnetic field obtained with Eqs. (2.67) and (2.69). Only the domain $r \geq 0$ is represented; the solution for $r \leq 0$ is obtained by symmetry with respect to the z axis. The parameters are the following:

$$\begin{aligned}
&a = 1.5\times10^{-2},\\
&L = 1.3\times10^{-2},\\
&I = 1.
\end{aligned} \tag{2.71}$$

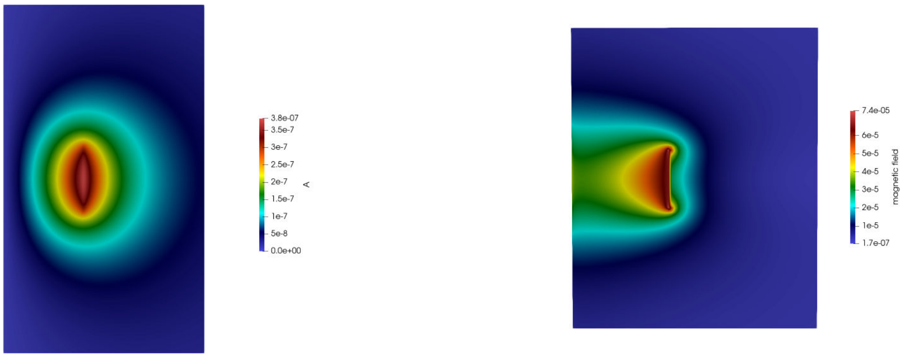

Figure 2.14. *Vector potential (left) and magnetic field (right) created by a solenoid.*

We now consider a cylindrical superconductor inserted in a coil. Figure 2.15 (left) shows the experimental set-up used to magnetize superconductors. To simplify the problem, we assume the coil is a strip encircling the superconductor (see Fig. 2.15 right).

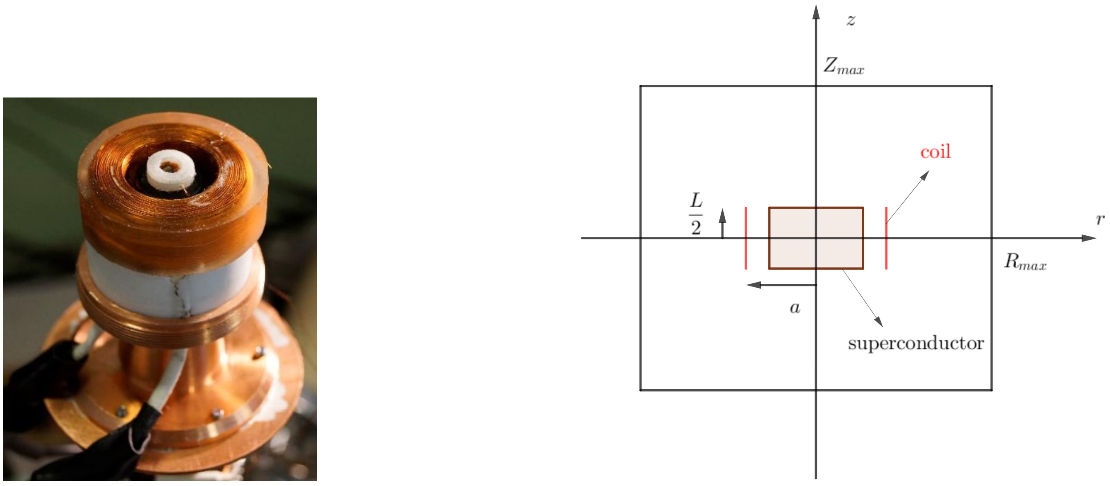

Figure 2.15. *Experimental set-up (left). Computational domain (right).*

We have seen in section (2.1) that, in the case of non homogenous applied field, the London equation is

$$-\Delta\mathbf{A} + \mathbb{1}\frac{1}{\lambda^2}\mathbf{A} = \mu_0\nabla\times\mathbf{H}. \tag{2.72}$$

We denote $\mu_0\mathbf{H} = \nabla\times\mathbf{A}_H$ where $\mathbf{A}_H$ is the vector potential associated to the coil; it is given by formula (2.67). Since div $\mathbf{A}_H = 0$, (2.72) becomes

$$-\Delta\mathbf{A} + \mathbb{1}\frac{1}{\lambda^2}\mathbf{A} = -\Delta\mathbf{A}_H. \tag{2.73}$$

In the same way as we obtained (2.58), we deduce the variational formulation of (2.73):

$$\int_\Omega \bar{\nabla} A \cdot \bar{\nabla} v - \int_\Omega \frac{1}{r}\frac{\partial A}{\partial r} v + \int_\Omega \frac{1}{r^2} A v + \int_\Omega \mathbb{1} \frac{1}{\lambda^2} A v = \int_\Omega \bar{\nabla} A_H \cdot \bar{\nabla} v \quad - \int_\Omega \frac{1}{r}\frac{\partial A_H}{\partial r} v + \int_\Omega \frac{1}{r^2} A_H v. \tag{2.74}$$

We use linear Lagrange finite elements P_1 in space. Figure 2.16 shows the results. The parameters for the coil are given by (2.71).

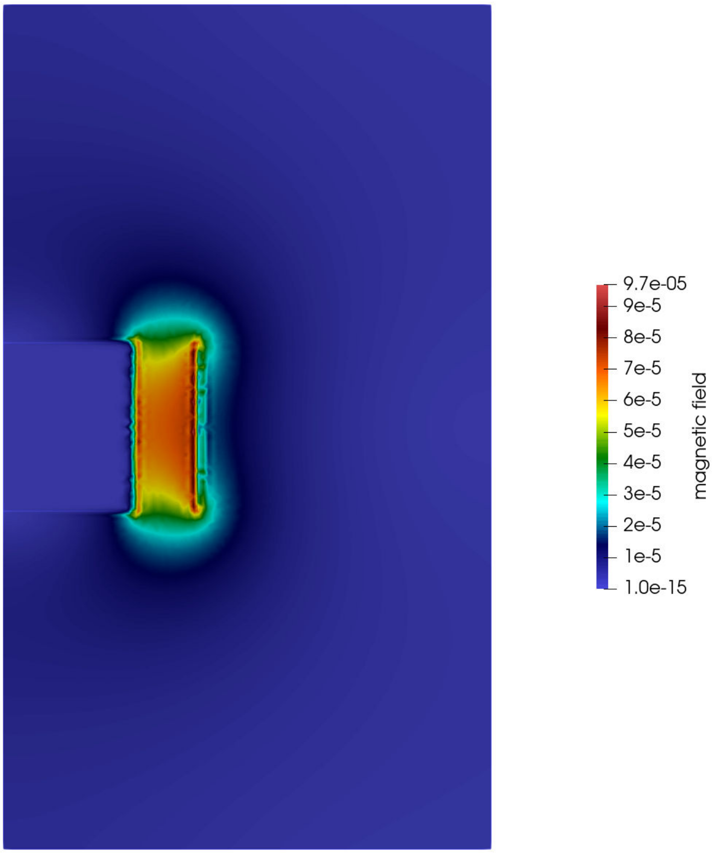

Figure 2.16. *Magnetic field resulting from the interaction of a superconductor in the Meissner state and a finite solenoid.*

2.4.2. 3D study

In this section we wish to solve directly the 3D problem (2.17) using Cartesian coordinates. Firstly, we wish to recover the solution computed in the 2D case where we used cylindrical coordinates. Second, we would like to get rid of the constraint of a bounded external domain which is an approximation of reality. We treat the unbounded case using a boundary element approach, a recent feature of FreeFEM. We recall the parameters (2.56):

$$\begin{cases} R_{max} = 37.5 \times 10^{-3}, Z_{max} = 32.5 \times 10^{-3}, \\ R_s = 1 \times 10^{-2}, Z_s = 6.5 \times 10^{-3}, \\ \lambda = 1.6 \times 10^{-7}, \\ \mathrm{B}_0 = 1, \\ M = 40. \end{cases} \tag{2.75}$$

where M refers to the number of nodes on the length R_{max}.

First case : the bounded external domain

We rewrite here the London model in Cartesian coordinates as seen in Section 2.2. We denote $\mathcal{O}$ an external cylindrical box and $\mathcal{S}$ a cylindrical superconductor (see Fig. 2.3):

$$\begin{cases} -\Delta A_x + \mathbb{1}\dfrac{A_x}{\lambda^2} = 0 & \text{in } \mathcal{O}, \\ -\Delta A_y + \mathbb{1}\dfrac{A_y}{\lambda^2} = 0 & \text{in } \mathcal{O}, \\ A_x = -\mathrm{B}_0\dfrac{y}{2} & \text{on } \partial\mathcal{O}, \\ A_y = \mathrm{B}_0\dfrac{x}{2} & \text{on } \partial\mathcal{O}, \\ A_z = 0 & \text{on } \partial\mathcal{O}. \end{cases} \tag{2.76}$$

To find the variational formulation of problem (2.76) we multiply each equation by a test function v_μ ($\mu = x, y, z$) and perform an integration by parts. We have to find A_μ component of $\mathbf{A}$ in $H^1(\mathcal{O})$ such that for every v_μ in $H^1_0(\mathcal{O})$

$$\sum_\mu (\nabla A_\mu, \nabla v_\mu) + \frac{1}{\lambda^2}\sum_\mu (\mathbb{1}A_\mu, v_\mu) = 0, \tag{2.77}$$

where we use the standard notation $(u, v) = \displaystyle\int_{\mathcal{O}} uv$ for the scalar product in L^2.

To discretize (2.77) we use linear Lagrange FE P^1. The transposition of (2.77) in FreeFEM syntax is simple:

```
varf vPb([A, Ay, Az], [v, vy, vz]) =
  int3d(Th)(grad(A)' * grad(v)
        + grad(Ay)' * grad(vy)
        + grad(Az)' * grad(vz)
        + Ind/lambda^2 * [A, Ay, Az]'*[v, vy, vz])
  + on(1, 2, 3, A = -B0*y/2., Ay = B0*x/2., Az = 0.);
```

Here *grad* is a macro defined by the user:

```
macro grad(u)[dx(u), dy(u), dz(u)]//
```

The magnetic field $\mathbf{B} = (B_x, B_y, B_z)$ is computed taking the curl of $\mathbf{A}$. Since we assume $A_z = 0$ it is given by:

$$\begin{cases} B_x = -\dfrac{\partial A_y}{\partial z}, \\ B_y = \dfrac{\partial A_x}{\partial z}, \\ B_z = \dfrac{\partial A_y}{\partial x} - \dfrac{\partial A_x}{\partial y}. \end{cases} \tag{2.78}$$

Figures 2.17-2.18 show the results. We recover the demagnetization effect with an increase of the field near the edge of the superconductor. However the effect is stronger than in the 2D results. An exclusion zone appears clearly above and below the superconducting cylinder. This ability to expel the magnetic flux called *shielding* is extensively used in medical or military applications.

In Fig. 2.18 (right) we compare the amplitude of the vector potential in the (y, z) plane with the one computed in 2D with Eq. (2.58). To be consistent we use linear Lagrange finite elements P^1 for both. The error is maximum along the edge of the superconductor. It is understandable since the vector potential varies rapidly near the edges (see Fig. 2.18 left).

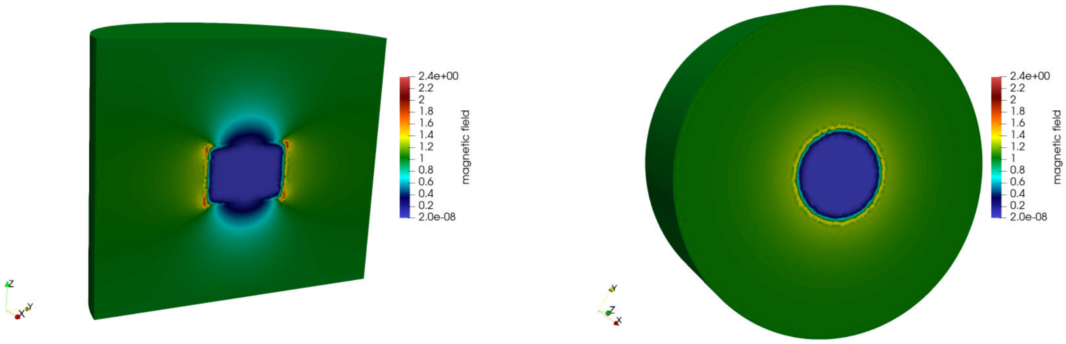

Figure 2.17. *London model in 3D, bounded case. Magnetic field in the (yz) plane (left). Magnetic field on the (xy) plane (right).*

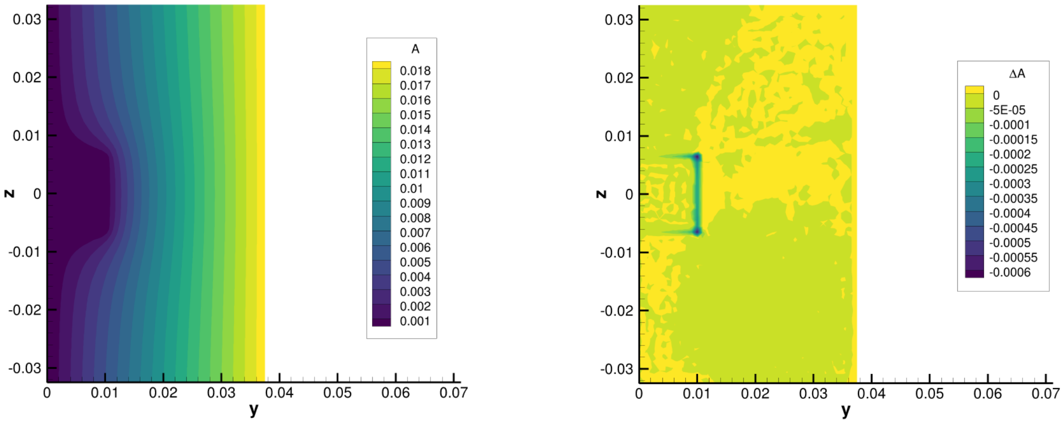

Figure 2.18. *London model in 3D, bounded case. Projection of the vector potential on the yz plane (left). Difference between the 3D and 2D solutions (right).*

In an unbounded domain

As we said in the introduction of the section, we want to treat the more realistic case of an unbounded external domain. For a uniform and static external magnetic field $\mathbf{B}_0$ the problem is

$$\begin{aligned} -\Delta \mathbf{A} + \mathbb{1}\frac{\mathbf{A}}{\lambda^2} &= \mathbf{0}, \\ \nabla \times \mathbf{A} \underset{|\mathbf{r}|\to\infty}{\to} & \mathbf{B}_0. \end{aligned} \tag{2.79}$$

The continuity of $\mathbf{A}$ and of the Neumann trace $\nabla\mathbf{A}\cdot\mathbf{n}$ is required across the boundary $\Gamma := \partial\Omega$; the reason for this will appear in the sequel. Therefore we add the jump conditions

$$\begin{aligned} [\mathbf{A}]_\Gamma &= 0, \\ [\nabla\mathbf{A}\cdot\mathbf{n}]_\Gamma &= 0. \end{aligned} \tag{2.80}$$

We make the change of variables

$$\mathbf{A} = \mathbf{A}' + \mathbf{A}_0, \tag{2.81}$$

where $\nabla \times \mathbf{A}_0 = \mathbf{B}_0$ since we want to have homogenous boundary conditions at infinity. In this case we have $\mathbf{A}_0 = \begin{pmatrix} -\frac{\mathrm{B}_0}{2}y \\ \frac{\mathrm{B}_0}{2}x \end{pmatrix}$.

Plugging (2.81) in (2.79)-(2.80) and dropping the primes, we obtain the London model in the unbounded case

$$\begin{cases} -\Delta \mathbf{A} + \mathbb{1}_\Omega \frac{\mathbf{A}}{\lambda^2} = -\mathbb{1}_\Omega \frac{\mathbf{A}_0}{\lambda^2}, \\ \nabla \times \mathbf{A} \underset{|\mathbf{r}|\to 0}{\to} \mathbf{0}, \\ [\mathbf{A}]_\Gamma = 0, \\ [\nabla\mathbf{A}\cdot\mathbf{n}]_\Gamma = 0. \end{cases} \tag{2.82}$$

From now on, we expose the method to solve (2.82): it is called *boundary element method* (BEM). We can find a very similar problem in Bielak and MacCamy (1983). They studied the propagation of a wave of a given frequency in an elastic material; in addition they introduce an obstacle. The interface condition between the surrounding material and the obstacle are identical to (2.80). By analogy the obstacle is the superconductor and the elastic material is the air outside.

We follow the presentation of Bielak and MacCamy (1983) and introduce the necessary mathematical tools. The main idea of the BEM is the following. In the exterior, the vector potential obeys the simple Laplace equation

$$-\Delta \mathbf{A} = \mathbf{0} \quad \text{in } \mathbb{R}^3 \backslash \Omega. \tag{2.83}$$

An interesting property of the Laplacian operator is that we can find the solution of (2.83) at any point in the exterior of the superconductor provided we know it on its surface. The goal is then to build a system equivalent to (2.82) but replacing the unbounded exterior by the surface Γ of the superconductor (see the system (2.91)). Finally we are left with discretizing "only" the interior and the surface of the superconductor. Finite elements defined on the surface are called *boundary elements*. The final linear system is written in (2.94).

Let χ be a vector function defined on Γ. We first define the single layer potential SL and the double layer potential DL

$$\begin{aligned} SL(\chi)(\mathbf{x}) &:= \int_\Gamma \mathcal{G}(\mathbf{x},\mathbf{y})\chi(\mathbf{y})\mathrm{d}\sigma(\mathbf{y}) \quad \forall \mathbf{x} \in \mathbb{R}^3 \backslash \Gamma, \\ DL(\chi)(\mathbf{x}) &:= \int_\Gamma \frac{\partial}{\partial \mathbf{n_y}} \mathcal{G}(\mathbf{x},\mathbf{y})\chi(\mathbf{y})\mathrm{d}\sigma(\mathbf{y}) \quad \forall \mathbf{x} \in \mathbb{R}^3 \backslash \Gamma, \end{aligned} \tag{2.84}$$

where $\mathcal{G}$ is the Green function of the Laplace equation in $\mathbb{R}^3$. It is given by:

$$\mathcal{G}(\mathbf{x},\mathbf{y}) = \frac{1}{4\pi|\mathbf{x}-\mathbf{y}|}. \tag{2.85}$$

We now define the *boundary integral operators* (BIO) $\mathcal{S},\mathcal{N},\mathcal{D}$. For every function χ defined on the boundary

$$\begin{aligned} \mathcal{S}(\chi)(\mathbf{x}) &:= \int_\Gamma \mathcal{S}(\mathbf{x},\mathbf{y})\chi(\mathbf{y})\mathrm{d}\sigma(\mathbf{y}), \quad \mathcal{S}(\mathbf{x},\mathbf{y}) = \mathcal{G}(\mathbf{x},\mathbf{y})\Bigg|_{\mathbf{x}\in\Gamma}, \\ \mathcal{N}(\chi)(\mathbf{x}) &:= \int_\Gamma \mathcal{N}(\mathbf{x},\mathbf{y})\chi(\mathbf{y})\mathrm{d}\sigma(\mathbf{y}), \quad \mathcal{N}(\mathbf{x},\mathbf{y}) = \frac{\partial \mathcal{G}}{\partial \mathbf{n_x}}(\mathbf{x},\mathbf{y})\Bigg|_{\mathbf{x}\in\Gamma}, \\ \mathcal{D}(\chi)(\mathbf{x}) &:= \int_\Gamma \mathcal{D}(\mathbf{x},\mathbf{y})\chi(\mathbf{y})\mathrm{d}\sigma(\mathbf{y}), \quad \mathcal{D}(\mathbf{x},\mathbf{y}) = \frac{\partial \mathcal{G}}{\partial \mathbf{n_y}}(\mathbf{x},\mathbf{y})\Bigg|_{\mathbf{x}\in\Gamma}. \end{aligned} \tag{2.86}$$

The main result is that we have explicit formulae for the Dirichlet and Neumann traces of the potentials (2.84); and these traces can be expressed with the BIO (2.86) as follows

$$\gamma_D{}^+ \circ SL(\chi) = \mathcal{S}(\chi), \quad \gamma_N{}^+ \circ SL(\chi) = \frac{1}{2}\chi + \mathcal{N}(\chi), \tag{2.87}$$

where γ_D^+ and γ_N^+ are Dirichlet (resp. Neumann) traces taken from the exterior, $\mathbf{N}$ being the normal to the boundary Γ oriented towards the exterior $\mathbb{R}^3\backslash\bar{\Omega}$.

Moreover we know that there exist a unique function χ defined on the boundary Γ such that

$$\mathbf{A} = SL(\chi) \quad \text{in} \quad \mathbb{R}^3\backslash\bar{\Omega}. \tag{2.88}$$

From (2.87) and (2.88) we deduce that

$$\gamma_D{}^+ \circ \mathbf{A} = \mathcal{S}(\chi) \quad \text{and} \quad \gamma_N{}^+ \circ \mathbf{A} = \frac{1}{2}\chi + \mathcal{N}(\chi). \tag{2.89}$$

From the jump conditions at the boundary (2.80) and using (2.89) we have

$$\gamma_D{}^- \circ \mathbf{A} = \mathcal{S}(\chi) \quad \text{and} \quad \gamma_N{}^- \circ \mathbf{A} = \frac{1}{2}\chi + \mathcal{N}(\chi). \tag{2.90}$$

Finally the problem is

$$\begin{aligned}
&-\Delta \mathbf{A} + \frac{1}{\lambda^2}\mathbf{A} = -\frac{1}{\lambda^2}\mathbf{A}_0 \text{ in } \Omega,\\
&{\gamma_D}^- \circ \mathbf{A} = \mathcal{S}(\boldsymbol{\chi}) \text{ on } \Gamma,\\
&{\gamma_N}^- \circ \mathbf{A} = \frac{1}{2}\boldsymbol{\chi} + \mathcal{N}(\boldsymbol{\chi}) \text{ on } \Gamma.
\end{aligned} \tag{2.91}$$

Multiplying $(2.91)_1$ by a test function $\tilde{\mathbf{A}}$ and $(2.91)_2$ by a test function $\tilde{\boldsymbol{\chi}}$ then integrating by parts we obtain the following variational formulation: find $\mathbf{A}$ and $\boldsymbol{\chi}$ such that for every $\tilde{\mathbf{A}}$, $\tilde{\boldsymbol{\chi}}$

$$\begin{aligned}
&(\nabla \mathbf{A}, \nabla \tilde{\mathbf{A}}) - ({\gamma_N}^- \circ \mathbf{A}, {\gamma_D}^- \circ \tilde{\mathbf{A}}) + \frac{1}{\lambda^2}(\mathbf{A}, \tilde{\mathbf{A}}) + \frac{1}{\lambda^2}(\mathbf{A}_0, \tilde{\mathbf{A}}) = 0,\\
&(\mathbf{A}, \tilde{\boldsymbol{\chi}}) = (\mathcal{S}(\boldsymbol{\chi}), \tilde{\boldsymbol{\chi}}).
\end{aligned} \tag{2.92}$$

We solve each component A_i, χ_i with $i \in \{1, 2\}$ separately since they are not coupled. We drop the index i since the system is formally identical for each component and rewrite (2.92)

$$\begin{aligned}
&(\nabla A, \nabla \tilde{A}) - ({\gamma_N}^- \circ A, {\gamma_D}^- \circ \tilde{A}) + \frac{1}{\lambda^2}(A, \tilde{A}) + \frac{1}{\lambda^2}(A_0, \tilde{A}) = 0,\\
&(A, \tilde{\chi}) = (\mathcal{S}(\chi), \tilde{\chi}).
\end{aligned} \tag{2.93}$$

We now discretize the system (2.93). We approximate the domain Ω by a $\Omega_h = \cup_{K \in \mathcal{T}_h} K$ where $\mathcal{T}_h$ is a set of tetrahedrons and h is the mesh size. The boundary $\Gamma_h := \Gamma_h$ is a union of triangles. We approximate the fields A and χ by their projections A_h and χ_h on the spaces of linear Lagrange FEs denoted by $\mathcal{V}$ and $\mathcal{W}$ respectively. The system (2.92) becomes finite dimensional and its projection on a basis $(v_i) \times (w_j)$ of $\mathcal{V} \times \mathcal{W}$ can be written

$$\begin{pmatrix} L & -N \\ M & -S \end{pmatrix} \begin{pmatrix} A_h \\ \chi_h \end{pmatrix} = \begin{pmatrix} F \\ 0 \end{pmatrix}, \tag{2.94}$$

$$\begin{aligned}
&S \in \mathbb{R}^{n_\mathcal{W} \times n_\mathcal{W}},\ S_{ij} = \int_{\Gamma \times \Gamma} \mathcal{G}(\mathbf{x}, \mathbf{y}) w_i(\mathbf{x}) w_j(\mathbf{y}) \mathrm{d}\sigma(\mathbf{x}) \sigma(\mathbf{y}),\\
&N \in \mathbb{R}^{n_\mathcal{V} \times n_\mathcal{W}},\ N_{ij} = \frac{1}{2}\int_\Gamma v_i w_j + \int_{\Gamma \times \Gamma} \frac{\partial}{\partial \mathbf{n_x}} \mathcal{G}(\mathbf{x}, \mathbf{y}) v_i(\mathbf{x}) w_j(\mathbf{y}) \mathrm{d}\sigma(\mathbf{x}) \mathrm{d}\sigma(\mathbf{y}),\\
&M \in \mathbb{R}^{n_\mathcal{W} \times n_\mathcal{V}},\ M_{ij} = \int_\Gamma w_i v_j.
\end{aligned} \tag{2.95}$$

Figures 2.19-2.20 show the results. In Fig. 2.19, the edges of the superconductor appear to be well delimited compared to (2.17); the reason is that we use piecewise constant FEs in the present case instead of P^1. In Fig. 2.20, we compare the amplitude of the vector potential in the (y, z) plane with the one computed in 2D with Eq. (2.58). Linear Lagrange finite elements P^1 is used for both. As expected, the error is maximum on the $z = 0$ plane for $y = R_{max}$. In 2D flux lines are indeed assumed straight at $y = R_{max}$ but they are not in the present model; moreover their curvature is maximum on the plane $z = 0$.

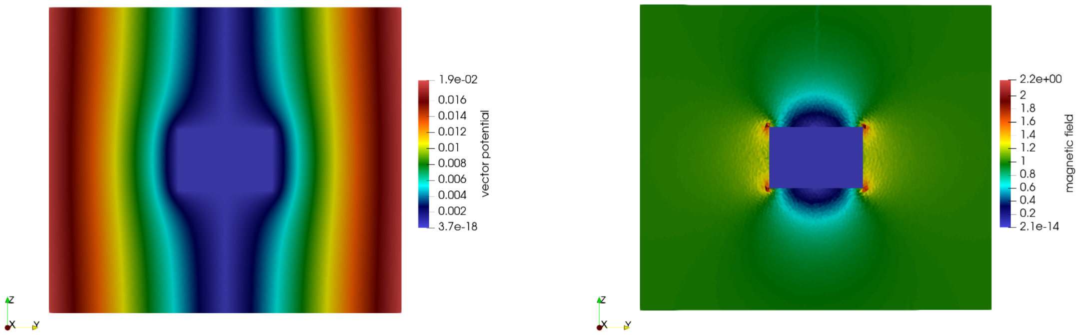

Figure 2.19. *London model in 3D, unbounded case. Vector potential in the yz plane (left). Magnetic field in the (yz) plane (right).*

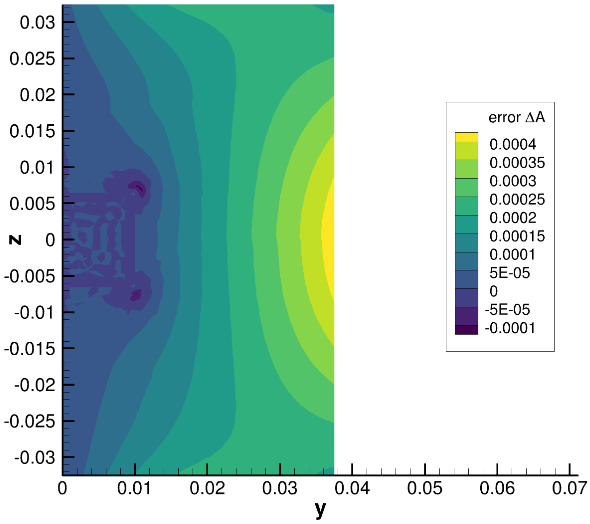

Figure 2.20. *London model in 3D, unbounded case. Difference between the BEM and 2D solutions.*

In this chapter we have studied the Meissner state of a superconductor. The superconductor expels the magnetic flux as long as the applied field is below the first critical field H_{c1}. Between H_{c1} and H_{c2} the superconductor is in a mixed state with flux lines or vortices entering the domain. This is the subject of the next chapter.

3. The time dependent Ginzburg-Landau model

In this chapter we introduce the TDGL model. We begin by a definition of the GL Gibbs free energy. Then we describe the TDGL model, the main scalings used in the literature, the concept of gauge and ω-gauge. Next, we outline the main results about existence and uniqueness of solutions. Subsequently, we present numerical examples in 2D and 3D. We end the chapter by a study of convergence orders for a mixed scheme using the ω-gauge.

3.1. Ginzburg-Landau free energy

Ginzburg and Landau, in their original paper (Ginzburg and Landau, 1950), decided to apply Landau's theory of second order phase transition to superconductors. Hence they postulated the existence of a complex valued function called the order parameter and denoted by ψ. This function describes completely the state of a superconductor. In particular the modulus $|\psi|^2$ corresponds to the density of Cooper pairs in the material.

They introduced the following energy density:

$$f = f_n + \alpha|\psi|^2 + \frac{\beta}{2}|\psi|^4 + \frac{B^2}{2\mu_0} + \frac{1}{2m_s}\left|\left(-i\hbar\nabla - e_s\mathbf{A}\right)\psi\right|^2 . \tag{3.1}$$

where f_n is the free energy of the normal phase; α and β are parameters which depend on the superconductor and the temperature. Near T_c we have at the first order:

$$\begin{aligned} &\alpha = \alpha_0\left(T - T_c\right), \quad \alpha_0 > 0, \\ &\beta = \beta_0. \end{aligned} \tag{3.2}$$

Notice that $\alpha < 0$ below T_c.

As in the London expression of the free energy (2.1) we have three terms:

$$\begin{aligned} &\mathcal{F}_s := \alpha|\psi|^2 + \frac{\beta}{2}|\psi|^4 : \text{the condensation energy density}, \\ &E_{kin} := \frac{1}{2m_s}\left|\left(-i\hbar\nabla - e_s\mathbf{A}\right)\psi\right|^2 : \text{the kinetic energy density}, \\ &E_{mag} := \frac{B^2}{2\mu_0} : \text{the magnetic energy density}. \end{aligned} \tag{3.3}$$

It happens that the free energy density (3.1) is adapted to the case where the magnetic induction $\mathbf{B}$ and temperature T are fixed. However the situation of interest is the case where the applied magnetic field $\mathbf{H}$ and the temperature T are fixed. Therefore we shall consider the Gibbs free energy (see de Gennes (1966) for details):

$$g = f - \mathbf{B} \cdot \mathbf{H}. \tag{3.4}$$

Then using (3.1) we find that

$$g = f_n + \alpha|\psi|^2 + \frac{\beta}{2}|\psi|^4 + \frac{B^2}{2\mu_0} + \frac{1}{2m_s}\left|(-i\hbar\nabla - e_s\mathbf{A})\,\psi\right|^2 - \mathbf{B}\cdot\mathbf{H}. \tag{3.5}$$

Since $\mathbf{B} = \nabla \times \mathbf{A}$ we deduce

$$g = f_n + \alpha|\psi|^2 + \frac{\beta}{2}|\psi|^4 + \frac{1}{2m_s}\left|(-i\hbar\nabla - e_s\mathbf{A})\,\psi\right|^2 + \frac{1}{2\mu_0}\left|\nabla\times\mathbf{A} - \mu_0\mathbf{H}\right|^2. \tag{3.6}$$

The total Gibbs free energy of the superconductors is then obtained by integrating (3.6) over the domain Ω of the superconductor

$$\mathcal{G} = \mathcal{G}_0 + \int_\Omega \alpha|\psi|^2 + \frac{\beta}{2}|\psi|^4 + \frac{1}{2m_s}\left|(-i\hbar\nabla - e_s\mathbf{A})\,\psi\right|^2 + \frac{1}{2\mu_0}\left|\nabla\times\mathbf{A} - \mu_0\mathbf{H}\right|^2, \tag{3.7}$$

where $\mathcal{G}_0 = \int_\Omega f_n$ is a constant.

3.2. Definition of the TDGL model and scaling

The equations of motion for the order parameter ψ and the vector potential $\mathbf{A}$ are the Euler-Lagrange equations associated to the Gibbs free energy density (3.7). We denote by Ω the superconducting domain and $\Gamma := \partial\Omega$ its boundary. In the SI units, the TDGL system reads:

$$\begin{aligned}
&\frac{\hbar^2}{2m_s D}\left(\frac{\partial}{\partial t} + i\frac{e_s}{\hbar}\phi\right)\psi = \frac{\hbar^2}{2m_s}\left(\nabla - i\frac{e_s}{\hbar}\mathbf{A}\right)^2\psi - \alpha\psi - \beta|\psi|^2\psi \quad \text{in } \Omega,\\
&\sigma\left(\frac{\partial\mathbf{A}}{\partial t} + \nabla\phi\right) = \frac{e_s\hbar}{2m_s i}(\psi^*\nabla\psi - \psi\nabla\psi^*) - \frac{e_s^2}{m_s}|\psi|^2\mathbf{A} - \frac{1}{\mu_0}\nabla\times(\nabla\times\mathbf{A} - \mu_0\mathbf{H}) \quad \text{in } \Omega.
\end{aligned} \tag{3.8}$$

The boundary conditions read:

$$\begin{aligned}
&(i\hbar\nabla\psi - e_s\mathbf{A}\psi)\cdot\mathbf{n} = 0 \text{ on } \Gamma,\\
&\nabla\times\mathbf{A}\times\mathbf{n} = \frac{1}{\mu_0}\mathbf{H}\times\mathbf{n} \quad \text{on } \Gamma,\\
&\mathbf{E}\cdot\mathbf{n} = 0 \quad \text{on } \Gamma.
\end{aligned} \tag{3.9}$$

The initial conditions read:

$$\begin{aligned}
\psi(\mathbf{x},0) &= \psi_0(\mathbf{x}) \quad \text{in } \Omega,\\
\mathbf{A}(\mathbf{x},0) &= \mathbf{A}_0(\mathbf{x}) \quad \text{in } \Omega.
\end{aligned} \tag{3.10}$$

D is a phenomenological diffusion coefficient, ϕ the electric potential and σ has the dimension of an electrical conductivity. We can rewrite Eq. (3.8)$_2$ for the vector potential as

$$\frac{1}{\mu_0}\nabla \times (\nabla \times \mathbf{A} - \mu_0 \mathbf{H}) = \mathbf{J}_s + \mathbf{J}_n, \tag{3.11}$$

where

$$\begin{aligned} \mathbf{J}_s &= \frac{e_s \hbar}{2m_s i}(\psi^* \nabla \psi - \psi \nabla \psi^*) - \frac{e_s^2}{m_s}|\psi|^2 \mathbf{A}, \\ \mathbf{J}_n &= -\sigma \left(\frac{\partial \mathbf{A}}{\partial t} + \nabla \phi \right). \end{aligned} \tag{3.12}$$

Hence we see that (3.11) is similar to the usual Maxwell-Ampere equation taking into accounts two kind of currents: $\mathbf{J}_s$ called *supercurrent* and $\mathbf{J}_n$ called *normal current*.

Boundary condition $(i\hbar\nabla\psi - e_s\mathbf{A}\psi)\cdot\mathbf{n} = 0$ implies that $\mathbf{J}_s \cdot \mathbf{n} = 0$; it means that the supercurrent does not escape from the superconductor. In the same manner $\mathbf{E}\cdot\mathbf{n} = 0$ implies that $\mathbf{J}_n \cdot \mathbf{n} = 0$. Finally $\nabla \times \mathbf{A} \times \mathbf{n} = \frac{1}{\mu_0}\mathbf{H} \times \mathbf{n}$ ensures the continuity of the tangential component of the magnetic field, which is the usual condition in electromagnetism provided there are no surface currents.

In order to non-dimensionalize (3.8) we start from the general scaling:

$$\begin{aligned} &\mathbf{x}' = \frac{\mathbf{x}}{x_0}, \quad \psi' = \frac{\psi}{\psi_0}, \quad \mathbf{A}' = \frac{\mathbf{A}}{A_0}, \\ &\phi' = \frac{\phi}{\phi_0}, \quad \mathbf{H}' = \frac{x_0 \mu_0}{A_0}\mathbf{H}, \quad \sigma' = \frac{\sigma}{\sigma_0}. \end{aligned} \tag{3.13}$$

Plugging (3.13) in (3.8) and dropping the primes for clarity we obtain:

$$\begin{aligned} &\frac{\hbar^2}{2m_s D t_0}\left(\frac{\partial}{\partial t} + i\frac{e_s t_0 \phi_0}{\hbar}\phi\right)\psi = \beta\psi_0^2\left[\frac{\hbar^2}{2m_s x_0^2 \beta \psi_0^2}\left(\nabla - i\frac{e_s x_0 A_0}{\hbar}\mathbf{A}\right)^2\psi - \frac{\alpha}{\beta\psi_0}\psi - |\psi|^2\psi\right], \\ &\frac{A_0}{\mu_0 x_0^2}\nabla \times \big(\nabla \times \mathbf{A}' - \mathbf{H}\big) = \frac{\hbar e_s \psi_0^2}{m_s x_0}\left[\frac{1}{2i}(\psi^*\nabla\psi - \psi\nabla\psi^*)\right. \\ &\qquad \left. - \frac{e_s x_0 A_0}{\hbar}|\psi|^2\mathbf{A} + \frac{A_0 x_0 e_s}{\hbar}\frac{m_s \sigma \sigma_0}{e_s^2 \psi_0^2 t_0}\left(-\nabla\phi\frac{\phi_0 t_0}{A_0 x_0} - \frac{\partial \mathbf{A}}{\partial t}\right)\right]. \end{aligned} \tag{3.14}$$

We set the following:

$$\psi_0^2 = \frac{-\alpha}{\beta}, \quad A_0 = \frac{\hbar}{e_s \xi}, \quad \frac{\phi_0 t_0}{A_0 x_0} = 1, \quad \sigma_0 = \frac{1}{\kappa^2 D \mu_0}. \tag{3.15}$$

where $\xi := \sqrt{\frac{\hbar^2}{2m_s(-\alpha)}}$ is the coherence length and $\kappa = \frac{\lambda}{\xi}$. Then (3.14) reads:

$$\begin{aligned} &\frac{\xi^2}{D t_0}\left(\frac{\partial}{\partial t} + i\frac{x_0}{\xi}\phi\right)\psi = \frac{\xi^2}{x_0^2}\left(\nabla - i\frac{x_0}{\xi}\mathbf{A}\right)^2\psi + \psi - |\psi|^2\psi, \\ &\frac{\lambda^2}{x_0 \xi}\nabla \times (\nabla \times \mathbf{A} - \mathbf{H}) = \frac{1}{2i}(\psi^*\nabla\psi - \psi\nabla\psi^*) - \frac{x_0}{\xi}|\psi|^2\mathbf{A} + \frac{x_0 \xi}{t_0 D}\sigma\left(-\nabla\phi - \frac{\partial \mathbf{A}}{\partial t}\right), \end{aligned} \tag{3.16}$$

where $\lambda := \sqrt{\dfrac{m_s\beta}{\mu_0 e_s^2(-\alpha)}}$ is the London length.

In the sequel we describe three possible choices for x_0 and t_0 that can be found in the literature. The first choice can be found for example in Chapman (2000), the second choice in Winiecki and Adams (2002) and the third choice in Gropp et al. (1996).

- *Choice 1*

  We set:

$$\begin{cases} x_0 = \lambda, \\ t_0 = \dfrac{\lambda^2}{D}. \end{cases} \tag{3.17}$$

  Then (3.16) reads:

$$\begin{aligned} &\frac{1}{\kappa^2}\left(\frac{\partial}{\partial t} + i\kappa\phi\right)\psi = \left(\frac{1}{\kappa}\nabla - i\mathbf{A}\right)^2 \psi + \psi' - |\psi|^2\psi, \\ &\nabla \times (\nabla \times \mathbf{A} - \mathbf{H}) = \frac{1}{2i\kappa}(\psi^*\nabla\psi - \psi\nabla\psi^*) - |\psi|^2\mathbf{A} + \frac{\sigma}{\kappa^2}\left(-\nabla\phi - \frac{\partial \mathbf{A}}{\partial t}\right). \end{aligned} \tag{3.18}$$

- *Choice 2*

  We set:

$$\begin{cases} x_0 = \xi, \\ t_0 = \dfrac{\xi^2}{D}. \end{cases} \tag{3.19}$$

  Then (3.16) reads:

$$\begin{aligned} &\left(\frac{\partial}{\partial t} + i\phi\right)\psi = (\nabla - i\mathbf{A})^2 \psi + \psi - |\psi|^2\psi, \\ &\kappa^2\nabla \times (\nabla \times \mathbf{A} - \mathbf{H}) = \frac{1}{2i}(\psi^*\nabla\psi - \psi\nabla\psi^*) - |\psi|^2\mathbf{A} + \sigma\left(-\nabla\phi - \frac{\partial \mathbf{A}}{\partial t}\right). \end{aligned} \tag{3.20}$$

- *Choice 3*

  We set:

$$\begin{cases} x_0 = \lambda, \\ t_0 = \dfrac{\xi^2}{D}. \end{cases} \tag{3.21}$$

  Then (3.16) reads:

$$\begin{aligned} &\left(\frac{\partial}{\partial t} + i\kappa\phi\right)\psi = \left(\frac{1}{\kappa}\nabla - i\mathbf{A}\right)^2 \psi + \psi - |\psi|^2\psi, \\ &\nabla \times (\nabla \times \mathbf{A} - \mathbf{H}) = \frac{1}{2i\kappa}(\psi^*\nabla\psi - \psi\nabla\psi^*) - |\psi|^2\mathbf{A} + \sigma\left(-\nabla\phi - \frac{\partial \mathbf{A}}{\partial t}\right). \end{aligned} \tag{3.22}$$

Scaling (3.21) is the most common in the literature and we will use it in the sequel. Using the scaling

(3.15) for $\mathbf{A}$ and ψ and the London length λ as unit length, the Gibbs free energy (3.7) becomes in units of $\frac{\alpha^2}{\beta}$:

$$\mathcal{G} = \mathcal{G}_0 + \int_\Omega \frac{1}{2}\left(|\psi|^2 - 1\right) + \left|\left(\frac{1}{\kappa}\nabla - i\mathbf{A}\right)\psi\right|^2 + |\nabla \times \mathbf{A} - \mathbf{H}|^2 . \tag{3.23}$$

3.3. Gauge definition and properties

Energy (3.23) is invariant under certain mathematical transformations called gauge transformations. Therefore the physical properties of the system do not depend on these transformations. In Du (1994b) we find the general definition of a gauge for the TDGL model:

Definition 3.3.1. *Given a function χ, a gauge transformation is a linear transformation G_χ given by*

$$\begin{aligned} &G_\chi(\psi, \boldsymbol{A}, \phi) = (\zeta, \boldsymbol{Q}, \Theta), \\ &\textit{where } \zeta = \psi e^{i\kappa\chi}, \boldsymbol{Q} = \boldsymbol{A} + \nabla\chi, \Theta = \phi - \frac{\partial\chi}{\partial t}. \end{aligned} \tag{3.24}$$

If $G_\chi(\psi, \mathbf{A}, \phi) = (\zeta, \mathbf{Q}, \Theta)$ then $(\zeta, \mathbf{Q}, \Theta)$ and $(\psi, \mathbf{A}, \phi)$ are said to be *gauge equivalent*. It is easily seen from (3.24) that $\nabla \times \mathbf{Q} = \nabla \times \mathbf{A}$ and $|\zeta|^2 = |\psi|^2$; hence the magnetic field or the density of the charge carriers, two physically relevant quantities, do not depend on the gauge. Moreover we see that:

$$\left(\frac{1}{\kappa}\nabla - i\mathbf{Q}\right)\zeta = \left(\frac{1}{\kappa}\nabla - i\mathbf{A}\right)\psi e^{i\kappa\chi}. \tag{3.25}$$

As a result the kinetic term $\left|\left(\frac{1}{\kappa}\nabla - i\mathbf{A}\right)\psi\right|^2$ in (3.23) is invariant under the transformation (3.24). We conclude that the energy (3.23) is gauge invariant.

In the literature three kind of gauges are usually employed. We now detail each of them.

Definition 3.3.2. *(Coulomb gauge)*

Given a solution $(\psi, \boldsymbol{A}, \phi)$ we can find a function χ such that

$$\begin{aligned} \Delta\chi &= -\operatorname{div}\boldsymbol{A} && \textit{in } \Omega, \\ \nabla\chi \cdot \boldsymbol{n} &= -\boldsymbol{A} \cdot \boldsymbol{n} && \textit{on } \Gamma. \end{aligned} \tag{3.26}$$

The transformed $\mathbf{A}$ verifies $\operatorname{div}\mathbf{A} = 0$ in Ω and $\mathbf{A} \cdot \mathbf{n} = 0$ on Γ. Moreover TDGL equations (3.22) with $\sigma = 1$ are given by the following proposition.

Proposition 3.3.3. *(TDGL model under Coulomb gauge)*

$$\begin{aligned}
&\left(\frac{\partial}{\partial t} + i\kappa\phi\right)\psi = \left(\frac{1}{\kappa}\nabla - i\boldsymbol{A}\right)^2 \psi + \psi - |\psi|^2\psi \quad \textit{in } \Omega,\\
&\frac{\partial \boldsymbol{A}}{\partial t} + \nabla \times \nabla \times \boldsymbol{A} + \nabla\phi = \frac{1}{2i\kappa}(\psi^*\nabla\psi - \psi\nabla\psi^*) - |\psi|^2\boldsymbol{A} + \nabla \times \boldsymbol{H} \quad \textit{in } \Omega,\\
&-\Delta\phi = \operatorname{div}\left(\frac{1}{2i\kappa}(\psi^*\nabla\psi - \psi\nabla\psi^*) - |\psi|^2\boldsymbol{A}\right) \quad \textit{in } \Omega,\\
&\operatorname{div}\boldsymbol{A} = 0 \quad \textit{in } \Omega,\\
&\nabla\psi\cdot\boldsymbol{n} = 0, \quad \nabla\phi\cdot\boldsymbol{n} = 0 \quad \textit{on } \Gamma,\\
&\nabla\boldsymbol{A}\times\boldsymbol{n} = \boldsymbol{H}\times\boldsymbol{n}, \quad \boldsymbol{A}\cdot\boldsymbol{n} = 0, \quad \textit{on } \Gamma.
\end{aligned} \tag{3.27}$$

Remark 3.3.4. *The Coulomb gauge seems attractive since we have the simplification $\nabla \times \nabla \times \boldsymbol{A} = -\Delta\boldsymbol{A}$. However the null divergence condition is in general difficult to impose numerically. Moreover the use of a Laplacian for $\boldsymbol{A}$ classically implies Dirichlet or Neumann type boundary conditions which is not the case in* (3.27)*.*

Definition 3.3.5. *(Lorentz gauge $\phi = -\operatorname{div}\boldsymbol{A}$)*

Given a solution $(\psi, \boldsymbol{A}, \phi)$ we can find a function χ such that

$$\begin{aligned}
&\frac{\partial\chi}{\partial t} - \Delta\chi = \phi + \operatorname{div}\boldsymbol{A} \quad \textit{in } \Omega,\\
&\nabla\chi\cdot\boldsymbol{n} = -\boldsymbol{A}\cdot\boldsymbol{n} \quad \textit{on } \Gamma,\\
&\textit{at t=0,} \quad \Delta\chi = -\operatorname{div}\boldsymbol{A} \quad \textit{in } \Omega, \quad \nabla\chi\cdot\boldsymbol{n} = -\boldsymbol{A}\cdot\boldsymbol{n} \quad \textit{on } \Gamma.
\end{aligned} \tag{3.28}$$

The transformed $\mathbf{A}$ verifies $\phi = -\operatorname{div}\mathbf{A}$ in Ω and $\mathbf{A}\cdot\mathbf{n} = 0$ on Γ. Moreover the TDGL equations (3.22) with $\sigma = 1$ are given by the following proposition.

Proposition 3.3.6. *(TDGL model under Lorentz gauge)*

$$\begin{aligned}
&\left(\frac{\partial}{\partial t} - i\kappa\operatorname{div}\boldsymbol{A}\right)\psi = \left(\frac{1}{\kappa}\nabla - i\boldsymbol{A}\right)^2 \psi + \psi - |\psi|^2\psi \quad \textit{in } \Omega,\\
&\frac{\partial \boldsymbol{A}}{\partial t} - \Delta\boldsymbol{A} + \nabla\phi = \frac{1}{2i\kappa}(\psi^*\nabla\psi - \psi\nabla\psi^*) - |\psi|^2\boldsymbol{A} + \nabla \times \boldsymbol{H} \quad \textit{in } \Omega,\\
&\nabla\boldsymbol{A}\times\boldsymbol{n} = \boldsymbol{H}\times\boldsymbol{n}, \quad \boldsymbol{A}\cdot\boldsymbol{n} = 0, \quad \nabla\psi\cdot\boldsymbol{n} = 0 \quad \textit{on } \Gamma.
\end{aligned} \tag{3.29}$$

Definition 3.3.7. *(Temporal gauge $\phi = 0$)*

Given a solution $(\psi, \boldsymbol{A}, \phi)$ we can find a function χ such that

$$\begin{aligned}
&\frac{\partial\chi}{\partial t} = \phi \quad \textit{in } \Omega,\\
&\nabla\chi\cdot\boldsymbol{n} = -\boldsymbol{A}\cdot\boldsymbol{n} \quad \textit{on } \Gamma,\\
&\textit{at t=0,} \quad \Delta\chi = -\operatorname{div}\boldsymbol{A} \quad \textit{in } \Omega \quad \nabla\chi\cdot\boldsymbol{n} = -\boldsymbol{A}\cdot\boldsymbol{n} \quad \textit{on } \Gamma.
\end{aligned} \tag{3.30}$$

The transformed $\mathbf{A}$ verifies $\phi = 0$ in Ω and $\mathbf{A}\cdot\mathbf{n} = 0$ on Γ. Moreover TDGL equations (3.22) with $\sigma = 1$ are given by the following proposition.

Proposition 3.3.8. *(TDGL model under temporal gauge)*

$$\begin{aligned}
&\frac{\partial \psi}{\partial t} = \left(\frac{1}{\kappa}\nabla - i\boldsymbol{A}\right)^2 \psi + \psi - |\psi|^2\psi \quad \text{in } \Omega,\\
&\frac{\partial \boldsymbol{A}}{\partial t} + \nabla\times\nabla\times\boldsymbol{A} = \frac{1}{2i\kappa}(\psi^*\nabla\psi - \psi\nabla\psi^*) - |\psi|^2\boldsymbol{A} + \nabla\times\boldsymbol{H} \quad \text{in } \Omega,\\
&\nabla\boldsymbol{A}\times\boldsymbol{n} = \boldsymbol{H}\times\boldsymbol{n}, \quad \boldsymbol{A}\cdot\boldsymbol{n} = 0, \quad \nabla\psi\cdot\boldsymbol{n} = 0 \quad \text{on } \Gamma.
\end{aligned} \tag{3.31}$$

The system (3.31) actually coincides with the classical descent method used in physics to find the state of lowest energy. Using the Gibbs energy (3.23), the descent method is

$$\begin{aligned}
\frac{\partial \psi}{\partial t} &= -\frac{\partial \mathcal{G}}{\partial \psi^*}(\psi, \mathbf{A}),\\
\frac{\partial \mathbf{A}}{\partial t} &= -\frac{\partial \mathcal{G}}{\partial \mathbf{A}}(\psi, \mathbf{A}).
\end{aligned} \tag{3.32}$$

Replacing the expressions of the derivatives in (3.32), we obtain a system identical to (3.31). Hence, TDGL model is equivalent to a descent method. We will come back to this remark in Chapter 4.

Remark 3.3.9. *It is interesting to note that in the temporal gauge* $\mathbf{A}$ *may not be divergence free. Indeed we have the following lemma*

Lemma 3.3.10.

$$\frac{\partial}{\partial t}\operatorname{div}\boldsymbol{A} = -\frac{i}{2}\kappa\left(\psi\frac{\partial\psi^*}{\partial t} - \psi^*\frac{\partial\psi}{\partial t}\right). \tag{3.33}$$

In hydrodynamic coordinates $\psi = \sqrt{\rho}e^{i\theta}$ *then the lemma reads* $\dfrac{\partial \operatorname{div}\boldsymbol{A}}{\partial t} = -\kappa\rho\dfrac{\partial\theta}{\partial t}$.

It has been noticed by Fleckinger-Pellé et al. (1997) that we can define a more general gauge by

$$\phi = -\omega \operatorname{div}\mathbf{A}, \tag{3.34}$$

where $\omega \geq 0$. It is called the ω-gauge. If $\omega = 0$ then $\phi = 0$ and we observe that we recover the temporal gauge; if $\omega = 1$ then $\phi = -\operatorname{div}\mathbf{A}$ and we recover the Lorentz gauge; finally if $\omega \to \infty$ then we must have $\operatorname{div}\mathbf{A} = 0$ and we find the Coulomb gauge. The ω-gauge is therefore an interesting tool that allows us to consider several gauges within a unified framework. In Section 3.7, we use extensively this property. The TDGL under the ω-gauge is:

$$\begin{aligned}
&\left(\frac{\partial}{\partial t} - i\omega\kappa\operatorname{div}\mathbf{A}\right)\psi = \left(\frac{1}{\kappa}\nabla - i\mathbf{A}\right)^2\psi + \psi - |\psi|^2\psi \quad \text{in } \Omega,\\
&\frac{\partial\mathbf{A}}{\partial t} + \nabla\times\nabla\times\mathbf{A} - \omega\nabla\operatorname{div}\mathbf{A} = \frac{1}{2i\kappa}(\psi^*\nabla\psi - \psi\nabla\psi^*) - |\psi|^2\mathbf{A} + \nabla\times\mathbf{H} \quad \text{in } \Omega,\\
&\nabla\times\mathbf{A}\times\mathbf{n} = \mathbf{H}\times\mathbf{n}, \quad \mathbf{A}\cdot\mathbf{n} = 0, \quad \nabla\psi\cdot\mathbf{n} = 0 \quad \text{on } \Gamma.
\end{aligned} \tag{3.35}$$

3.4. Mathematical results about TDGL solutions

In this part we describe some important mathematical properties of the TDGL model: the boundedness of $|\psi|$, the decrease of the energy with time and eventually existence and uniqueness results for the TDGL model under the temporal gauge.

Let us introduce some notations. In the following $H^s(\Omega)$ denotes the Sobolev space of order s, $\mathcal{H}^s(\Omega)$ the complex Sobolev space of order s, and $\mathbf{H}^s(\Omega) := (H^s(\Omega))^d$ where $d = 2$ or $d = 3$. Each of these spaces are Hilbert spaces equipped with a norm denoted by $||\cdot||_s$. For more details about Sobolev spaces one may consult Adams and Fournier (2003) or Cioranescu et al. (2018). Similarly we use $L^p(\Omega)$, $\mathcal{L}^p(\Omega)$ and $\mathbf{L}^p(\Omega)$ for the Lebesgue spaces of p-integrable functions. In addition, we introduce:

$$\begin{aligned}
&\mathbf{H}^1_n(\Omega) := \{\mathbf{A} \in \mathbf{H}^1(\Omega), \mathbf{A}\cdot\mathbf{n} = 0 \text{ on } \partial\Omega\},\\
&\mathbf{H}^1_n(\mathrm{div},\Omega) := \{\mathbf{A} \in \mathbf{H}^1_n(\Omega), \operatorname{div}\mathbf{A} = 0\},\\
&\mathbf{H}(\mathrm{div}) := \{\mathbf{A} \in \mathbf{L}^2(\Omega), \operatorname{div}\mathbf{A} \in \mathbf{L}^2(\Omega)\},\\
&\mathbf{H}_0(\mathrm{div}) := \{\mathbf{A} \in \mathbf{L}^2(\Omega), \operatorname{div}\mathbf{A} \in \mathbf{L}^2(\Omega) \text{ and } \mathbf{A}\cdot\mathbf{n} = 0\},\\
&\mathbf{H}(\mathrm{curl}) := \{\boldsymbol{\gamma} \in \mathbf{L}^2(\Omega), \nabla\times\boldsymbol{\gamma} \in \mathbf{L}^2(\Omega)\},\\
&\mathbf{H}_0(\mathrm{curl}) := \{\boldsymbol{\gamma} \in \mathbf{L}^2(\Omega), \nabla\times\boldsymbol{\gamma} \in \mathbf{L}^2(\Omega) \text{ and } \boldsymbol{\gamma}\times\mathbf{n} = 0\}.
\end{aligned} \tag{3.36}$$

The following proposition sets out a bound for $|\psi|$.

Proposition 3.4.1. *Hoffmann and Tang (2001) Let $(\psi, \boldsymbol{A}, \phi)$ a solution of the TDGL model. Assume that, at initial time, $|\psi_0(\boldsymbol{x})| \leq 1$, then*

$$|\psi(\boldsymbol{x}, t)| \leq 1 \quad \text{for almost all } \boldsymbol{x} \in \Omega, t > 0. \tag{3.37}$$

The next result gives an explicit formula for the time derivative of the Gibbs energy (3.23).

Proposition 3.4.2. *Hoffmann and Tang (2001) Let $u = (\psi, \phi, \boldsymbol{A})$ be a triplet of solutions of (3.22), H be independent of time. We have*

$$\frac{d}{dt}\mathcal{G}(u) = -||\frac{\partial\psi}{\partial t} + i\phi\psi||^2_{L^2(\Omega)} - ||\frac{\partial\mathbf{A}}{\partial t} + \nabla\phi||^2_{L^2(\Omega)}. \tag{3.38}$$

An immediate consequence of proposition (3.38) is that the energy is a decreasing function of time.

Remark 3.4.3. *Both propositions (3.37) and (3.38) are of great importance when doing numerics. In practice, an increase of the energy or the breaking of condition (3.37) are visible signs of a convergence or stability issue.*

Several authors have tackled the problem of existence and uniqueness of a solution. Finite element methods have been studied in Du (1994b), Chen et al. (1993), Tang and Wang (1995). We can find another point of view in Fleckinger-Pellé et al. (1997): here the authors show the existence of a dynamical process for the TDGL equations.

We outline here the method of Du (1994b) for the TDGL model under the temporal gauge (3.30).

In the sequel Ω is an open bounded set in $\mathbb{R}^d$ ($d = 2$ or 3) with smooth boundary. We also use the following time dependent Sobolev space:

$$\begin{aligned}
&\mathbf{V} := \mathbf{L}^\infty(0,T;\mathbf{H}^1_n(\Omega)) \cap \mathbf{H}^1(0,T;\mathbf{L}^2(\Omega)),\\
&\mathcal{V} := \mathcal{L}^\infty(0,T;\mathcal{H}^1(\Omega)) \cap \mathcal{H}^1(0,T;\mathcal{L}^2(\Omega)).
\end{aligned} \tag{3.39}$$

We begin by writing the weak formulation of (3.31):

$$\left\{\begin{array}{l}
\text{find } (\psi, \mathbf{A}) \in \mathcal{V} \times \mathbf{V} \text{ such that} \\
\dfrac{\mathrm{d}}{\mathrm{d}t}(\psi, \tilde{\psi}) + \left(\left[\dfrac{1}{\kappa}\nabla\psi - i\mathbf{A}\psi\right], \left[\dfrac{1}{\kappa}\nabla\tilde{\psi} - i\mathbf{A}\tilde{\psi}\right] \right) + ([|\psi|^2 - 1]\psi, \tilde{\psi}) = 0 \quad \text{for all } \tilde{\psi} \in \mathcal{H}^1(\Omega), \\
\dfrac{\mathrm{d}}{\mathrm{d}t}(\mathbf{A}, \tilde{\mathbf{A}}) + (\nabla \times \mathbf{A}, \nabla \times \tilde{\mathbf{A}}) + (|\psi|^2\mathbf{A}, \tilde{\mathbf{A}}) - \dfrac{1}{2i\kappa}(\psi^*\nabla\psi - \psi\nabla\psi^*, \tilde{\mathbf{A}}) \\
\quad = (\mathbf{H}, \nabla \times \tilde{\mathbf{A}}) \quad \text{for all } \tilde{\mathbf{A}} \in \mathbf{H}_n^1(\Omega), \\
\text{with at t = 0, } \psi_0 \in \mathcal{H}^1(\Omega) \text{ , } \mathbf{A}_0 \in \mathbf{H}_n^1(\mathrm{div}, \Omega),
\end{array}\right. \tag{3.40}$$

where the scalar product for ψ is the sesquilinear form in $\mathcal{L}^2(\Omega)$ defined by $(u, v) = \displaystyle\int_\Omega uv^*$. Then we introduce a modified form of (3.40). Let $\epsilon > 0$,

$$\left\{\begin{array}{l}
\text{find } (\psi^\epsilon, \mathbf{A}^\epsilon) \in \mathcal{V} \times \mathbf{V} \text{ such that} \\
\dfrac{\mathrm{d}}{\mathrm{d}t}(\psi^\epsilon, \tilde{\psi}) + \left(\left[\dfrac{1}{\kappa}\nabla\psi^\epsilon - i\mathbf{A}^\epsilon\psi^\epsilon\right], \left[\dfrac{1}{\kappa}\nabla\tilde{\psi} - i\mathbf{A}^\epsilon\tilde{\psi}\right] \right) + ([|\psi^\epsilon|^2 - 1]\psi^\epsilon, \tilde{\psi}) = 0 \quad \text{for all } \tilde{\psi} \in \mathcal{H}^1(\Omega), \\
\dfrac{\mathrm{d}}{\mathrm{d}t}(\mathbf{A}^\epsilon, \tilde{\mathbf{A}}) + (\nabla \times \mathbf{A}^\epsilon, \nabla \times \tilde{\mathbf{A}}) + \epsilon(\mathrm{div}\, \mathbf{A}^\epsilon, \mathrm{div}\, \tilde{A}) + (|\psi^\epsilon|^2\mathbf{A}^\epsilon, \tilde{\mathbf{A}}) \\
\quad -\dfrac{1}{2i\kappa}(\psi^*\nabla\psi - \psi\nabla\psi^*, \tilde{\mathbf{A}}) = (\mathbf{H}, \nabla \times \tilde{\mathbf{A}}) \quad \text{for all } \tilde{\mathbf{A}} \in \mathbf{H}_n^1(\Omega).
\end{array}\right. \tag{3.41}$$

Existence and uniqueness of solutions for (3.41) follow from classical methods used in Navier-Stokes equations (Temam, 2001).

Finite dimensional subspaces $\mathbf{\Lambda}_n$ (resp. $\mathcal{Z}_n$) of $\mathbf{H}_n^1$ (resp $\mathcal{H}^1$) are introduced. The Galerkin approximation of (3.41) is:

$$\left\{\begin{array}{l}
\text{find } (\psi_n^\epsilon(t), \mathbf{A}_n^\epsilon(t)) \in \mathcal{Z}_n \times \mathbf{\Lambda}_n \text{ such that} \\
(\nabla\psi_n^\epsilon(0), \nabla\tilde{\psi}_n) + (\psi_n^\epsilon(0), \tilde{\psi}_n) = (\nabla\psi(0), \nabla\tilde{\psi}_n) + (\psi(0), \tilde{\psi}_n) \quad \text{for all } \tilde{\psi}_n \in \mathcal{Z}_n, \\
(\nabla\mathbf{A}_n^\epsilon(0), \nabla\tilde{\mathbf{A}}_n) + (\mathbf{A}_n^\epsilon(0), \tilde{\mathbf{A}}_n) = (\nabla\mathbf{A}(0), \nabla\tilde{\mathbf{A}}) + (\mathbf{A}(0), \tilde{\mathbf{A}}_n) \quad \text{for all } \tilde{\mathbf{A}}_n \in \mathbf{\Lambda}_n, \\
\dfrac{\mathrm{d}}{\mathrm{d}t}(\psi_n^\epsilon, \tilde{\psi}_n) + \left(\left[\dfrac{1}{\kappa}\nabla\psi_n^\epsilon - i\mathbf{A}_n^\epsilon\psi_n^\epsilon\right], \left[\dfrac{1}{\kappa}\nabla\tilde{\psi}_n - i\mathbf{A}_n^\epsilon\tilde{\psi}_n\right] \right) + ([|\psi_n^\epsilon|^2 - 1]\psi_n^\epsilon, \tilde{\psi}_n) = 0 \quad \text{for all } \tilde{\psi}_n \in \mathcal{Z}_n, \\
\dfrac{\mathrm{d}}{\mathrm{d}t}(\mathbf{A}_n^\epsilon, \tilde{\mathbf{A}}_n) + (\nabla \times \mathbf{A}_n^\epsilon, \nabla \times \tilde{\mathbf{A}}_n) + \epsilon(\mathrm{div}\, \mathbf{A}_n^\epsilon, \mathrm{div}\, \tilde{\mathbf{A}}_n) + (|\psi_n^\epsilon|^2\mathbf{A}_n^\epsilon, \tilde{\mathbf{A}}_n) \\
\quad -\dfrac{1}{2i\kappa}(\psi_n^*\nabla\psi_n - \psi_n\nabla\psi_n^*, \tilde{\mathbf{A}}_n) = (\mathbf{H}, \nabla \times \tilde{\mathbf{A}}_n) \quad \text{for all } \tilde{\mathbf{A}}_n \in \mathbf{\Lambda}_n.
\end{array}\right. \tag{3.42}$$

The main result is the following:

Theorem 3.4.4. *Du (1994b) Given $\epsilon > 0$ and a final time $T > 0$, there exist $(\psi^\epsilon, \mathbf{A}^\epsilon)$ in $\mathcal{V} \times \mathbf{V}$ solution of (3.41), weak limit of a sequence $(\psi_{n_k}^\epsilon, \mathbf{A}_{n_k}^\epsilon)$ of solutions of (3.42) as $n_k \longrightarrow +\infty$. Moreover such a solution is unique.*

To obtain the solution for (3.40) we need to pass to the limit as $\epsilon \longrightarrow 0$. The main result is:

Theorem 3.4.5. *Du (1994b) Given a final time $T > 0$, there exists a solution of (3.40) $(\psi, \boldsymbol{A})$ in $\mathcal{V} \times \boldsymbol{V}$ which is the weak limit of a subsequence $(\psi^{\epsilon_k}, \boldsymbol{A}^{\epsilon_k})$ of solutions of (3.41) as $\epsilon_k \longrightarrow 0$. Moreover for any given initial conditions, the solution of (3.40) is unique.*

Remark 3.4.6. *The well-posedness of TDGL presented here is still valid if Ω is a convex polygon ($d = 2$) or polyhedra ($d = 3$). Well-posedness in non-convex domains has been studied by Li and Zhang (2017).*

3.5. Numerical results in 2D

In this section, we first describe the numerical schemes that we used for the discretization of the TDGL model (3.35). Then various examples from the literature are treated. In particular we describe in detail each equilibrium pattern. Finally, we address the problem of varying the gauge through the use of the ω-gauge.

3.5.1. Numerical schemes

We describe below two schemes based on two variational formulations of the TDGL model. We will make use of the ω-gauge so that our study covers both $\omega = 0$ (temporal gauge) and $\omega = 1$ (Lorentz gauge).

First scheme

From (3.40) and (3.35), we deduce the following variational formulation in the ω-gauge setting:

$$\left\{\begin{array}{l} \text{find } (\psi, \mathbf{A}) \in \mathcal{H}^1(\Omega) \times \mathbf{H}^1_n(\Omega) \text{ such that} \\ \dfrac{\mathrm{d}}{\mathrm{d}t}(\psi, \tilde{\psi}) - i\kappa\omega(\psi \operatorname{div} \mathbf{A}, \tilde{\psi}) + \left(\left[\dfrac{1}{\kappa}\nabla\psi - i\mathbf{A}\psi\right], \left[\dfrac{1}{\kappa}\nabla\tilde{\psi} - i\mathbf{A}\tilde{\psi}\right]\right) \\ \quad +([|\psi|^2 - 1]\psi, \tilde{\psi}) = 0 \quad \text{ for all } \tilde{\psi} \in \mathcal{H}^1(\Omega), \\ \dfrac{\mathrm{d}}{\mathrm{d}t}(\mathbf{A}, \tilde{\mathbf{A}}) + (\nabla \times \mathbf{A}, \nabla \times \tilde{\mathbf{A}}) - \omega(\operatorname{div}(\mathbf{A}), \operatorname{div}(\tilde{\mathbf{A}})) + (|\psi|^2\mathbf{A}, \tilde{\mathbf{A}}) \\ \quad -\dfrac{1}{2i\kappa}(\psi^*\nabla\psi - \psi\nabla\psi^*, \tilde{\mathbf{A}}) = (\mathbf{H}, \nabla \times \tilde{\mathbf{A}}) \quad \text{ for all } \tilde{\mathbf{A}} \in \mathbf{H}^1_n(\Omega), \end{array}\right. \tag{3.43}$$

with initial condition $\psi_0 \in \mathcal{H}^1(\Omega)$, $\mathbf{A}_0 \in \mathbf{H}^1_n(\operatorname{div}, \Omega)$.

For time discretization we use a Crank-Nicolson approximation for the two linear parts $\nabla_A := \dfrac{i}{\kappa}\nabla + \mathbf{A}$ and $L_A(\mathbf{A}, \mathbf{v}) := (\nabla \times \mathbf{A}, \nabla \times \mathbf{v}) + \omega(\operatorname{div} \mathbf{A}, \operatorname{div} \mathbf{v}) + |\psi^n|^2(\mathbf{A}, \mathbf{v})$.

We approximate the nonlinear part $\mathcal{N}(\psi) := (1 - |\psi|^2)\psi$ in the equation for ψ by an Adams-Bashforth scheme. Fields $\mathbf{A}$ and ψ are approximated by Lagrange FEs.

The transcription of formulation (3.43) in terms of time differences $q_{\mathbf{A}} := \mathbf{A}^{n+1} - \mathbf{A}^n$ and $q_\psi = \psi^{n+1} - \psi^n$ with FreeFEM syntax is:

```
varf vqA([qA,qAy], [B, By]) = int2d(Th)(1/dt*[qA,qAy]'*[B,By]
  - 0.5*opLinA(qA,B,psiold))
  + on(1, qAy = 0)
  + on(2, qA = 0) ; // matrix for A

varf vrhsA(def(qA),def(B)) = int2d(Th)(opJs(psiold,psioldConj,B))
  + int2d(Th)(opLinA(Aold,B,psiold))
  + int2d(Th)(h0*Curl(B))
  + on(1, qAy = 0)
  + on(2, qA = 0); // right-hand side for A

varf vqPsi(qPsi, v) =  int2d(Th)(1/dt*qPsi*v - 0.5*opGradA(qPsi, v, Aold));
// matrix for psi

varf vrhsPsi(qPsi,v) = int2d(Th)(1.5*opN(psiold)*v - 0.5*opN(psiold2)*v)
  + int2d(Th, mpirank)(I*kappa*omega*div(Aold)*psiold*v)
  + int2d(Th)(opGradA(psiold, v, Aold)); // right-hand side for psi
```

where $opLinA$, $opGradA$, opN, $opJs$ are macros defined by the user corresponding to L_A, ∇_A, $\mathcal{N}$ and supercurrent $\mathbf{J}_s = \dfrac{1}{2i\kappa}(\psi^*\nabla\psi - \psi\nabla\psi^*)$ respectively.

Second scheme

This scheme has been originally proposed by Gao and Sun (2015). It is a mixed scheme in the sense that $\gamma = \nabla \times \mathbf{A}$ is introduced as a supplementary unknown. In 2D, γ is taken as a scalar with $\gamma = \dfrac{\partial A_2}{\partial x} - \dfrac{\partial A_1}{\partial y}$, where $\mathbf{A} = (A_1(x,y), A_2(x,y))$. The mixed form of the TDGL model in the ω-gauge is:

$$\begin{array}{l}
\dfrac{\partial\psi}{\partial t} - i\kappa\omega \operatorname{div}\mathbf{A} = \left(\dfrac{1}{\kappa}\nabla - i\mathbf{A}\right)^2 \psi + \psi - |\psi|^2\psi \quad \text{in } \Omega,\\
\gamma = \nabla \times \mathbf{A} \quad \text{in } \Omega,\\
\dfrac{\partial\mathbf{A}}{\partial t} - \omega\nabla \operatorname{div}\mathbf{A} + \nabla\times\gamma = \dfrac{1}{2i\kappa}\left(\psi^*\nabla\psi - \psi\nabla\psi^*\right) - |\psi|^2\mathbf{A} + \nabla\times\mathbf{H} \quad \text{in } \Omega,
\end{array} \tag{3.44}$$

with boundary and initial conditions:

$$\begin{array}{l}
\dfrac{\partial\psi}{\partial\mathbf{n}} = 0, \quad \gamma = H, \quad \mathbf{A}\cdot\mathbf{n} = 0 \quad \text{on } \Gamma,\\
\psi(\mathbf{x},0) = 1, \quad \gamma(\mathbf{x},0) = 0, \quad \mathbf{A}(\mathbf{x},0) = (0,0) \quad \text{in } \Omega.
\end{array} \tag{3.45}$$

The variational form of (3.44) (Gao and Sun, 2018) is to find $\psi \in \mathcal{H}^1(\Omega)$ and $(\gamma, \mathbf{A}) \in \mathrm{H}^1(\Omega) \times \mathbf{H}_0(\operatorname{div})$ where $\gamma = H$ on $\partial\Omega$ such that

$$\left\{\begin{array}{l}
\left(\dfrac{\partial\psi}{\partial t}, w\right) - i\kappa\omega\left((\operatorname{div}(\mathbf{A})\psi, w\right) + \left(\left(\dfrac{1}{\kappa}\nabla - i\mathbf{A}\right)\psi, \left(\dfrac{1}{\kappa}\nabla - i\mathbf{A}\right)w\right)\\
\qquad + \left(\left(|\psi|^2 - 1\right)\psi, w\right) = 0 \quad \text{for all } w \in \mathcal{H}^1(\Omega),\\
(\gamma, \chi) - (\nabla\times\mathbf{A}, \chi) = 0 \quad \text{for all } \chi \in \mathrm{H}_0^1(\Omega),\\
\left(\dfrac{\partial\mathbf{A}}{\partial t}, \mathbf{v}\right) + (\nabla\times\gamma, \mathbf{v}) + (\omega \operatorname{div}\mathbf{A}, \operatorname{div}\mathbf{v}) - \dfrac{1}{2i\kappa}\left(\psi^*\nabla\psi - \psi\nabla\psi^*, \mathbf{v}\right)\\
\qquad + (|\psi|^2\mathbf{A}, \mathbf{v}) = (\nabla^\perp H, \mathbf{v}) \quad \text{for all } \mathbf{v} \in \mathbf{H}_0(\operatorname{div}),
\end{array}\right. \tag{3.46}$$

a.e. for $t \in (0,T)$ with $\psi(x,0) = \psi_0(x)$, $\gamma(x,0) = \nabla \times \mathbf{A}_0(x)$ and $\mathbf{A}(x,0) = \mathbf{A}_0(x)$.

A conformal approximation of the vector potential $\mathbf{A}$ in $\mathbf{H}(\text{div})$ is obtained by Raviart-Thomas FEs (for the theory of these elements see Boffi et al. (2013)). In the case of Raviart-Thomas FEs of degree 0, the degrees of freedom of $\mathbf{A}$ are the fluxes of $\mathbf{A}$ computed through the edges of each triangle. An important consequence is the continuity of the normal component of the approximated field at each edge. Triangular Raviart-Thomas FEs are available in FreeFEM for degree 0, 1 and 2 (denoted hereafter by RT0, RT1, RT2).
The homogenous boundary condition $\mathbf{A} \cdot \mathbf{n} = 0$ is simply implemented thanks to the function $on(\dots)$. ψ and γ are approximated by Lagrange FEs. Table 3.1 summarizes the possible choices for different degrees of finite elements:

	$\mathbf{A}$	ψ	γ
degree 0	RT0	P1	P1
degree 1	RT1	P1	P2
degree 2	RT2	P2	P3

Table 3.1. *Finite elements of various degrees used for each quantity.*

Now the transposition of the formulation (3.46) in FreeFEM syntax is:

```
varf vSys([sigma, A, Ay],[ki, v, vy]) =
  int2d(Th)(sigma*ki)
  + int2d(Th)(-1.*[A, Ay]'*Curl(ki))
  + int2d(Th)(1/dt*[A, Ay]'*[v,vy])
  + int2d(Th)(omega*div(A)*div(v))
  + int2d(Th)(Curl(sigma)'*[v,vy])
  + on(1, sigma = H, A = 0., Ay = 0.); // matrix for A

varf vrhsSys([sigma, A, Ay],[ki, v, vy]) =
  int2d(Th)(1/dt*[Aold, Aoldy]'*[v,vy])
  + int2d(Th)(opJs(psiold, psioldConj, Aold)'*[v,vy])
  + on(1, sigma = H, A = 0., Ay = 0.); // right-hand side for A

varf vPsi(psi, w) =  int2d(Th)(1/dt*psi*w + 1./kappa^2*Grad(psi)'*Grad(w));
// matrix for psi

varf vrhsPsi(psi,w) = int2d(Th)(1/dt*psiold*w)
  + int2d(Th)(I*kappa*omega*div(Aold)*psiold*w)
  + int2d(Th)(I/kappa*div(Aold)*psiold*w)
  + int2d(Th)(2*I/kappa*psiold*[Aold, Aoldy]'*Grad(w))
  + int2d(Th)(opN(psiold,Aold)*w); // right-hand side for psi
```

3.5.2. Examples

In this section, our goal is to retrieve classical benchmarks of the literature. In the first paragraph, we study three basic examples: the unit square, an L-shape domain and the disk. The goal is to show the effectiveness of the numerical schemes on convex and non-convex geometries. In the second paragraph, we study two classical benchmarks from the literature.

In all examples, the nondimensionalized form of the TDGL model corresponds to (3.22). We take $\mathbf{A}_0 = \mathbf{0}$ and $\psi_0 = 1$ (pure S state) as initial condition. Hereafter *mixed scheme* refers to the discretization of (3.46) and *Lagrange scheme* to the discretization of (3.43).

The parameters and energy of equilibrium state of each examples is summarized in Tab. 3.2. r denotes the degree of the finite element (see Tab. 3.1 for the mixed scheme). Δt is the chosen time step. M refers to the number of nodes per unit length of the mesh. $\mathcal{G}_{t_{max}}$ denotes the Gibbs free energy (3.23) computed at $t = t_{max}$:

	Scheme	r	ω	M	Δt	κ	H	t_{max}	$\mathcal{G}_{t_{max}}$
Example 1	Lagrange	1	0	100	0.05	10	3.5	500	0.2362
Example 2	Lagrange	1	0	100	0.05	10	5	500	0.2045
Example 3	Mixed	1	1	50	0.1	10	5	500	0.4873
Example 4	Lagrange	1	0	21	0.05	2	0.95	3000	51.1546
Example 5	Mixed	2	1	12	0.05	4	0.9	5000	16.4711

Table 3.2. *Parameters and energy of the final state in Examples 1-5.*

Basic examples

The unit square domain (Example 1) has been treated several times in the literature to test proposed numerical schemes (Du, 1994b; Yang, 2014; Li and Zhang, 2015; Gao et al., 2014). The L-shape domain (Example 2) has also been frequently used: it serves as a test on a non-convex geometry since the regularity of the solution is worse (Gao and Sun, 2018; Li and Zhang, 2015; Gao and Sun, 2015).

- *Example 1*: we consider the unit square $[0, 1]^2$. We set the GL parameter $\kappa = 10$ and the applied magnetic field $H = 3.5$. Figures 3.1-3.3 shows the results. Fig. 3.1 shows the evolution of the density $|\psi|$. We see two patterns that forms successively; at the beginning, vortices enter by each side all at once forming the metastable state shown at $t = 100$; then they slowly arrange themselves in an energetically more favourable pattern at $t = 500$.

  Figure 3.2 (left) shows the supercurrent at $t = 500$. Near the boundary, $\mathbf{J}_s$ rotates clockwise, opposing the applied field: it is a *shielding* current; around each vortex, $\mathbf{J}_s$ rotates counterclockwise producing a magnetic field shown on the right panel.

  In Fig. 3.3 we show the evolution of the energy and relative energy differences $\dfrac{|\mathcal{G}_{t+1} - \mathcal{G}_t|}{\mathcal{G}_t}$ (note that, in order to reduce the computational cost, we evaluate this expression only for integer values of t from 0 to t_{max}). The sharp decrease of the energy at the beginning corresponds to the entry of vortices; then, at $t \approx 200$, the energy is decreasing a little: it corresponds to the rotation of the vortex pattern; it is the cause of the bump observed on the relative energy differences plot.

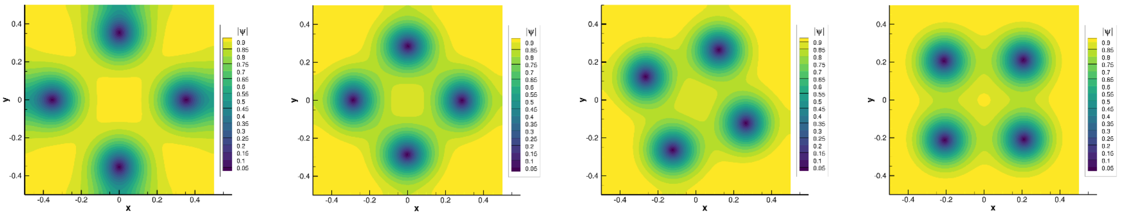

Figure 3.1. *Example 1. Density $|\psi|$ at instants $t = 10, 100, 250, 500$.*

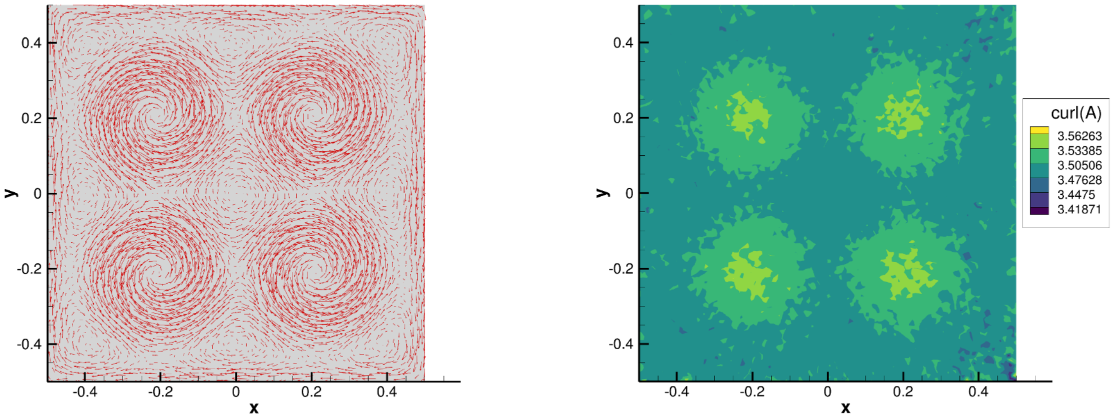

Figure 3.2. *Example 1. Supercurrent* $\boldsymbol{J}_s$ *(left) and magnetic field* $\nabla \times \boldsymbol{A}$ *(right).*

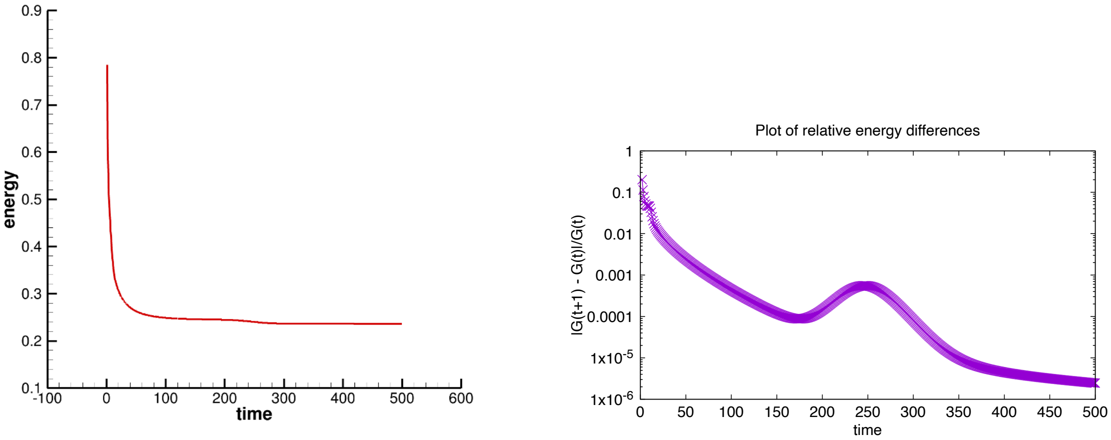

Figure 3.3. *Example 1. Evolution of the Gibbs energy (left) and relative energy differences* $|\mathcal{G}_{t+1} - \mathcal{G}_t|/\mathcal{G}_t$ *(right).*

- *Example 2*: we consider an L shape domain:

$$\overline{\Omega} := \{(x,y) \in [0,1]^2, x \leq 0.5 \text{ or } y \leq 0.5\}. \tag{3.47}$$

We set $\kappa = 10$ and $H = 5$. Figures 3.4-3.6 show the results. We see that the usual final state is recovered. It shows that the Lagrange scheme is efficient in non convex domains where the solution is expected to have low regularity (Li and Zhang, 2017).

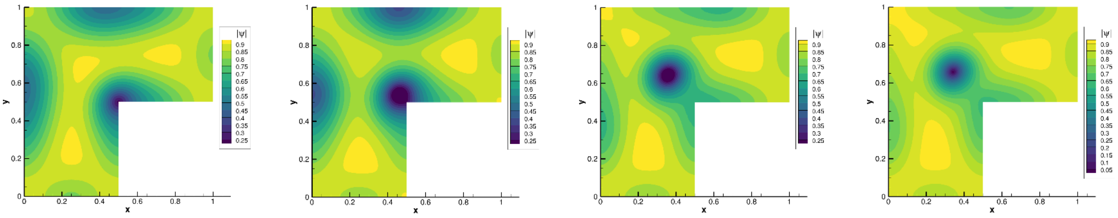

Figure 3.4. *Example 2. Density $|\psi|$ at instants $t = 2, 6, 20, 500$.*

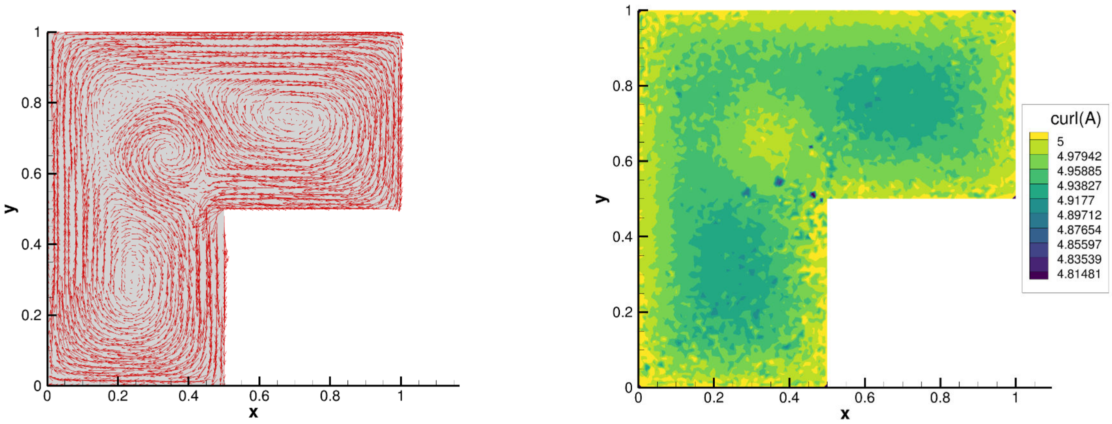

Figure 3.5. *Example 2. Supercurrent $\boldsymbol{J}_s$ (left) and magnetic field $\nabla \times \boldsymbol{A}$ (right).*

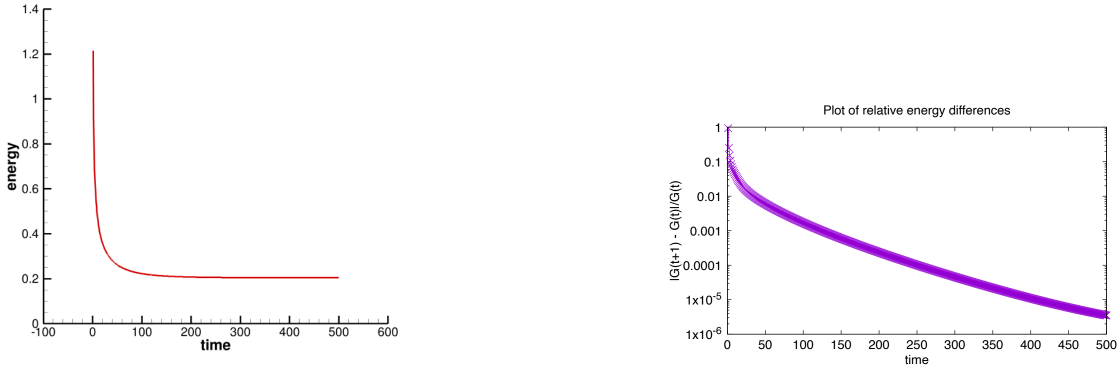

Figure 3.6. *Example 2. Evolution of the Gibbs energy (left) and relative energy differences $|\mathcal{G}_{t+1} - \mathcal{G}_t|/\mathcal{G}_t$ (right).*

- Example 3: we consider a disk of radius $R = \dfrac{\sqrt{2}}{2}$. We set $\kappa = 10$ and $H = 5$. Figures 3.7-3.9 show the results. In Fig. 3.7, we see that the vortices arrange in circle at $t \approx 50$. In Fig. 3.9, energy varies little until $t \approx 200$. This reflects the low values of relative energy differences (10^{-7}). The state is actually metastable and we observe that a vortex is slowly moving towards the centre of the disk at $t \approx 300$. This corresponds to the increase of relative energy differences seen in Fig. 3.9 between $t \approx 150$ and $t \approx 370$.

  We obtain a good approximation of the magnetic field shown in Fig. 3.8. The magnetic field $\nabla \times \mathbf{A}$ is introduced as a supplementary unknown in the mixed scheme, hence the convergence order is equal or even higher than the one for the vector potential (see Section 3.7).

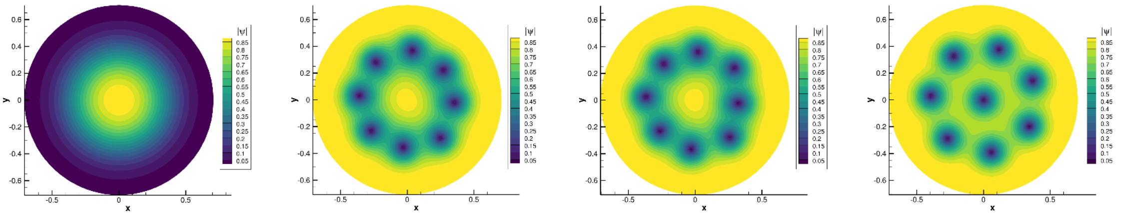

Figure 3.7. *Example 3. Density $|\psi|$ at instants $t = 5, 50, 300, 500$.*

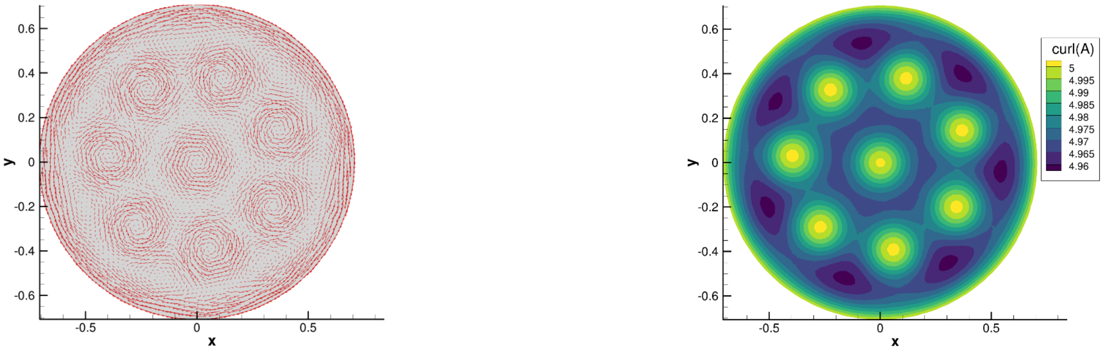

Figure 3.8. *Example 3. Supercurrent $\boldsymbol{J}_s$ (left) and magnetic field $\nabla \times \boldsymbol{A}$ (right).*

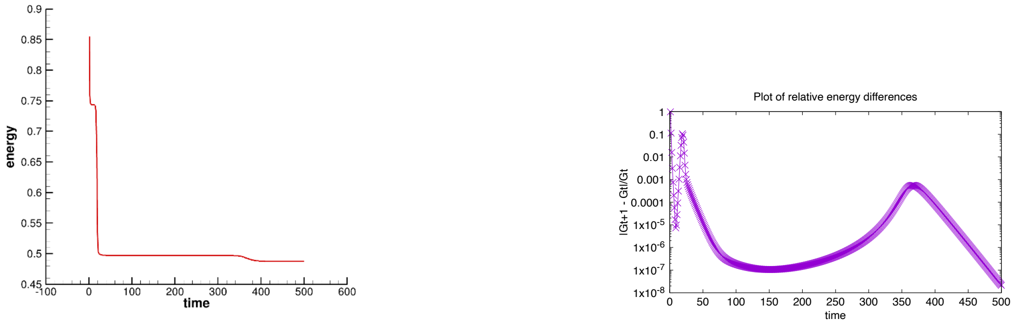

Figure 3.9. *Example 3. Evolution of the Gibbs energy (left) and relative energy differences $|\mathcal{G}_{t+1} - \mathcal{G}_t|/\mathcal{G}_t$ (right).*

Remark 3.5.1. *The boundary condition* $\boldsymbol{A} \cdot \boldsymbol{n} = 0$ *is naturally present in the mixed scheme. Indeed this condition reads as a homogenous Dirichlet condition in the case of Raviart-Thomas finite elements. In example 1 and 2 we use the Lagrange scheme. In this case the condition* $\boldsymbol{A} \cdot \boldsymbol{n} = 0$ *is satisfied by imposing* $A_x = 0$ *on edges parallel to the* y*-axis and* $A_y = 0$ *on edges parallel to the* x*-axis. Due to this constraint it has not been possible for us to use a Lagrange scheme on a general curved polygon. In the literature, Li and Zhang (2015) have reported a new formulation of the TDGL equations based on a Hodge decomposition of the vector potential written as the sum of its divergence-free part and curl-free part. The authors have built a scheme valid only in 2D where the condition* $\boldsymbol{A} \cdot \boldsymbol{n} = 0$ *does not appear explicitly.*

Benchmarks from the literature

- *Example 4*: this benchmark was first proposed by Gropp et al. (1996); we can also find it in Richardson et al. (2004).

  We consider a square $[-6, 6]^2$. We set $\kappa = 2$ and $H = 0.95$. The results are shown on Figs. 3.10-3.12. We observe that vortices arrange first in a metastable state at $t = 1000$. Then, the four central vortices rotate, forcing the peripheral ones to align in a perfect square array at $t = 3000$. These two consecutive moves reflect in the shape of the relative energy differences curve shown in Fig. 3.12.

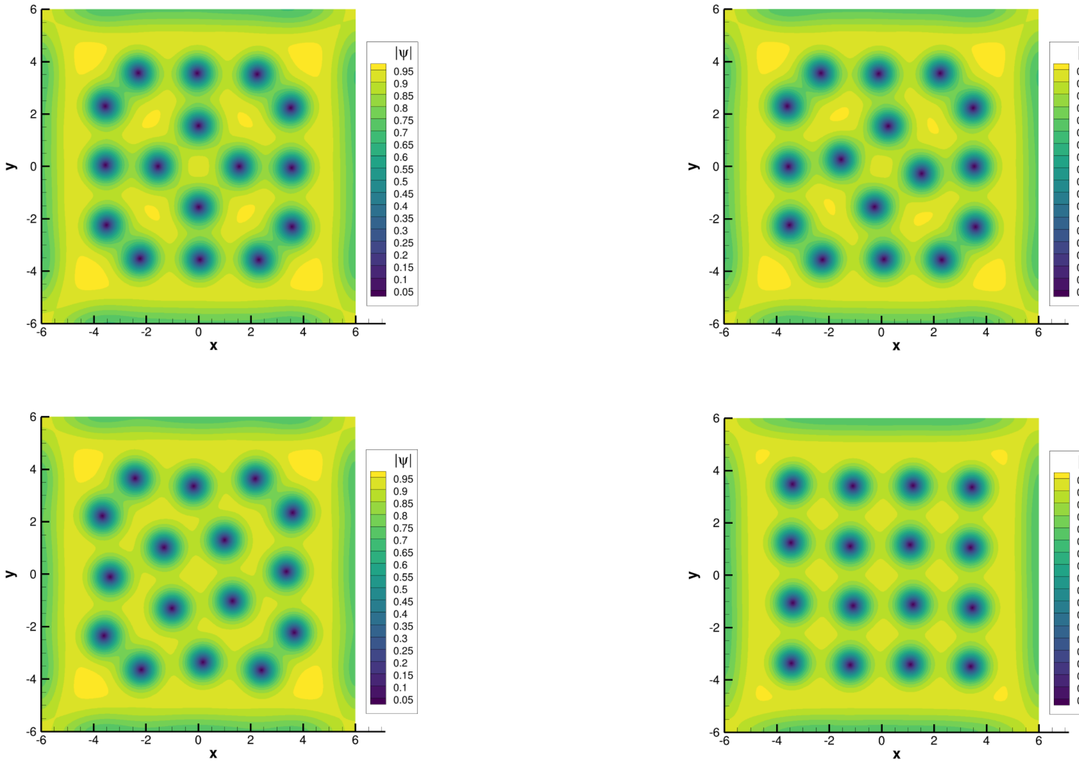

Figure 3.10. *Example 4. Density* $|\psi|$ *at instants* $t = 1000, 1300, 1400, 3000$.

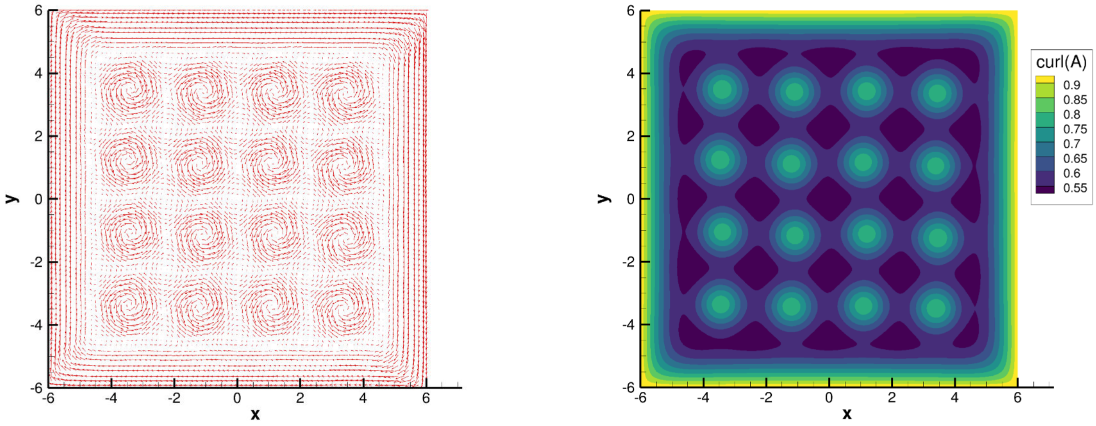

Figure 3.11. *Example 4. Supercurrent $\boldsymbol{J}_s$ (left) and magnetic field $\nabla \times \boldsymbol{A}$ (right).*

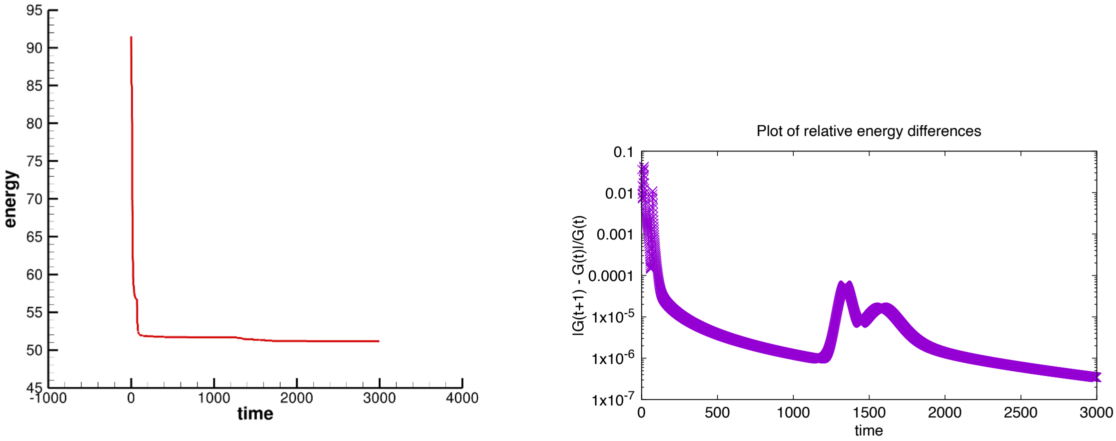

Figure 3.12. *Example 4. Evolution of the Gibbs energy (left) and relative energy differences $|\mathcal{G}_{t+1} - \mathcal{G}_t|/\mathcal{G}_t$ (right).*

- *Example 5* : this benchmark was originally studied by Alstrom et al. (2011). We also find it in Gao and Sun (2015), Li and Zhang (2015) and Gao (2017). The domain Ω consists of a disk with a triangular defect (see Fig. 3.13). In Alstrom et al. (2011), the authors use Lagrange finite elements and find equilibrium patterns with so called “giant vortices”. Since then, Gao and Sun (2015) have shown that Lagrange finite elements can lead to spurious solutions that may appear perfectly converged. In their article the authors, propose the scheme we have presented in Section 3.5.1, based on an approximation of $\mathbf{A}$ by Raviart-Thomas FEs. We consider here the case where $\kappa = 4$ and $H = 0.9$. Figures 3.14-3.16 show the results. From Fig. 3.14 we see that the vortices first enter the domain via the defect; then 17 vortices enter from the circular part of the boundary; at $t = 50$, the domain contains 20 vortices; eventually, the 21st vortex enter at $t = 200$. In total, 4 vortices have entered via the defect. The entrant corner appear to be a privileged location for the nucleation of vortices. This is closely related to the high value of the velocity $\mathbf{v}_s = \dfrac{1}{|\psi|^2}\mathbf{J}_s$ at that place (see Fig. 3.15). In Vodolazov et al. (2003), it is shown that the vortex nucleation is controlled by $\mathbf{v}_s$ on the sample surface. Specifically, if $|\mathbf{v}_s \times \mathbf{n}| > v_{cr}$, where $v_{cr} \approx 1$ is a critical value, then a modulation instability occurs at the edge. Moreover, the vortex entry field (i.e. the minimum field corresponding to an entry of a vortex) is lowered in the case of defects.

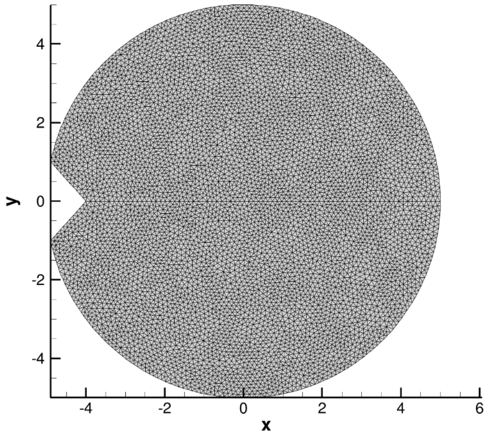

Figure 3.13. *Example 5. Symmetric mesh with respect to the* (Ox) *axis with* $M = 12$*.*

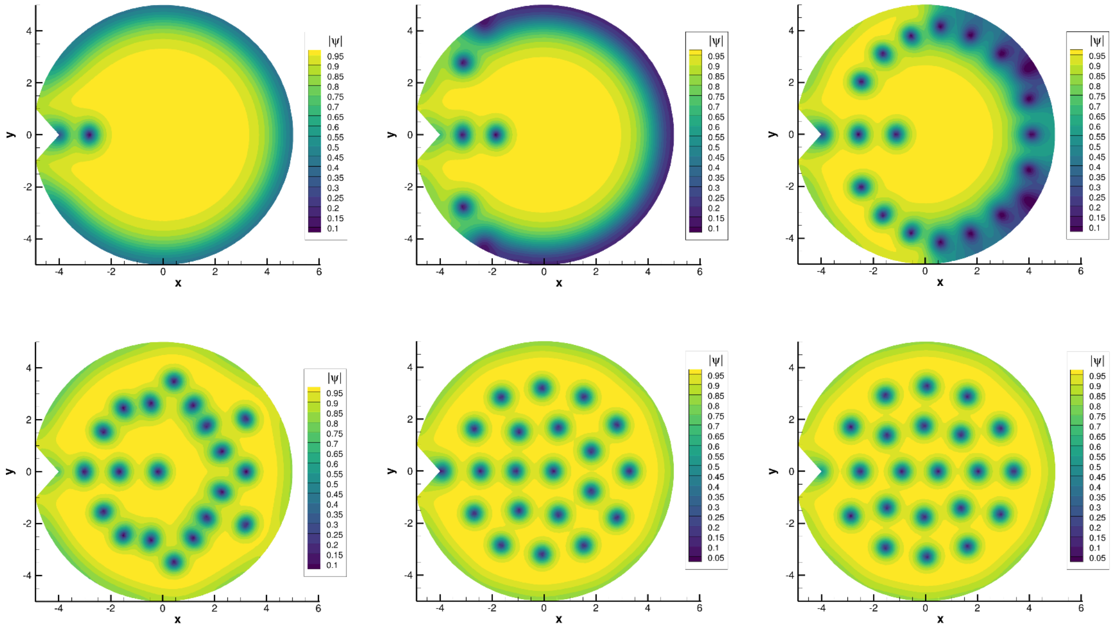

Figure 3.14. *Example 5. Density* $|\psi|$ *at instants* $t = 10, 20, 30$ *(above) and* $t = 50, 200, 5000$ *(below).*

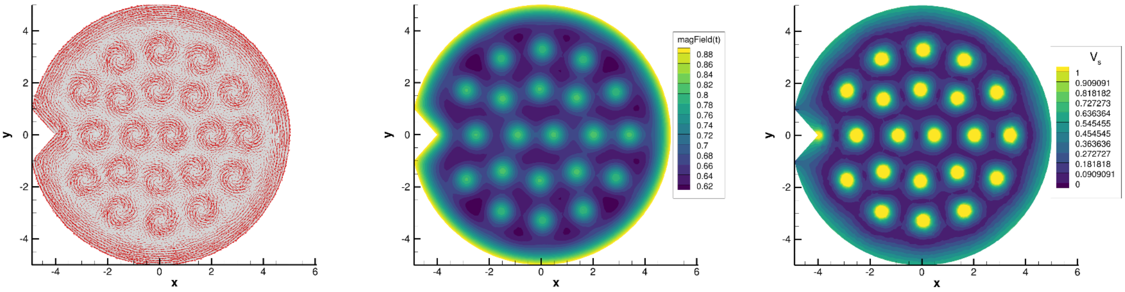

Figure 3.15. *Example 5. Supercurrent* $\boldsymbol{J}_s$ *(left) magnetic field* $\nabla \times \boldsymbol{A}$ *(middle) and velocity* $\boldsymbol{v}_s = \boldsymbol{J}_s/|\psi|^2$ *(right).*

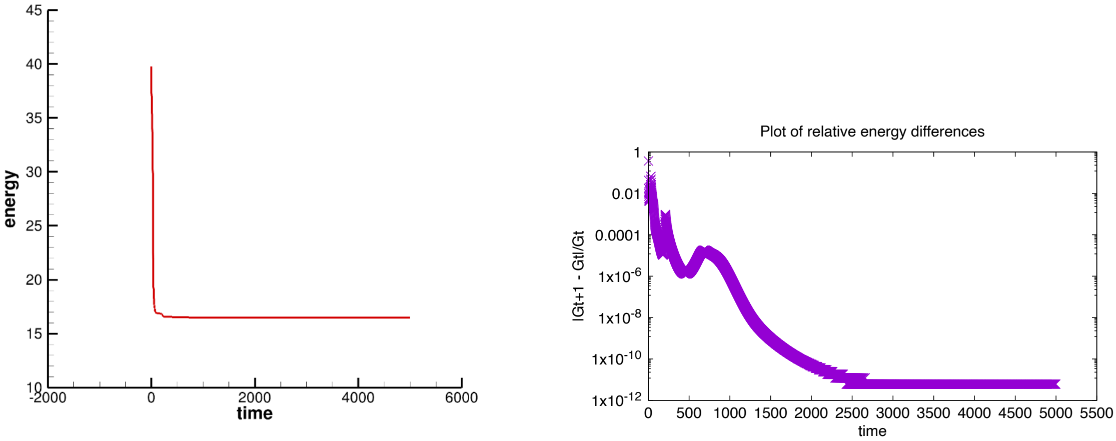

Figure 3.16. *Example 5. Evolution of the Gibbs energy (left) and relative energy differences* $|\mathcal{G}_{t+1} - \mathcal{G}_t|/\mathcal{G}_t$ *(right).*

3.6. Numerical results in 3D

In the previous section, we have studied the TDGL model in 2D. In 3D, numerical simulations are more challenging due to the high number of degrees of freedom. In the first paragraph, we describe the numerical schemes we have used. In the second paragraph, we present examples with different geometries: a cube, a parallelepiped with an inclined applied field, a sphere and a sphere with a boundary defect.

3.6.1. Numerical schemes

The Lagrange scheme presented in the previous section is used directly for the 3D case without modification. Thus, we only describe the mixed scheme. In 3D the magnetic field $\boldsymbol{\gamma} = \nabla \times \mathbf{A}$ is not a scalar as in the 2D case, but a vector. TDGL mixed formulation is:

$$\begin{aligned}
&\frac{\partial \psi}{\partial t} - i\kappa\omega \operatorname{div} \mathbf{A} = \left(\frac{1}{\kappa}\nabla - i\mathbf{A}\right)^2 \psi + \psi - |\psi|^2\psi \quad \text{in } \Omega,\\
&\boldsymbol{\gamma} = \nabla \times \mathbf{A} \quad \text{in } \Omega,\\
&\frac{\partial \mathbf{A}}{\partial t} - \omega\nabla \operatorname{div} \mathbf{A} + \nabla \times \boldsymbol{\gamma} = \frac{1}{2i\kappa}\left(\psi^*\nabla\psi - \psi\nabla\psi^*\right) - |\psi|^2\mathbf{A} + \nabla \times \mathbf{H} \quad \text{in } \Omega,
\end{aligned} \tag{3.48}$$

with boundary and initial conditions

$$\begin{aligned}
&\frac{\partial \psi}{\partial \mathbf{n}} = 0, \quad \boldsymbol{\gamma} \times \mathbf{n} = \mathbf{H} \times \mathbf{n}, \quad \mathbf{A} \cdot \mathbf{n} = 0 \quad \text{on } \Gamma,\\
&\psi(\mathbf{x}, 0) = 1, \quad \boldsymbol{\gamma}(\mathbf{x}, 0) = 0, \quad \mathbf{A}(\mathbf{x}, 0) = (0, 0) \quad \text{in } \Omega.
\end{aligned} \tag{3.49}$$

The variational form of (3.44) (Gao and Sun, 2018) is to find $\psi \in \mathcal{H}^1(\Omega)$ and $(\gamma, \mathbf{A}) \in \mathbf{H}(\text{curl}) \times \mathbf{H}_0(\text{div})$ where $\boldsymbol{\gamma} \times \mathbf{n} = \mathbf{H} \times \mathbf{n}$ on Γ, such that

$$\left\{\begin{aligned}
&\left(\frac{\partial \psi}{\partial t}, w\right) - i\kappa\omega \left((\operatorname{div}(\mathbf{A})\psi, w\right) + \left(\left(\frac{1}{\kappa}\nabla - i\mathbf{A}\right)\psi, \left(\frac{1}{\kappa}\nabla - i\mathbf{A}\right) w\right)\\
&\qquad + \left(\left(|\psi|^2 - 1\right)\psi, w\right) = 0 \quad \text{for all } w \in \mathcal{H}^1(\Omega),\\
&(\gamma, \boldsymbol{\chi}) - (\nabla \times \mathbf{A}, \boldsymbol{\chi}) = 0 \quad \text{for all } \chi \in \mathbf{H}_0(\text{curl}),\\
&\left(\frac{\partial \mathbf{A}}{\partial t}, \mathbf{v}\right) + (\nabla \times \gamma, \mathbf{v}) + (\omega \operatorname{div} \mathbf{A}, \operatorname{div} \mathbf{v}) - \frac{1}{2i\kappa}\left(\psi^*\nabla\psi - \psi\nabla\psi*, \mathbf{v}\right)\\
&\qquad + (|\psi|^2\mathbf{A}, \mathbf{v}) = (\nabla \times \mathbf{H}, \mathbf{v}) \quad \text{for all } \mathbf{v} \in \mathbf{H}_0(\text{div}),
\end{aligned}\right. \tag{3.50}$$

a.e. for $t \in (0, T)$ with $\psi(x, 0) = \psi_0(x)$, $\gamma(x, 0) = \nabla \times \mathbf{A}_0(x)$ and $\mathbf{A}(x, 0) = \mathbf{A}_0(x)$.

A conformal approximation of the magnetic field $\boldsymbol{\gamma}$ in $\mathbf{H}(\text{curl})$ is obtained by Nedelec FEs (for the theory of these elements see Boffi et al. (2013)). In the case of Nedelec FEs of degree 0, the degrees of freedom of the field are the integral of the field along the edges of each tetrahedron. An important consequence is the continuity of the tangential component of the approximated field at each edge. Tetrahedral Nedelec finite elements of degree 0, 1 and 2 are available in FreeFEM. In numerical examples, we use Nedelec FEs of degree 0.

The vector potential $\mathbf{A}$ is approximated by Raviart-Thomas FEs of degree 0 and ψ by linear Lagrange FEs P^1.

The transposition of formulation (3.50) in FreeFEM syntax is similar to the 2D case:

```
varf vSys([sigma, sigmay, sigmaz, A, Ay, Az],[ki, kiy, kiz, v, vy, vz]) =
  int3d(Th, mpirank)([sigma, sigmay, sigmaz]'*[ki, kiy, kiz])
  + int3d(Th, mpirank)(-1.*[A, Ay, Az]'*Curl(ki))
  + int3d(Th, mpirank)(1/dt*[A, Ay, Az]'*[v, vy, vz])
  + int3d(Th, mpirank)(omega*div(A)*div(v))
  + int3d(Th, mpirank)(Curl(sigma)'*[v, vy, vz])
  + on(1, sigma = Bax, sigmay = Bay, sigmaz = Baz, A = 0., Ay = 0., Az = 0.);
// matrix for A

varf vrhsSys([sigma, sigmay, sigmaz, A, Ay, Az],[ki, kiy, kiz, v, vy, vz]) =
  int3d(Th, mpirank)(1/dt*[Aold, Aoldy, Aoldz]'*[v,vy,vz])
  + int3d(Th, mpirank)(opJs(psiold, psioldConj, Aold)'*[v, vy, vz])
  + on(1, sigma = Bax, sigmay = Bay, sigmaz = Baz, A = 0., Ay = 0., Az = 0);
// right-hand side for A


varf vPsi(psi, w) =  int3d(Th,mpirank)(1/dt*psi*w + 1./kappa^2*Grad(psi)'*Grad(w));
// matrix for psi

varf vrhsPsi(psi,w) = int3d(Th,mpirank)(1/dt*psiold*w)
  + int3d(Th,mpirank)(I*kappa*omega*div(Aold)*psiold*w)
  + int3d(Th,mpirank)(I/kappa*div(Aold)*psiold*w)
  + int3d(Th,mpirank)(2*I/kappa*psiold*[Aold, Aoldy, Aoldz]'*Grad(w))
  + int3d(Th,mpirank)(opN(psiold,Aold)*w); // right-hand side for psi
```

3.6.2. Examples

In this paragraph we analyse some particular geometries, some of them extracted the literature. The cube has been treated in Gao and Sun (2015), the parallelepiped with inclined applied field in Richardson et al. (2004); the sphere and the sphere with a geometrical defect are original. In Tab. 3.3, we report the parameters of the model and the energy of the final configuration $\mathcal{G}_{t_{max}}$.

	Scheme	r	ω	M	Δt	κ	**H**	t_{max}	$\mathcal{G}_{t_{max}}$
example 1	Mixed	0	1	30	0.1	10	(0,0,3.5)	500	0.2084
example 2	Mixed	0	1	6	0.1	2	(0.3,0.3,1)	500	50.7318
example 3	Mixed	0	1	30	0.1	10	(0,0,5)	500	0.4888
example 4	Mixed	0	1	30	0.1	10	(0,0,5)	500	0.4869

Table 3.3. *Parameters and energy of the final state in Examples 1-4.*

- *Example 1*: we consider the unit cube $\left[-\frac{1}{2},\frac{1}{2}\right]^3$. We set $\kappa = 10$ and $\mathbf{H} = (0,0,3.5)$. We use a uniform mesh with $M = 30$ (i.e. three nodes per unit of the coherence length ξ). The results are shown on Figs. 3.17-3.20. In Fig. 3.17, we observe a metastable state with 4 vortices at $t = 100$; however one vortex is ejected at $t \approx 185$; three vortices remain afterwards and arrange in a regular triangle shape. It is somewhat surprising since in 2D (see Example 1, Section 3.5.2), with identical parameters, the four vortices rotate to form a square. We would expect the same behaviour in 3D. It is not due to the choice of the mixed scheme, since the Lagrange scheme gives the same result. It may be due to the mesh since the 2D case is much more refined (10 nodes per ξ); a finite thickness effect is also possible.

  The magnetic field is shown in Fig. 3.18. We observe that isovalues are very close. It is due to the relatively high value for κ. In the limit $\kappa \to \infty$, we would obtain a uniform field. Flux tubes are shown on the right panel. We see that the tubes are straight, hence there is no surface effect. This could be surprising since in type I superconductors, it is known that flux tubes become larger near the surface (de Gennes, 1966).

In Fig. 3.20, the energy shows a dramatic decrease due to the loss of one vortex at $t \approx 185$. It is worth noting that relative energy differences are increasing as soon as $t \approx 50$. Relative energy differences is a reliable indicator to tell whether the current state is going to evolve or not.

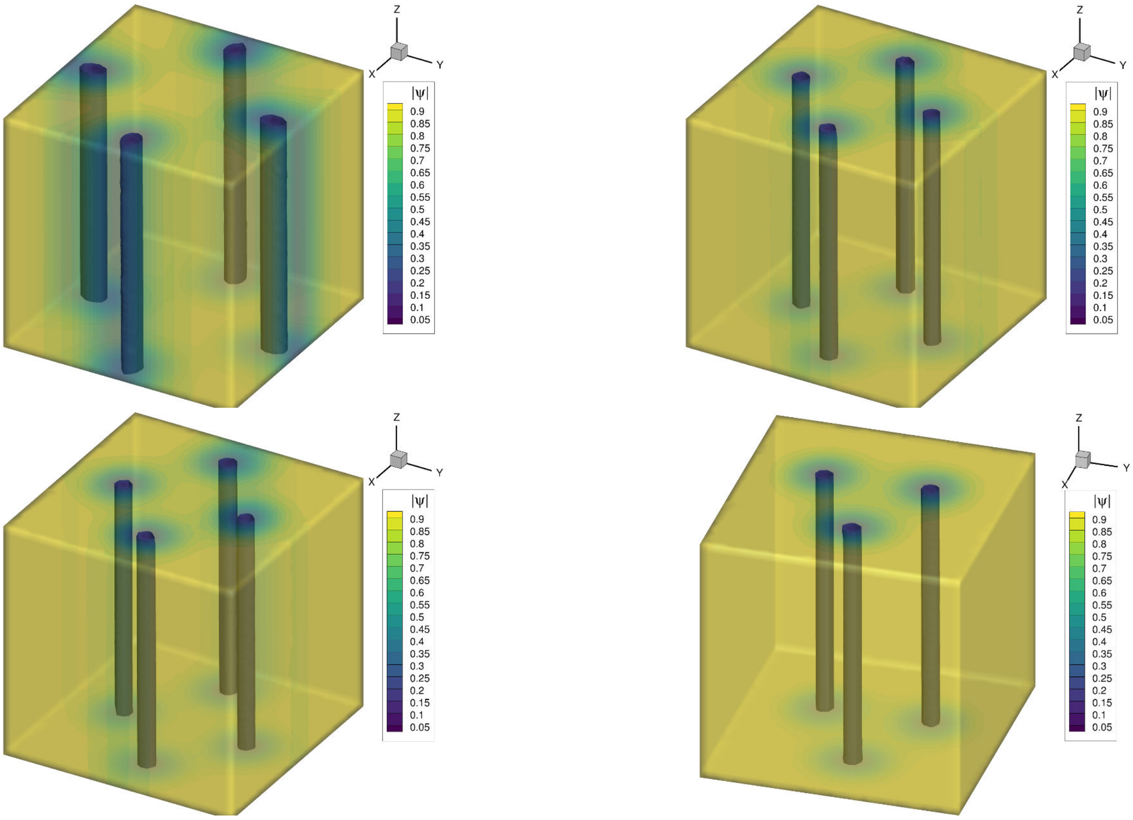

Figure 3.17. *Example 1. Isosurfaces of the density* $|\psi| = 0.25$ *at* $t = 10, 100, 180, 500$.

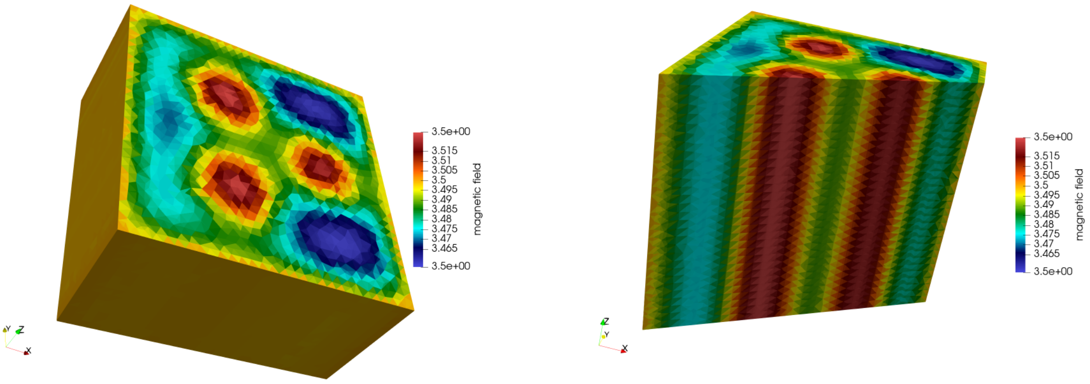

Figure 3.18. *Example 1. Section of the magnetic field along the plane* $z = 0$ *at* $t = 500$ *(left), section of the magnetic field along a plane of normal* $\boldsymbol{n} = (-0.55, 0.83, 0)$ *at* $t = 500$ *(right).*

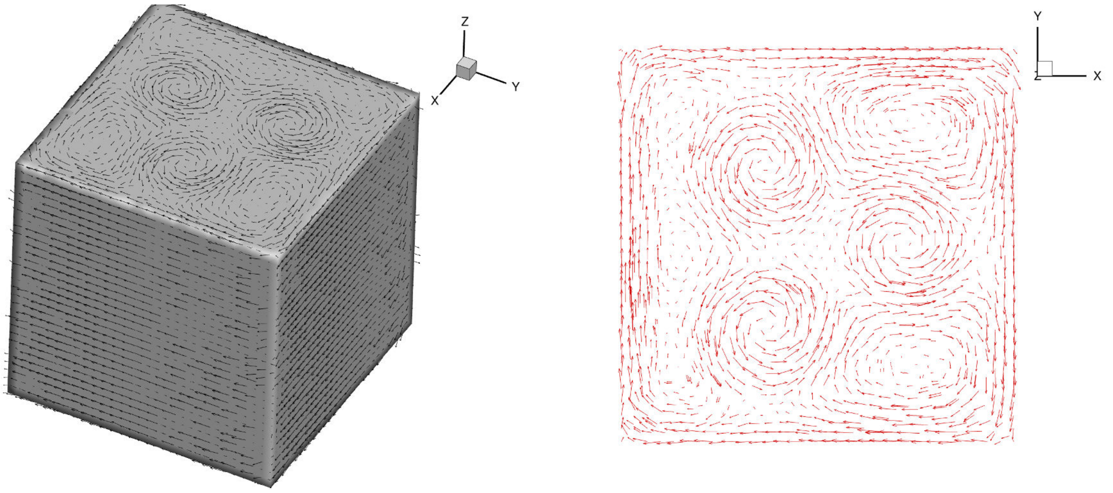

Figure 3.19. *Example 1. Supercurrent $\boldsymbol{J}_s$ on the surface at $t = 500$ (left), supercurrent on the mid-plane at $t = 500$ (right).*

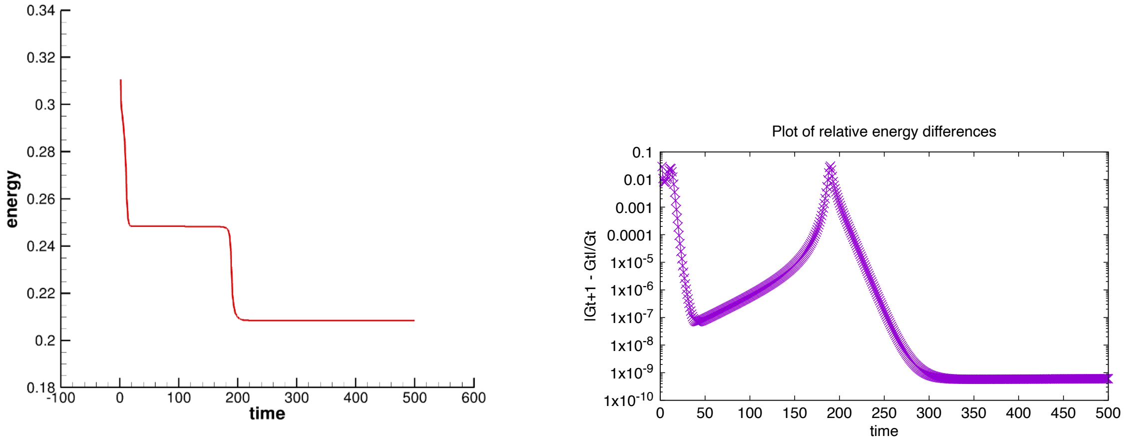

Figure 3.20. *Example 1. Evolution of the Gibbs energy (left) and relative energy differences $|\mathcal{G}_{t+1} - \mathcal{G}_t|/\mathcal{G}_t$ (right).*

- *Example 2*: we consider a parallelepiped $\left[0, \dfrac{20}{3}\right] \times \left[0, \dfrac{20}{3}\right] \times \left[0, \dfrac{10}{3}\right]$. We set $\kappa = 2$ and $\mathbf{H} = (0.3, 0.3, 1)$. We use a uniform mesh with $M = 30$. The results are shown in Figs. 3.21-3.24. In Fig. 3.21 we observe that, at $t = 100$, the state is not stable and at $t = 500$, vortices have rotated by $-45°$ using the right hand rule. We see that vortices are inclined along the applied field and meet the upper surface along the normal. It is due to surface currents shown in Fig. 3.23. These currents flow in circles in a plane perpendicular to the z-axis; as a consequence they locally induce a magnetic field along the z-axis that distorts the vortices near the edges. The interior of flux tubes is shown in Fig. 3.22. We clearly see that the diameter of the tubes are larger near the surface.

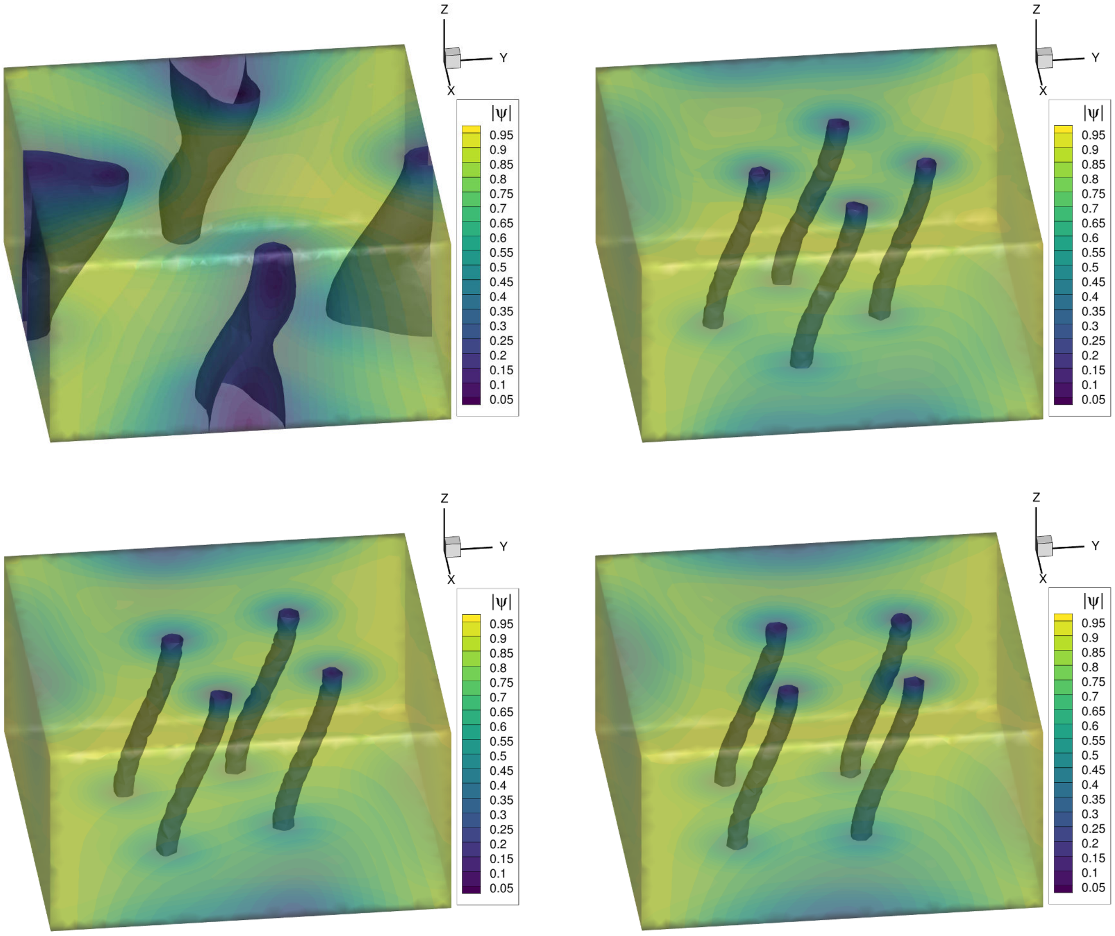

Figure 3.21. *Example 2. Isosurfaces of the density* $|\psi| = 0.25$ *at instants* $t = 10, 100, 250, 500$.

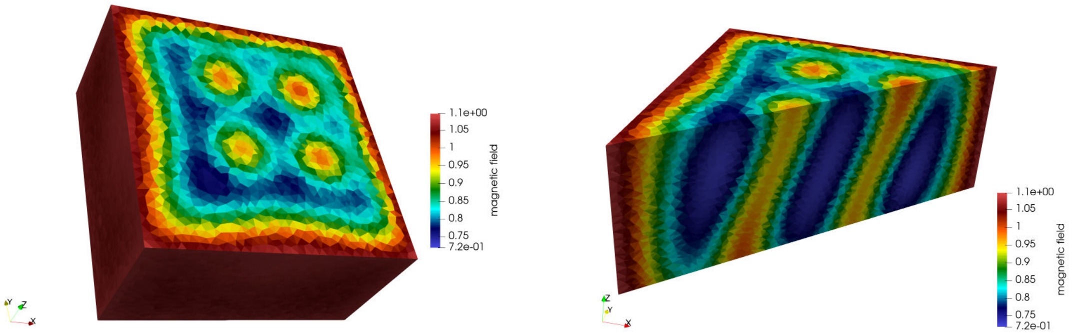

Figure 3.22. *Example 2. Magnetic field at* $t = 500$ *(left), section of the magnetic field along the plane* $x - y = 0$ *(right).*

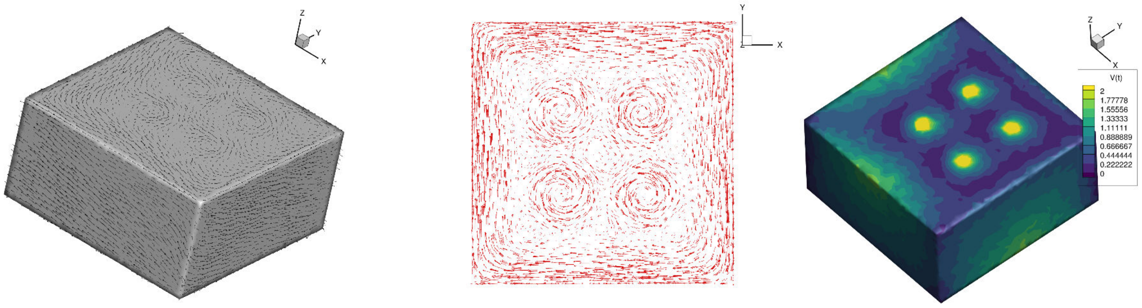

Figure 3.23. *Example 2. Supercurrent* $\boldsymbol{J}_s$ *on the surface at* $t = 500$ *(left), supercurrent on the mid-plane (middle), supervelocity* $\boldsymbol{v}_s = \boldsymbol{J}_s/|\psi|^2$ *at* $t = 500$ *(right).*

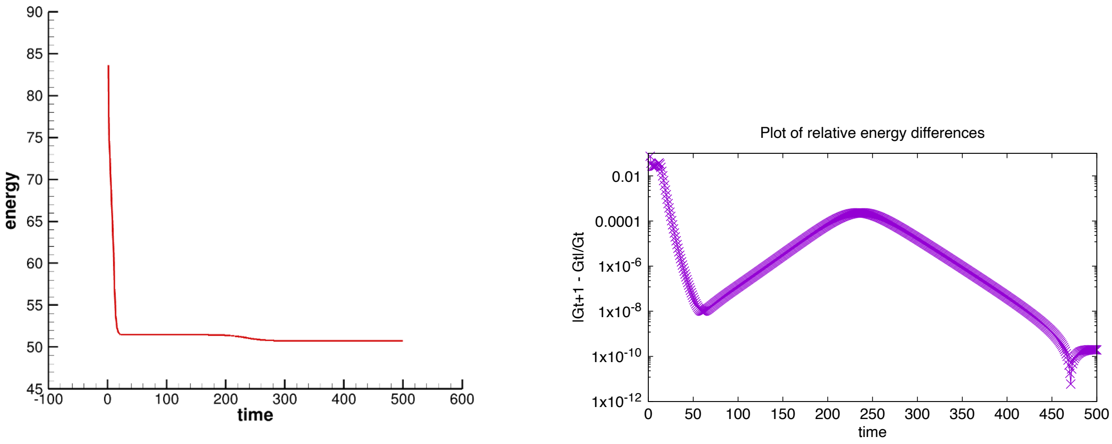

Figure 3.24. *Example 2. Evolution of the Gibbs energy (left) and relative energy differences* $|\mathcal{G}_{t+1} - \mathcal{G}_t|/\mathcal{G}_t$ *(right).*

- *Example 3*: we consider a sphere of radius $R = \frac{\sqrt{2}}{2}$. We set $\kappa = 10$ and the applied field is $\mathbf{H} = (0, 0, 5)$. Figures 3.25-3.29 show the results. We use a uniform tetrahedral mesh with $M = 30$. In Fig. 3.25, we see that vortices nucleate from the equator; this happens because the supervelocity is maximum at the equator (see Fig. 3.28 at $t = 10$). At $t = 30$, we observe 8 vortices but, at $t = 40$, only 7 remain. Afterwards, they slowly arrange in an hexagonal lattice with a central vortex. Vortex lines are straight in the middle since they are aligned with the applied magnetic field which is along the z-axis. In addition they meet the sphere along its normal: it is due to the currents on the surface shown in Fig. 3.27; these currents induce a magnetic field locally aligned with the normal (see the isovalues of the magnetic field shown on Fig. 3.26).

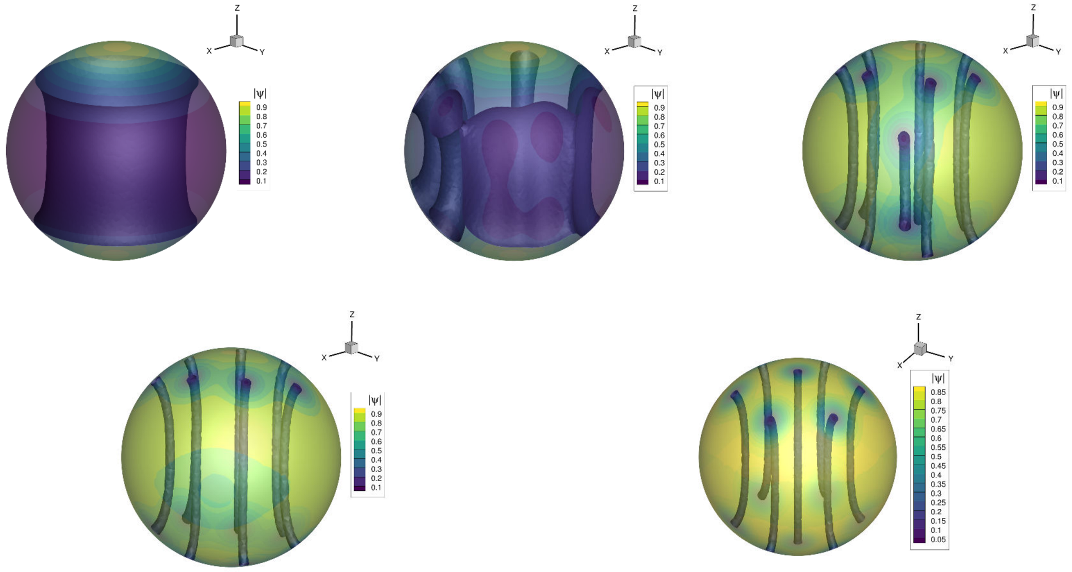

Figure 3.25. *Example 3. Isosurfaces of the density $|\psi| = 0.2$ at $t = 10, 20, 30$ (above) and $t = 40, 500$ (below).*

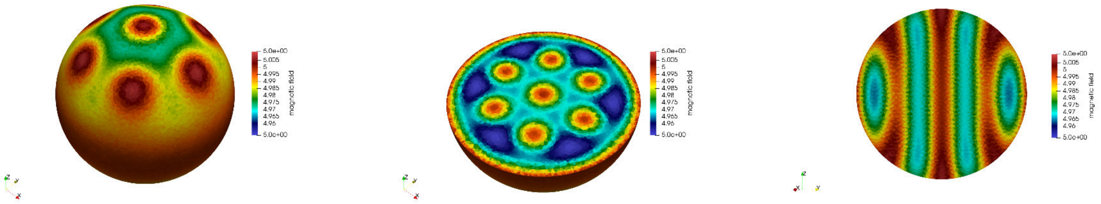

Figure 3.26. *Example 3. Magnetic field $\nabla \times \mathbf{A}$ (left), section of the magnetic field along the equatorial plane (middle), magnetic field $\nabla \times \mathbf{A}$ along the z-axis (right).*

Figure 3.27. *Example 3. Section along the equatorial plane of supercurrent $\boldsymbol{J}_s$ (left), view of the surface currents (right).*

Figure 3.28. *Example 3. Supervelocity $\boldsymbol{v}_s = \boldsymbol{J}_s/|\psi|^2$ at instants $t = 10$ (left) and $t = 20$ (right).*

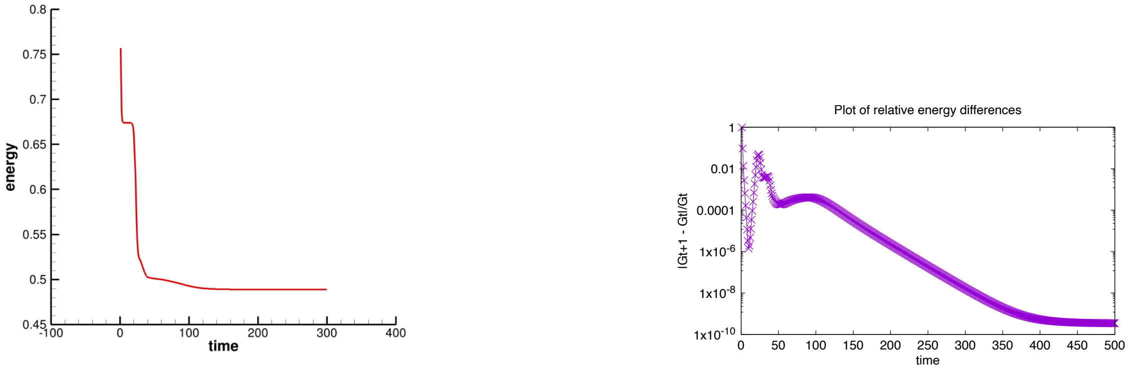

Figure 3.29. *Example 3. Evolution of the Gibbs energy (left) and relative energy differences $|\mathcal{G}_{t+1} - \mathcal{G}_t|/\mathcal{G}_t$ (right).*

- *Example 4*: we consider a sphere of radius $R = \dfrac{\sqrt{2}}{2}$ with a geometrical defect (see Fig. 3.30). We set $\kappa = 10$ and $\mathbf{H} = (0, 0, 5)$. Figures 3.31-3.35 show the results. We use a uniform tetrahedral mesh with $M = 30$. In Figs. 3.31-3.32, at $t = 5$, we see that the first vortex enters the domain via the defect; the other 6 vortices then nucleates from the equator; eventually, at $t = 500$, the pattern is identical to the case of the sphere without defect. The supervelocity, shown in Fig. 3.33, highlights the role of the defect. We observe that v_s is maximum in the vicinity of the defect from the very beginning. This inhomogeneity of v_s appear to enhance the nucleation of vortices at the defect, but also nearby, as can be seen from Fig. 3.32 at $t = 10$.

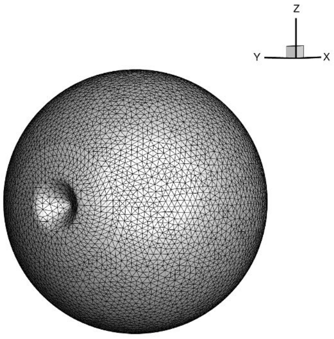

Figure 3.30. *Example 4. Tetrahedral mesh with* $M = 30$.

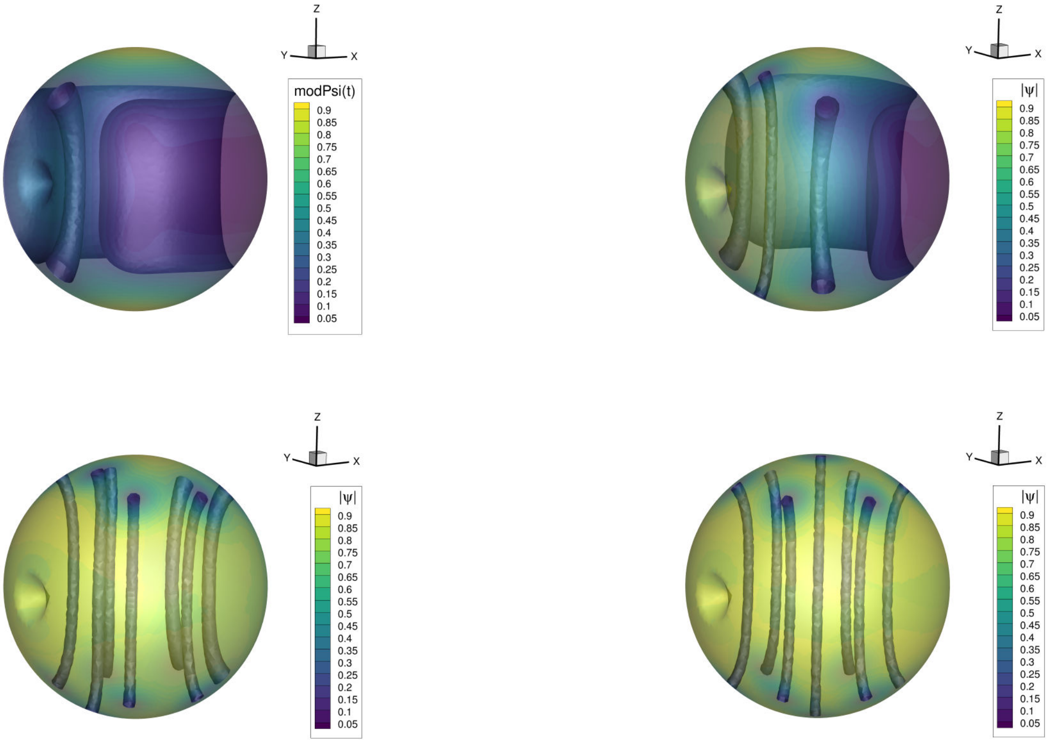

Figure 3.31. *Example 4. Isosurfaces of the density* $|\psi| = 0.2$ *at* $t = 5, 10, 20, 500$.

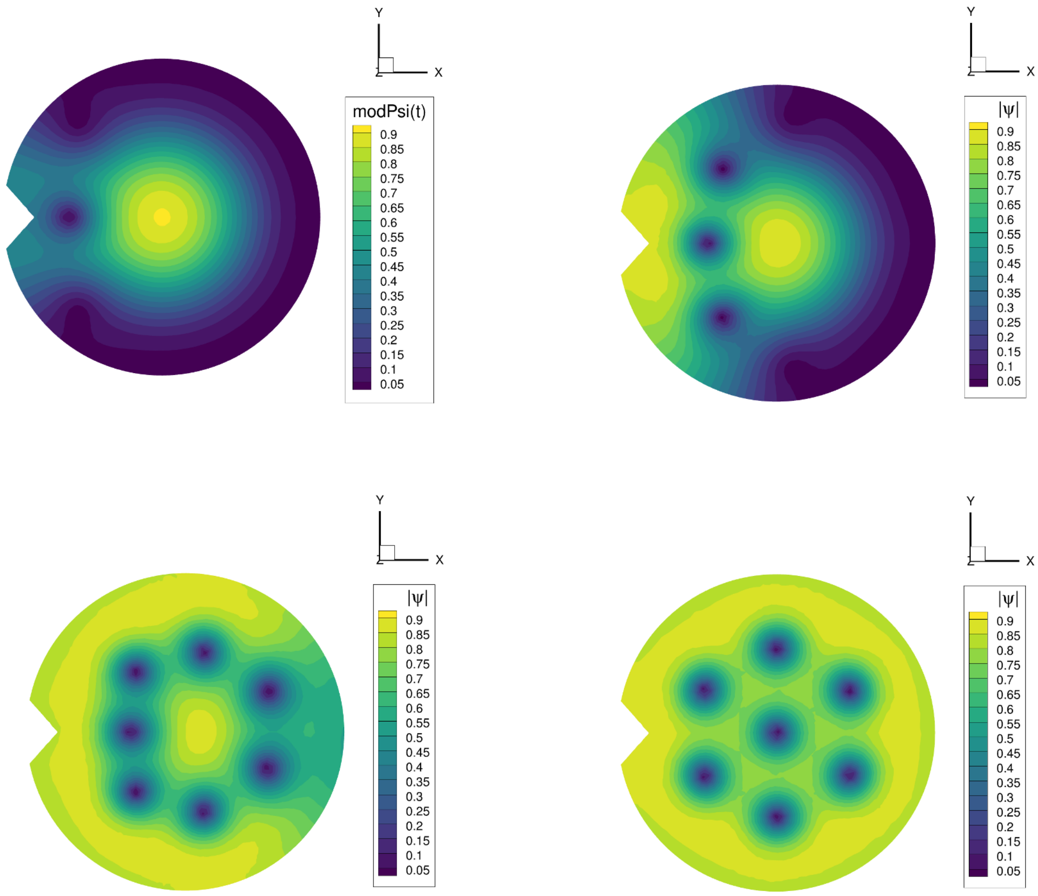

Figure 3.32. *Example 4. Sections along the equatorial plane of the density at* $t = 5, 10, 20, 500$.

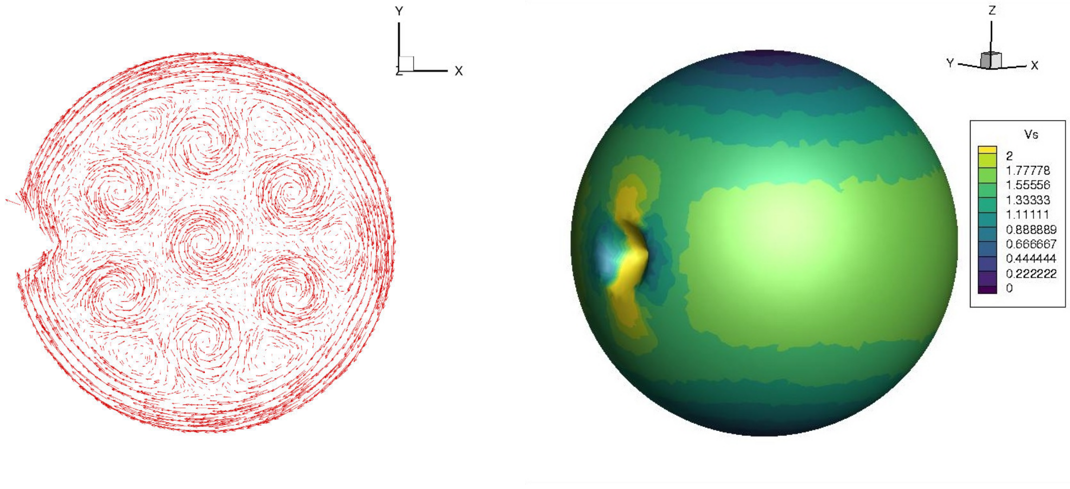

Figure 3.33. *Example 4. Section of the supercurrent* $\boldsymbol{J}_s$ *at* $t = 500$ *along the equatorial plane (left), supervelocity* $\boldsymbol{v}_s = \boldsymbol{J}_s/|\psi|^2$ *at* $t = 1$ *(right).*

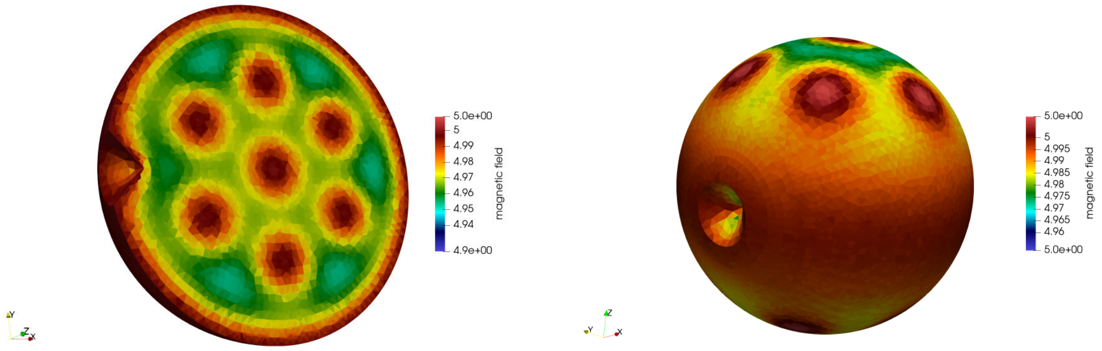

Figure 3.34. *Example 4. Section of the magnetic field at* $t = 500$ *along the equatorial plane (left), magnetic field on the surface (right).*

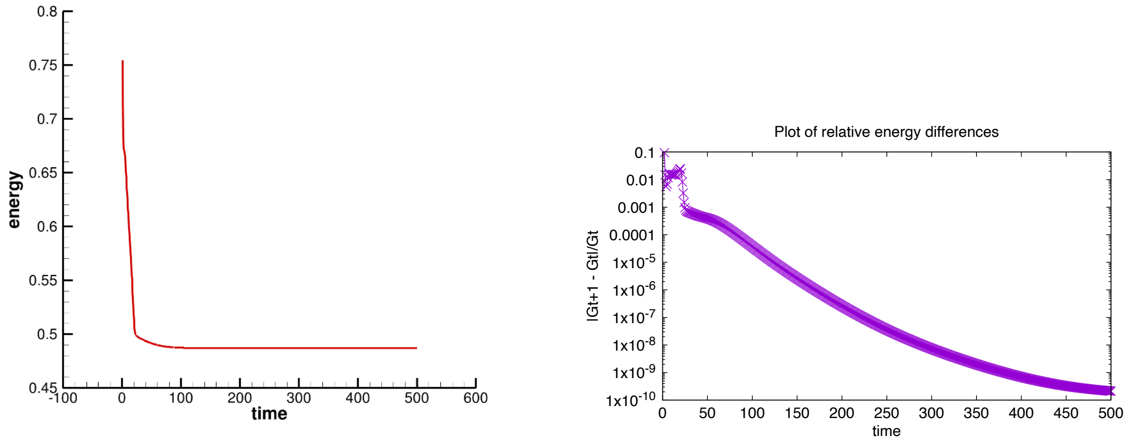

Figure 3.35. *Example 4. Evolution of the Gibbs energy (left) and relative energy differences* $|\mathcal{G}_{t+1} - \mathcal{G}_t|/\mathcal{G}_t$ *(right).*

3.7. Influence of the gauge parameter

In this section we conduct a detailed study of convergence orders for the mixed scheme using the general ω-gauge (3.34). In the first paragraph we come back to Example 3.5.2; that allows us to study the role of the ω-gauge via the parameter ω and the degree r of finite elements. In the second paragraph, we study the convergence orders for the mixed scheme using two different techniques. We conclude on the existence of an optimal gauge for some $\omega_0 \in (0, 1)$.

3.7.1. Study of a benchmark in non convex geometry

We give here a detailed numerical description of Example 3.5.2 when the gauge parameter ω and the degree r of finite elements vary.

We set the applied field $H = 0.9$ and $\kappa = 4$. The number of nodes per unit of coherence length is 3, corresponding to $M = 12$. Figure 3.36 shows the vortex patterns at $t = 5000$ in the case $r = 1$ for different values of ω. We observe a normal zone (i.e. a zone where $|\psi| = 0$) growing near the indent when ω is decreasing. It indicates that our scheme is becoming less efficient for that mesh size and values of ω close enough to 0. This issue is standard in TDGL numerical treatment and can be solved by a refinement of the mesh (Richardson et al., 2004).

In Fig. 3.37, we show the results in the case $r = 2$ and Tab. 3.4 reports details about the observed vortex patterns. We do not see any normal zone; however the final state varies with ω which contradicts the gauge invariance property. Moreover, we see that the pattern we called *circle* with 21 vortices is not the one with the lowest energy. The pattern *circle* is the one we usually find in the literature (Gao and Sun, 2015; Li and Zhang, 2015; Gao, 2017). In Chapter 4, we will present other original states of lowest energy for this geometry.

Figures 3.38 and 3.39 show the relative energy differences $\dfrac{|\mathcal{G}_{t+1} - \mathcal{G}_t|}{\mathcal{G}_t}$, for $t = 0 \ldots 5000$, in the Lorentz and temporal gauge. Clearly the convergence is much better in the Lorentz gauge. The results for other values of ω indicate that the convergence is improving when we increase ω. Moreover, for each gauge, the convergence also improves when r is larger.

ω	Pattern type (Number of vortices)	$\lvert\mathcal{G}_{t+1} - \mathcal{G}_t\rvert$ at $t = t_{max}$	$\mathcal{G}_{t_{max}}$	t_{max}
1	line 1 (21)	$< 10^{-10}$	16.4711	5000
10^{-1}	line 1 (21)	$< 10^{-10}$	16.4711	5000
10^{-2}	line 2 (22)	1.6×10^{-7}	16.0959	5000
10^{-3}	circle (21)	7.4×10^{-8}	16.4362	5000
10^{-4}	circle (21)	4.3×10^{-7}	16.4310	5000
0	circle (21)	1.3×10^{-6}	16.4338	5000

Table 3.4. *Case r = 2. Characteristics of equilibrium patterns for each ω.*

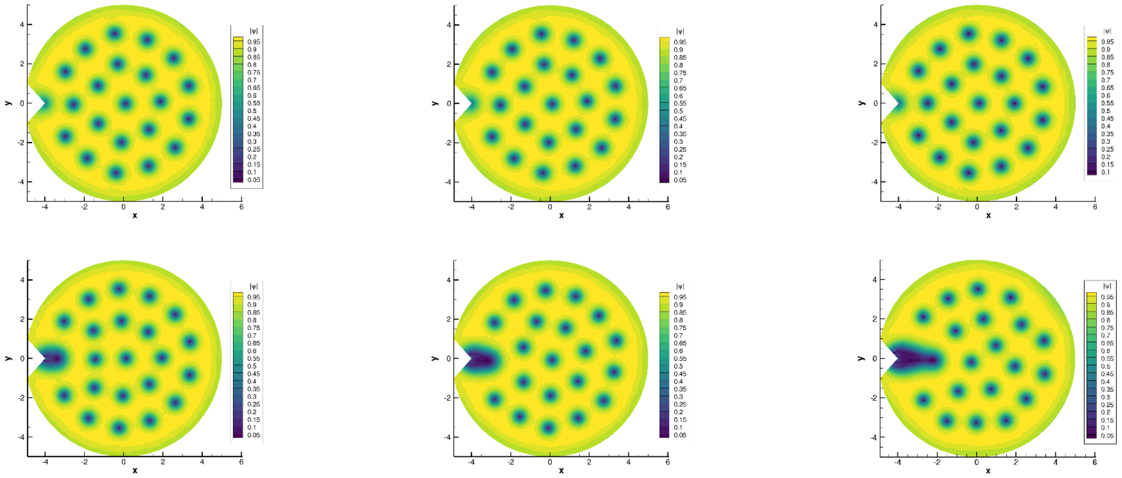

Figure 3.36. *Case r = 1. Vortex patterns for the disk with a boundary defect for different values of the* ω *parameter (from left to right and top to bottom :* $\omega = 1, 10^{-1}, 10^{-2}, 10^{-3}, 10^{-4}, 0$*).*

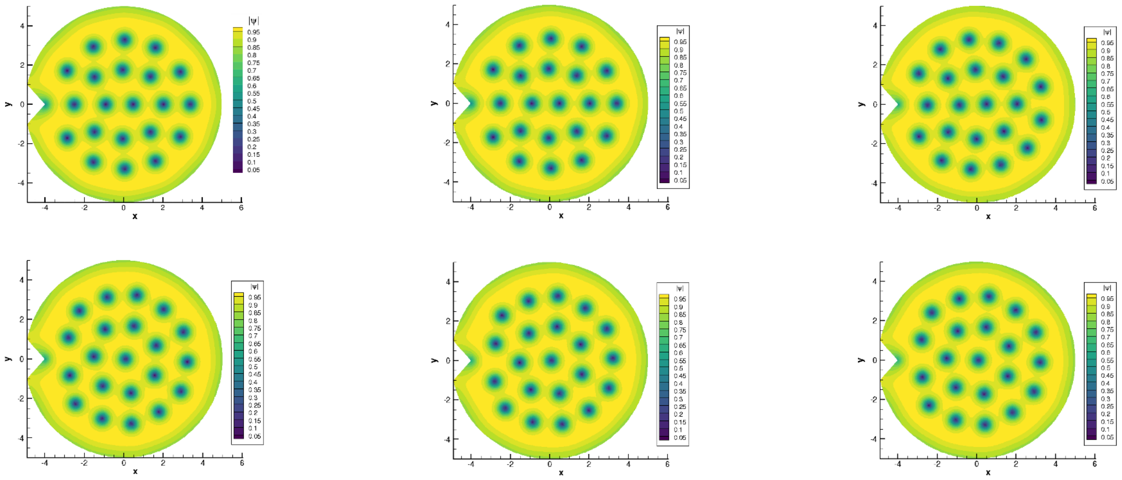

Figure 3.37. *Case r = 2. Vortex patterns for the disk with a boundary defect for different values of the* ω *parameter (from left to right and top to bottom :* $\omega = 1, 10^{-1}, 10^{-2}, 10^{-3}, 10^{-4}, 0$*).*

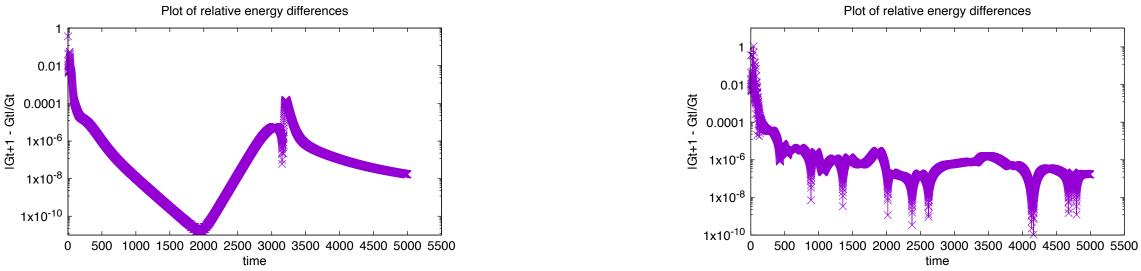

Figure 3.38. *Case r = 1. Relative Energy difference* $|\mathcal{G}_{t+1} - \mathcal{G}_t|/\mathcal{G}_t$ *in logarithmic scale for the Lorentz gauge (left) and in the temporal gauge (right).*

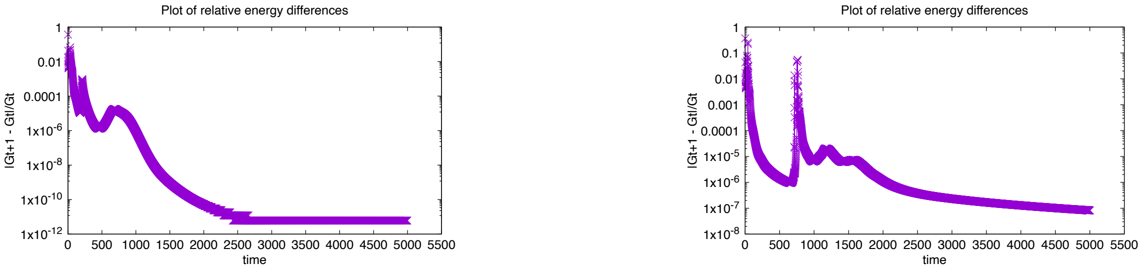

Figure 3.39. *Case r = 2. Relative energy difference* $|\mathcal{G}_{t+1} - \mathcal{G}_t|/\mathcal{G}_t$ *in logarithmic scale for the Lorentz gauge (left) and in the temporal gauge (right).*

3.7.2. Convergence analysis of the mixed scheme when $r = 1$

We present in this paragraph two techniques: a graphic method inspired by Gao and Sun (2015) and the Richardson extrapolation technique. The graphical method is very accurate since it computes directly the difference between the exact solution of our equations and the ones computed with the numerical scheme. The drawback is that it is highly time consuming. The Richardson extrapolation technique is fast and accurate but relies on parameters chosen ”by hand”.

Before starting the analysis itself, we introduce the *manufactured* system we use. We call it manufactured since it is built in such a way that we know the exact solution of this system. In our case it is defined on the unit square $[0,1]^2$ and the equations read:

$$\begin{aligned} &\frac{\partial \psi}{\partial t} - i\kappa\omega \operatorname{div} \mathbf{A} - \left(\frac{1}{\kappa}\nabla - i\mathbf{A}\right)^2 \psi - \psi + |\psi|^2\psi = g \quad \text{in } \Omega, \\ &\frac{\partial \mathbf{A}}{\partial t} - \omega\nabla \operatorname{div} \mathbf{A} + \nabla\times\nabla\times\mathbf{A} - \frac{1}{2i\kappa}\left(\psi^*\nabla\psi - \psi\nabla\psi^*\right) + |\psi|^2\mathbf{A} = \nabla\times\mathbf{H} + \mathbf{f} \quad \text{in } \Omega, \end{aligned} \tag{3.51}$$

with boundary and initial conditions

$$\nabla\psi\cdot\mathbf{n} = 0, \quad \nabla\times\mathbf{A} = H, \quad \mathbf{A}\cdot\mathbf{n} = 0 \quad \text{on } \Gamma. \tag{3.52}$$

f and g are defined such that the exact solution of (3.51) is:

$$\begin{aligned} &\psi = \exp(-t)\left(\cos(\pi x) + i\cos(\pi y)\right), \\ &\mathbf{A} = \begin{pmatrix} \exp(y-t)\sin(\pi x) \\ \exp(x-t)\sin(\pi y) \end{pmatrix}, \\ &H = \exp(x-t)\sin(\pi y) - \exp(y-t)\sin(\pi x). \end{aligned} \tag{3.53}$$

The graphical method

We start by choosing a space step $\Delta x = \dfrac{1}{M}$. M is an integer and belongs to the set $\{8, 16, 32, 64, 128\}$. Increasing values for M means a smaller space step, a finer mesh and eventually a more accurate approximation for our solution. We choose a time step $\Delta t = \dfrac{1}{M^3}$ and we iterate our scheme $\dfrac{M^3}{8}$ times. We end up with an approximation for the solutions of (3.51) at the final time $t_{max} = \dfrac{1}{8}$. Then we compare this approximation to the exact solution (3.53) by taking the L^2 norm of the difference. Figures 3.40-3.41 show the results for **A**, div **A**, ψ, γ,$\nabla \times \gamma$ and for different values of ω.

In Fig. 3.41, we see that quantities ψ, γ,$\nabla \times \gamma$ are unaffected by the change of gauge: convergence curves exhibit an order 2 (dashed line) and are nearly superimposed.

In Fig. 3.40 the vector potential shows an order 2 when $\omega = 1$ and an order 1 when $\omega = 0$. For values of ω between $\omega = 5 \times 10^{-5}$ and $\omega = 10^{-3}$ the order is greater than 2 for small size of the mesh. The divergence of **A** shows an order 1 when $\omega = 1$ and an order 0 when $\omega = 0$: it means that this quantity is not converging to the exact value when $\omega = 0$. For values of ω between $\omega = 5 \times 10^{-5}$ and $\omega = 10^{-3}$ the order is 2 for small sizes of the mesh and then it decreases; however the beginning of the decrease depends on ω.

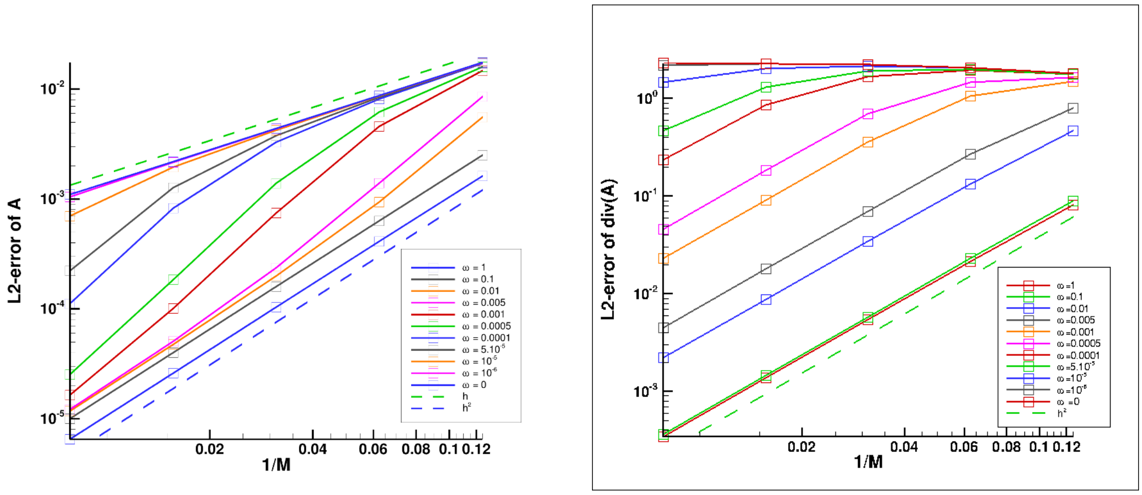

Figure 3.40. *Orders for the vector potential (left) and its divergence (right).*

These results can be recovered and extended by the Richardson extrapolation method we now introduce.

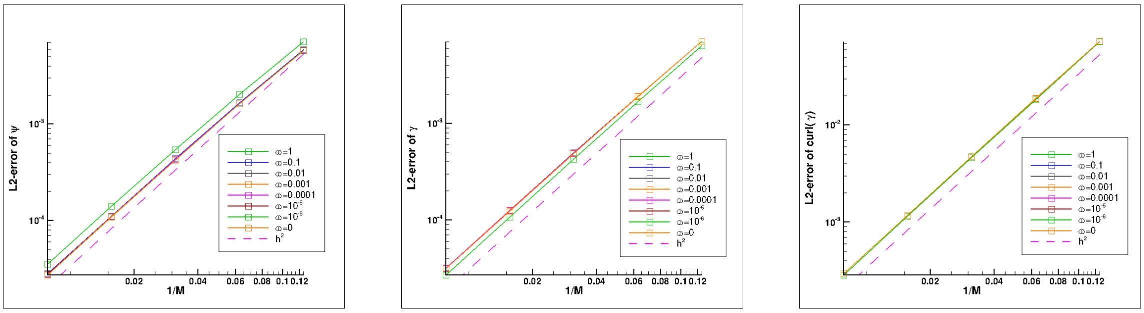

Figure 3.41. *Orders for the magnetic field ψ, γ and $\nabla \times \gamma$.*

The Richardson extrapolation method

We begin by a description of the method. Consider a quantity u to be evaluated numerically. We denote u_{ex} its exact value and u_h its approximation where h is the step to be refined. If p is the order of the numerical scheme then

$$\begin{aligned} u_{ex} &= u_h + Ch^p, \\ u_{ex} &= u_{\frac{h}{2}} + C\left(\frac{h}{2}\right)^p, \\ u_{ex} &= u_{\frac{h}{4}} + C\left(\frac{h}{4}\right)^p. \end{aligned} \tag{3.54}$$

Then by substitution we deduce

$$p = \frac{1}{\log 2} \log\left(\frac{u_{\frac{h}{2}} - u_h}{u_{\frac{h}{4}} - u_{\frac{h}{2}}}\right). \tag{3.55}$$

Since u is a field, we shall consider: $p = \dfrac{1}{\log 2} \log\left(\dfrac{||u_{\frac{h}{2}} - u_h||_{L^2}}{||u_{\frac{h}{4}} - u_{\frac{h}{2}}||_{L^2}}\right)$.

The Richardson extrapolation method is reliable once a time step is carefully chosen. In our case we choose $\Delta t = 10^{-3}$; the final time is the same as the graphical method: $t_{max} = \dfrac{1}{8} = 0.125$. As a consequence we iterate our scheme 125 times and compute the approximated solution u_h; we do the same for $u_{\frac{h}{2}}$ and $u_{\frac{h}{4}}$; eventually we compute p given by Eq. (3.55). Hereafter we denote $p \equiv o(u)$ the order for a quantity u.

Table 3.5 shows the results for the Lorentz gauge ($\omega = 1$) where $(h, \dfrac{h}{2}, \dfrac{h}{4}) = (\dfrac{1}{16}, \dfrac{1}{32}, \dfrac{1}{64})$; we retrieve the graphical results of Figs. 3.40-3.41 for $\omega = 1$.

	Err_{ψ}	$\mathrm{Err}_{\mathbf{A}}$	Err_{γ}	$\mathrm{Err}_{\mathrm{div}\,\mathbf{A}}$	$\mathrm{Err}_{\nabla\times\gamma}$
$\|\|u_{\frac{h}{2}} - u_h\|\|_{L^2}$	0.00283065	0.00149477	0.00133044	0.00704915	0.0101429
$\|\|u_{\frac{h}{4}} - u_{\frac{h}{2}}\|\|_{L^2}$	0.000709576	0.000374159	0.000332586	0.001772	0.00252371
order	1.99611	1.9982	2.0001	2.00685	1.99207

Table 3.5. *Computed L^2 norm errors of ψ, $\boldsymbol{A}$, γ, $\nabla \times \gamma$ and $\mathrm{div}\,\boldsymbol{A}$ for the Lorentz gauge.*

Table 3.6 shows the results for 10 values of ω between 0 and 1. We retrieve that the order for ψ, γ,

$\nabla \times \gamma$ is two and unaffected by the change of gauge.

For $\mathbf{A}$ and $\mathrm{div}\,\mathbf{A}$, the orders for $\omega = 0$ or $\omega = 1$ coincide again with the graphical results. In passing, we note the great accuracy of the values. For values of ω between 0 and 1, we report in Tabs. 3.7-3.8 a comparison with the graphical results. The reported graphical values are the average slope obtained with the 3 points used in the Richardson method; hence the graphical values correspond to the points of abscissa $\frac{1}{M} = (\frac{1}{16}, \frac{1}{32}, \frac{1}{64})$ in Fig. 3.40. The agreement between the two methods is very good.

Richardson method is fast and we can get a broader picture than the one we obtain from Figs. 3.40. In Fig. 3.42, we report computations of the orders for $\mathbf{A}$ and $\mathrm{div}\,\mathbf{A}$ for 30 values of ω. Four sets of values for M are shown: $M = 16, 32, 64$, $M = 32, 64, 128$, $M = 64, 128, 256$ and $M = 128, 256, 512$. We observe that given a mesh size h, there exists a value $\omega_0(h)$ in $(0, 1)$ with better convergence properties than the Lorentz gauge; in particular, when $r = 1$, we have

$$\omega_0(h) = \inf\{\omega, o(\mathbf{A}) > 2, o(\mathrm{div}\,\mathbf{A}) = 2\}. \tag{3.56}$$

Our results indicate that $o(\mathbf{A})$ is maximum at $\omega_0(h)$.

	$\omega = 1$	$\omega = 10^{-1}$	$\omega = 10^{-2}$	$\omega = 10^{-3}$	$\omega = 10^{-4}$	$\omega = 10^{-5}$	$\omega = 10^{-6}$	$\omega = 0$
Err_{ψ}	1.99594	1.99294	1.99083	1.98507	1.9919	1.99305	1.99307	1.99307
$\mathrm{Err}_{\mathbf{A}}$	1.9982	1.999	2.07292	2.55124	1.36199	1.05806	1.01602	1.0111
Err_{γ}	2.00008	1.99683	1.99408	1.98795	1.99617	1.99733	1.99735	1.99735
$\mathrm{Err}_{\nabla\times\gamma}$	2.00681	2.00412	2.00279	2.00014	2.00375	2.00425	2.00425	2.00425
$\mathrm{Err}_{\mathrm{div}\,\mathbf{A}}$	1.99169	2.00495	2.00072	1.67622	0.941629	0.116245	-0.00869583	-0.0230222

Table 3.6. *Computed orders of ψ, $\mathbf{A}$, γ, $\nabla \times \gamma$ and $\mathrm{div}\,\mathbf{A}$ for different gauges.*

	$\omega = 1$	$\omega = 10^{-1}$	$\omega = 10^{-2}$	$\omega = 10^{-3}$	$\omega = 10^{-4}$	$\omega = 10^{-5}$	$\omega = 10^{-6}$	$\omega = 0$
o($\mathbf{A}$) Richardson	1.9982	1.999	2.07292	2.55124	1.36199	1.05806	1.01602	1.0111
o($\mathbf{A}$) graphic	1.9982	1.9991	2.07829	2.41946	1.31109	1.05595	1.02201	1.01808

Table 3.7. *Comparison of the order for $\mathbf{A}$ between the Richardson method and the graphical method.*

	$\omega = 1$	$\omega = 10^{-1}$	$\omega = 10^{-2}$	$\omega = 10^{-3}$	$\omega = 10^{-4}$	$\omega = 10^{-5}$	$\omega = 10^{-6}$	$\omega = 0$
o($\mathrm{div}\,\mathbf{A}$) Richardson	1.99169	2.00495	2.00072	1.67622	0.94162	0.11624	-0.00869	-0.0230
o($\mathrm{div}\,\mathbf{A}$) graphic	1.97904	1.99031	1.95232	1.77475	0.58941	0.01583	-0.06348	-0.0643

Table 3.8. *Comparison of the order for $\mathrm{div}\,\mathbf{A}$ between the Richardson method and the graphical method.*

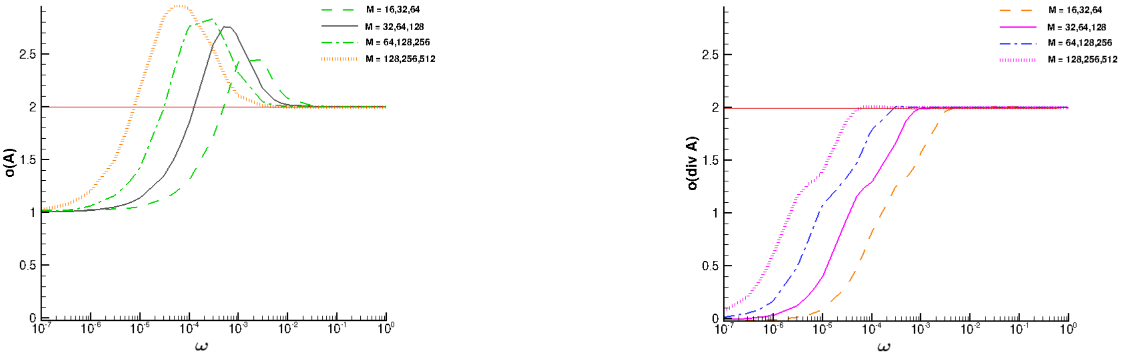

Figure 3.42. *Convergence orders for* $\boldsymbol{A}$ *(left) and* $\operatorname{div}\boldsymbol{A}$ *(right) with respect to the gauge parameter* ω.

In this chapter we have thus studied the TDGL model. The choice of the gauge is essential to define a well-posed problem and thus “to know what we compute”, as a professor told us during a conference. However it is sometimes not sufficient, since numerical issues can still happen, as we have seen in the benchmark of the disk with a boundary defect. Even when this last obstacle is overcome, we often end up with different equilibrium states (see Fig. 3.37) and one may ask which is the right one. In the case of the TDGL model, the ”right one” is a solution of the steady state GL model. The next chapter is then a natural path to explore.

4. The steady state Ginzburg-Landau model

In this chapter, we study the steady state GL model. From the historical point of view, it is interesting to notice that the steady state GL model has been introduced by Ginzburg and Landau (1950), 18 years before the TDGL model. A general physical principle states that a system tends to minimize its energy. We have seen in the previous chapter that, in the case of a superconductor of domain Ω, this energy is

$$\mathcal{G} = \mathcal{G}_0 + \int_\Omega \frac{1}{2}\left(|\psi|^2 - 1\right)^2 + \left|\left(\frac{1}{\kappa}\nabla - i\mathbf{A}\right)\psi\right|^2 + |\nabla \times \mathbf{A} - \mathbf{H}|^2 . \tag{4.1}$$

The goal of this chapter is then to minimize (4.1) and compute the minimizers $(\psi, \mathbf{A})$; hence, the constant $\mathcal{G}_0$ is of no importance and we omit it in the sequel. The outline of this chapter is as follows. In the first section, we detail mathematical results about this model: we define the concept of gauge, we study the existence of minimizers and give some of their known properties. In the second section, we present numerical results: we introduce a steepest descent algorithm using Sobolev gradients; then, we apply our algorithm to some benchmarks of the literature.

4.1. Mathematical results on the steady state GL model

4.1.1. Concept of gauge and existence of minimizers

In Du et al. (1992) we find the following definition of gauges in the steady state GL framework.

Definition 4.1.1. *For any $\phi \in H^2(\Omega)$, let the linear transformation G_ϕ from $\mathcal{H}^1(\Omega) \times \boldsymbol{H}^1(\Omega)$ into itself be defined by:*

$$G_\phi(\psi,\boldsymbol{A}) = (\zeta,\boldsymbol{Q}) := (\psi e^{i\kappa\phi},\boldsymbol{A} + \nabla\phi). \tag{4.2}$$

Two couples $(\psi, \mathbf{A})$ and $(\zeta, \mathbf{Q})$ related through (4.2) are said to be gauge equivalent.

The following proposition justifies the introduction of gauges. It states that the Gibbs free energy is invariant under the gauge transformation G_ϕ.

Proposition 4.1.2. *(Du et al., 1992)*

$$\forall\phi \in H^2(\Omega), (\psi,\boldsymbol{A}) \in \mathcal{H}^1(\Omega) \times \boldsymbol{H}^1(\Omega), \quad \mathcal{G}(\psi,\boldsymbol{A}) = \mathcal{G}(G_\phi(\psi,\boldsymbol{A})). \tag{4.3}$$

The following lemma characterises the classes of equivalence of solutions of the GL equations. It states that we can look for minimizers $(\psi, \mathbf{A})$ in the "smaller" space $\mathcal{H}^1(\Omega) \times \mathbf{H}^1_n(\mathrm{div}, \Omega)$ instead of $\mathcal{H}^1(\Omega) \times \mathbf{H}^1(\Omega)$. It is equivalent to choose the Coulomb gauge for the vector potential $\mathbf{A}$.

Lemma 4.1.3. *(Du et al., 1992) Every* $(\zeta, \boldsymbol{Q})$ *in* $\mathcal{H}^1(\Omega) \times \boldsymbol{H}^1(\Omega)$ *is gauge equivalent to an element of* $\mathcal{H}^1(\Omega) \times \boldsymbol{H}^1_n(div, \Omega)$.

The next lemma echoes the traditional $U(1)$ symmetry of the linear Schrödinger equation

Lemma 4.1.4. *(Du et al., 1992)* $(\psi, \boldsymbol{A})$ *and* $(\zeta, \boldsymbol{Q})$ *in* $\mathcal{H}^1(\Omega) \times \boldsymbol{H}^1_n(div, \Omega)$ *are gauge equivalent if and only if there exists* $c \in \mathbb{R}$ *such that* $\boldsymbol{A} = \boldsymbol{Q}$ *and* $\zeta = \psi e^{ic}$.

To introduce the existence of minimizers rigorously, we need to define what is a critical point of the GL energy (4.1). At a critical point, the derivatives of $\mathcal{G}$ are zero in every direction; mathematically, it is given by the following definition.

Definition 4.1.5. *(Sandier and Serfaty, 2008)* $(\psi, \boldsymbol{A})$ *is a critical point of GL energy (4.1) if for every smooth and compactly supported functions* $\tilde{\psi}$ *and* $\tilde{\boldsymbol{A}}$ *we have:*

$$\frac{d}{dt}\mathcal{G}(\psi + t\tilde{\psi}, \boldsymbol{A} + t\tilde{\boldsymbol{A}})|_{t=0} = 0. \tag{4.4}$$

We can show by standard calculations that a critical point of the GL energy satisfies the following set of equations and boundary conditions called *steady state GL model*:

$$\begin{aligned}
&-\left(\frac{1}{\kappa}\nabla - i\mathbf{A}\right)^2 \psi + (|\psi|^2 - 1)\psi = 0 \quad \text{in } \Omega, \\
&\nabla \times \nabla \times \mathbf{A} - \nabla \times \mathbf{H} = \frac{1}{2i}(\psi^* \nabla \psi - \psi \nabla \psi^*) - |\psi|^2 \mathbf{A} \quad \text{in } \Omega, \\
&\left(\frac{1}{\kappa}\nabla\psi - i\mathbf{A}\psi\right) \cdot \mathbf{n} = 0 \quad \text{on } \Gamma, \\
&\nabla \times \mathbf{A} \times \mathbf{n} = \mathbf{H} \times \mathbf{n} \quad \text{on } \Gamma.
\end{aligned} \tag{4.5}$$

In addition, minimizers are critical points since, when you achieve the minimum of a function, any direction you choose or its opposite, the function will increase; hence, its derivative is zero. We deduce that minimizers verify the steady state GL model (4.5).

In the previous chapter (see Eqs. (3.32)), we have already noticed that the TDGL under the temporal gauge is equivalent to a minimization of the energy (4.1). In this case, Proposition 3.38 becomes:

$$\frac{\mathrm{d}}{\mathrm{d}t}\mathcal{G}(u) = -\left|\left|\frac{\partial \psi}{\partial t}\right|\right|^2_{L^2(\Omega)} - \left|\left|\frac{\partial \mathbf{A}}{\partial t}\right|\right|^2_{L^2(\Omega)}. \tag{4.6}$$

In the steady state GL model framework, the time t is not the physical time any more; we call it *imaginary* time. We still denote this time t in the sequel.

In Du et al. (1992), existence of minimizers is proved, hence we deduce the existence of solutions for (4.5). More precisely we have the following theorem.

Theorem 4.1.6. $\mathcal{G}$ *has at least one minimizer belonging to* $\mathcal{H}^1(\Omega) \times \boldsymbol{H}^1(\Omega)$. *Moreover*

$$\min_{\mathcal{H}^1(\Omega)\times\boldsymbol{H}^1(\Omega)} \mathcal{G} = \min_{\mathcal{H}^1(\Omega)\times\boldsymbol{H}^1_n(\Omega)} \mathcal{G} = \min_{\mathcal{H}^1(\Omega)\times\boldsymbol{H}^1_n(div,\Omega)} \mathcal{G}. \tag{4.7}$$

In the next section we detail some known results about minimizers.

4.1.2. Properties of solutions of the steady state GL model (4.5)

The earliest description of the solutions for a superconductor of type II has been made by Abrikosov (1957). He showed that, for $\kappa > \dfrac{1}{\sqrt{2}}$, a periodic solution for the order parameter ψ exists: it is called *flux-line lattice*. Later, it has been shown by Kleiner et al. (1964) that the triangular lattice is the state of lowest energy near H_{c2}. These results are valid only when the domain Ω is unbounded. For bounded domains, regular polygons, regular stars have been observed experimentally when the number of vortices is such that $n \leq 8$; beyond this threshold, vortices appear to arrange in concentric circles (Grigorieva et al., 2006).

4.1.3. Basic solutions

When the domain Ω is unbounded, there exists two "simple" solutions of equations $(4.5)_{1,2}$: the pure superconducting state S and the normal state N.

- in state S, $\psi = 1$ (all electrons are superconducting) and $\mathbf{A} = \mathbf{0}$ (no magnetic field penetrate the domain). Replacing ψ and $\mathbf{A}$ in (4.1) we obtain

  $$\mathcal{G} = \int_\Omega H^2 = |\Omega| H^2, \tag{4.8}$$

  where $|\Omega|$ is the area (or volume) of the domain.
- in state N, $\psi = 0$ (all the electrons are normal) and $\nabla \times \mathbf{A} = \mathbf{H}$ (the field inside the domain is equal to the applied field). In this case we have

  $$\mathcal{G} = \int_\Omega H^2 = \frac{1}{2}|\Omega|. \tag{4.9}$$

From (4.8)-(4.9) we deduce the critical value for the applied field $H_c = \dfrac{1}{\sqrt{2}}$; this is the critical field for type I superconductor. But as we have seen in the introduction, type II superconductors have two critical values for the applied magnetic field, H_{c1} and H_{c2}; in between, the superconductor is in the mixed state. A rigorous mathematical description of the mixed state is a difficult task; this work has been pioneered by Bethuel et al. (1994) and continued by many authors. A detailed exposition of the results can be found in Sandier and Serfaty (2008). In the next section, we present two of these results.

4.1.4. Two theorems towards Abrikosov mixed state

In this section our goal is to present the ideas behind two results. We do not want to be technical and refer the interested reader to Sandier and Serfaty (2008).

For convenience, we start by rescaling energy (4.1). If we make the additional change of variables $\mathbf{A}' = \kappa \mathbf{A}$, $\mathbf{H}' = \kappa \mathbf{H}$, $\mathcal{G}' = \dfrac{\kappa^2}{2}\mathcal{G}$ and omitting primes, we find the following Gibbs energy (Neuberger, 2009):

$$\mathcal{G} = \int_{\Omega} \frac{\kappa^2}{4}\left(|\psi|^2 - 1\right)^2 + \frac{1}{2}\left|\left(\nabla - i\mathbf{A}\right)\psi\right|^2 + \frac{1}{2}\left|\nabla \times \mathbf{A} - \mathbf{H}\right|^2. \tag{4.10}$$

Since we intend to consider large values for κ, we set $\epsilon = \frac{1}{\kappa}$. Moreover, we denote $\nabla_A = \nabla - i\mathbf{A}$ so that (4.10) becomes:

$$\mathcal{G}_\epsilon := \frac{1}{2}\int_{\Omega} |\nabla_A \psi|^2 + |\nabla \times \mathbf{A} - \mathbf{H}|^2 + \frac{1}{2\epsilon^2}\left(|\psi|^2 - 1\right)^2. \tag{4.11}$$

When $\mathbf{H} = 0$ we denote:

$$\mathcal{F}_\epsilon := \frac{1}{2}\int_{\Omega} |\nabla_A \psi|^2 + |\nabla \times \mathbf{A}|^2 + \frac{1}{2\epsilon^2}\left(|\psi|^2 - 1\right)^2. \tag{4.12}$$

The first theorem is due to Sandier (1998) and establishes a lower bound on $\mathcal{F}_\epsilon$. Suppose a superconductor is in a mixed state with N vortices around which supercurrents rotate in the same sense; you can think of Fig. 3.15 but with N possibly very large and vortices densely packed. The theorem says that you can cover the areas where the amplitude $|\psi|$ is below a given threshold (in particular areas where there are vortices) by a family of disjoint disks if we are in 2D. Denoting r the sum of the radii of the disks, then the following inequality holds:

$$\mathcal{F}_\epsilon \geq \pi N \left(\log\left(\frac{r}{N\epsilon}\right) - C\right), \tag{4.13}$$

where C is a universal constant. The term $\pi N \log\left(\frac{r}{N\epsilon}\right)$ can be seen as N times the energy of a single vortex which is $\pi \log\left(\frac{r}{N\epsilon}\right)$. The energy of a single vortex line $E_{1\text{ vortex}}$ is known: in de Gennes (1966) for example we find the expression

$$E_{1\text{ vortex}} = \left(\frac{\phi_0}{\sqrt{4\pi\mu_0}\lambda}\right)^2 \log\kappa. \tag{4.14}$$

After a suitable scaling, we have $E_{1\text{ vortex}} = \pi\log\kappa$, to be compared to $\pi\log\left(\frac{r}{N}\kappa\right)$ given by Theorem 4.13 for a large number of vortices.

The second theorem characterizes the limit of the energy $\mathcal{G}_\epsilon$ when $\epsilon \to 0$ and $\frac{H}{\log\epsilon} \to \lambda > 0$, i.e. for large values of κ and suitable large applied magnetic field. We do not state the convergence result mathematically since it would lead us too far but rather give a physical interpretation. It states that if H is sufficiently large, then there is a *blow-up* of the number of vortices, and they are uniformly distributed. This justifies rigorously the existence of the first critical field H_{c1} in an asymptotic sense.

The density of the vortex distribution is described mathematically by a measure denoted by μ^*, and we have that μ^* is proportional to the Lebesgue measure:

$$\mu^* = \left(1 - \frac{1}{2\lambda}\right)\mathbb{1}_{\omega_\lambda}\mathrm{d}x, \tag{4.15}$$

where ω_λ is a compact set.

The limiting magnetic field h_{μ^*} is also characterized as the unique minimizer of an obstacle problem:

$$\min_{\substack{h-1\in \mathrm{H}_0^1(\Omega) \\ h\geq 1-\frac{1}{2\lambda}}} \frac{1}{2}\int_\Omega |\nabla h|^2 + |h|^2. \tag{4.16}$$

An interesting consequence of (4.16) is that h_{μ^*} is constant on ω_λ.

4.2. Numerical results

The goal of this section is to find the vortex pattern in the equilibrium state. Since we are interested in equilibrium patterns, we choose an algorithm known for its fast convergence: the steepest descent method with Sobolev gradients (Neuberger and Renka, 1998; Neuberger, 2009; Danaila and Kazemi, 2010; Kazemi and Renka, 2013).

In the first part, we recall the essential features of Sobolev gradients and describe the algorithm. In the second part, we show some numerical examples on various geometries.

4.2.1. The steepest descent algorithm using Sobolev gradient method

We begin by recalling the definition of the Fréchet derivative of a functional with real values since we use this concept several times in the manuscript.

Definition 4.2.1. *Let H a Hilbert space and $\Omega \subset H$ an open subset. A functional $\mathcal{G} : \Omega \to \mathbb{R}_+$ is Fréchet differentiable at u in Ω if it exits a continuous and linear functional denoted by $d_u\mathcal{G} : H \to \mathbb{R}$ such that*

$$\mathcal{G}(u+h) = \mathcal{G}(u) + d\mathcal{G}_u(h) + ||h||_H \epsilon(h), \tag{4.17}$$

and $\epsilon(h) \to 0$ when $h \to 0$.

In what follows, we consider partial derivatives of Fréchet type. We state the following definition.

Definition 4.2.2. *Let H_1 and H_2 two Hilbert spaces and $\Omega_1 \times \Omega_2 \subset H_1 \times H_2$ an open subset. A functional $\mathcal{G} : \Omega_1 \times \Omega_2 \to \mathbb{R}_+$ is Fréchet differentiable at $u = (u_1, u_2)$ in the direction of u_1 if it exits a continuous and linear functional denoted by $\partial_{u_1}\mathcal{G} : H_1 \to \mathbb{R}$ such that*

$$\mathcal{G}(u_1 + h, u_2) = \mathcal{G}(u) + \partial_{u_1}\mathcal{G}(h) + ||h||_{H_1}\epsilon(h), \tag{4.18}$$

and $\epsilon(h) \to 0$ when $h \to 0$.

Fréchet derivative of the Gibbs energy with respect to ψ

In view of definition (4.2.2) the Fréchet derivative of (4.1) with respect to ψ is:

$$\partial_\psi \mathcal{G}(\tilde{\psi}) = 2\Re\left(\int_\Omega \left(\frac{1}{\kappa}\nabla\psi - i\mathbf{A}\psi\right)\cdot\left(\frac{1}{\kappa}\nabla\tilde{\psi}^* - i\mathbf{A}\tilde{\psi}^*\right) + \int_\Omega \left(|\psi|^2 - 1\right)\psi\tilde{\psi}\right). \tag{4.19}$$

If we do an integration by parts on the first term of the right hand side, and suppose that ψ verifies the boundary conditions (4.5)$_3$, we deduce:

$$\partial_\psi \mathcal{G}(\tilde{\psi}) = 2\Re\left(\int_\Omega -\left(\frac{1}{\kappa}\nabla - i\mathbf{A}\right)^2 \psi\tilde{\psi} + \int_\Omega \left(|\psi|^2 - 1\right)\psi\tilde{\psi}\right). \tag{4.20}$$

Then

$$\partial_\psi \mathcal{G}(\tilde{\psi}) = 2\Re\left(\nabla^\psi_{L^2}\mathcal{G}, \tilde{\psi}\right)_{L^2}, \tag{4.21}$$

where $(u,v)_{L^2} = \displaystyle\int_\Omega uv^*$ is the usual scalar product on L^2 and where we called L^2-gradient of $\mathcal{G}$ with respect to ψ:

$$\nabla^\psi_{L^2}\mathcal{G} = -\left(\frac{1}{\kappa}\nabla - i\mathbf{A}\right)^2 \psi + \left(|\psi|^2 - 1\right)\psi. \tag{4.22}$$

The descent equation for ψ can be written (see also (3.32)):

$$\frac{\partial\psi}{\partial t} = -\nabla^\psi_{L^2}\mathcal{G}. \tag{4.23}$$

Fréchet derivative of the Gibbs energy with respect to A

In view of definition (4.2.2) the Fréchet derivative of (4.1) with respect to $\mathbf{A}$ is

$$\partial_\mathbf{A}\mathcal{G}(\tilde{\mathbf{A}}) = 2\Re\left(\int_\Omega i\psi^*\left(\frac{1}{\kappa}\nabla\psi - i\mathbf{A}\psi\right)\cdot\tilde{\mathbf{A}}\right) + 2\int_\Omega (\nabla\times\mathbf{A} - \mathbf{H})\cdot\nabla\times\tilde{\mathbf{A}}. \tag{4.24}$$

By noting that $\Re(iz) = -\Im(z) = -\frac{1}{2i}(z+\bar{z})$ and doing an integration by parts on the second term of the right hand side, with $\mathbf{A}$ verifying boundary condition (4.5)$_4$, we obtain:

$$\partial_\mathbf{A}\mathcal{G}(\tilde{\mathbf{A}}) = 2\int_\Omega \left[-\frac{1}{2i\kappa}\left(\psi^*\nabla\psi - \psi\nabla\psi^*\right) + \mathbf{A}|\psi|^2\right]\cdot\tilde{\mathbf{A}} + 2\int_\Omega \nabla\times(\nabla\times\mathbf{A} - \mathbf{H})\cdot\tilde{\mathbf{A}}. \tag{4.25}$$

We can rewrite (4.25):

$$\partial_\mathbf{A}\mathcal{G}(\tilde{\mathbf{A}}) = 2\left(\nabla^\mathbf{A}_{L^2}\mathcal{G}, \tilde{\mathbf{A}}\right)_{L^2}, \tag{4.26}$$

where $(X,Y)_{L^2} = \displaystyle\int_\Omega X\cdot Y$ is the usual scalar product on $\mathbf{L}^2$ and where we called L^2-gradient of $\mathcal{G}$ with respect to $\mathbf{A}$:

$$\nabla^\mathbf{A}_{L^2}\mathcal{G} = -\frac{1}{2i\kappa}\left(\psi^*\nabla\psi - \psi\nabla\psi^*\right) + \mathbf{A}|\psi|^2 + \nabla\times(\nabla\times\mathbf{A} - \mathbf{H}). \tag{4.27}$$

The descent equation for $\mathbf{A}$ can be written (see also (3.32)):

$$\frac{\partial\mathbf{A}}{\partial t} = -\nabla^\mathbf{A}_{L^2}\mathcal{G}. \tag{4.28}$$

Sobolev gradients

Equations (4.23) and (4.28) are used to find the state of minimum energy. The minus sign on the right hand sides of (4.23) and (4.28) means that we follow the direction opposite to the gradient of the energy: it is called the *gradient flow* technique. Doing this, we are indeed minimizing energy (4.1), since we recall that (Hoffmann and Tang, 2001; Du, 1994b):

$$\frac{\mathrm{d}}{\mathrm{d}t}\mathcal{G}(u) = -\left|\left|\frac{\partial \psi}{\partial t}\right|\right|^2_{L^2(\Omega)} - \left|\left|\frac{\partial \mathbf{A}}{\partial t}\right|\right|^2_{L^2(\Omega)}. \tag{4.29}$$

To explain Sobolev gradients, we recall a powerful theorem of functional analysis called the *Riesz representation theorem.*

Theorem 4.2.3. *Any continous linear functional f on a Hilbert space H can be represented by a vector f_H in the sense that*

$$f(x) = (f_H, x)_H \quad \forall x \in H, \tag{4.30}$$

where $(\cdot,\cdot)$ denotes the scalar product on H.

Now, if we denote H_ψ and $H_\mathbf{A}$ two Hilbert spaces (that we will define later), (4.30) shows the existence of two vectors denoted by $\nabla^\psi_S\mathcal{G}$ and $\nabla^\mathbf{A}_S\mathcal{G}$ such that

$$\begin{aligned}\left(\nabla^\psi_{L^2}\mathcal{G}, \tilde{\psi}\right)_{L^2} &= \left(\nabla^\psi_S\mathcal{G}, \tilde{\psi}\right)_{H_\psi},\\ \left(\nabla^\mathbf{A}_{L^2}\mathcal{G}, \tilde{\mathbf{A}}\right)_{L^2} &= \left(\nabla^\mathbf{A}_S\mathcal{G}, \tilde{\mathbf{A}}\right)_{H_\mathbf{A}}.\end{aligned} \tag{4.31}$$

We interpret (4.31) saying that we can follow a gradient descent called *Sobolev gradient* in H_ψ (or $H_\mathbf{A}$), instead of L^2. If we choose wisely these Hilbert spaces the convergence towards the state of minimum energy can be faster. In what follows, we detail the spaces H_ψ and $H_\mathbf{A}$ and the descent algorithm.

The descent algorithm

A first choice for H_ψ is to choose $H_\psi := \mathcal{H}_1$. In that case solving Eq. $(4.31)_1$ amounts to find a function χ such that

$$\int_\Omega \chi\tilde{\psi} + \int_\Omega \nabla\chi\cdot\nabla\tilde{\psi} = \left(\nabla^\psi_{L^2}\mathcal{G}, \tilde{\psi}\right)_{L^2}. \tag{4.32}$$

Another choice has been proposed by Danaila and Kazemi (2010). The authors set:

$$H_\psi := \{\psi \in L^2(\Omega), \int_\Omega |\nabla_A\psi|^2 < \infty\}, \tag{4.33}$$

where we denote $\nabla_A := \frac{1}{\kappa}\nabla - i\mathbf{A}$. H_ψ is equipped with the scalar product $(u,v)_H = \int_\Omega uv^* + \int_\Omega \nabla_A u\cdot(\nabla_A v)^*$. Solving Eq. $(4.31)_1$ amounts to find a function χ such that

$$\int_\Omega \chi\tilde{\psi} + \int_\Omega \nabla_A\chi\cdot\nabla_A\tilde{\psi} = \left(\nabla^\psi_{L^2}\mathcal{G}, \tilde{\psi}\right)_{L^2}. \tag{4.34}$$

For the vector potential, a possible choice can be $H_{\mathbf{A}} := \mathbf{H}^1$, but in view of (4.1.6), we choose $H_{\mathbf{A}} := \mathbf{H}^1_n$. For simplicity, we do not impose div $\mathbf{A} = 0$. Then solving Eq. (4.31)$_2$ amounts to find a function $\mathbf{B}$ such that

$$\int_\Omega \mathbf{B} \cdot \tilde{\mathbf{A}} + \int_\Omega \nabla \mathbf{B} : \nabla \tilde{\mathbf{A}} = \left(\nabla^{\mathbf{A}}_{L^2} \mathcal{G}, \tilde{\mathbf{A}} \right)_{L^2}. \tag{4.35}$$

The Sobolev gradients are found by solving (4.32) or (4.34) and (4.35). We use linear Lagrange FEs P^1. Then the solution is advanced following the general descent method:

$$\begin{pmatrix} \psi_{n+1} \\ \mathbf{A}_{n+1} \end{pmatrix} = \begin{pmatrix} \psi_n \\ \mathbf{A}_n \end{pmatrix} - \delta t \begin{pmatrix} \nabla^{\psi}_{S} \mathcal{G}(u_n, \mathbf{A}_n) \\ \nabla^{\mathbf{A}}_{S} \mathcal{G}(u_n, \mathbf{A}_n) \end{pmatrix}. \tag{4.36}$$

4.2.2. Results in 2D

In this section we study three benchmarks of the literature. The first example is taken from Kazemi (2008); the second one is a well-known benchmark (Gropp et al., 1996; Richardson et al., 2004); the third one has been proposed by Alstrom et al. (2011) and has been studied by many authors since then (Gao and Sun, 2015; Li and Zhang, 2015; Gao, 2017). In all examples, the pure superconducting state is taken as initial state ($\psi_0 = 1$ and $\mathbf{A}_0 = \mathbf{0}$). Then we compute iterates $(\psi_n, \mathbf{A}_n)$ using Algorithm 4.36. Table 4.1 summarizes the parameters of each simulation and the choice for the Hilbert space H_ψ. M refers to the number of nodes per unit length of the mesh. We also report the energy at final time $\mathcal{G}_{t_{max}}$.

	H_ψ	M	Δt	κ	$\mathbf{H}$	t_{max}	$\mathcal{G}_{t_{max}}$
Example 1	$\mathcal{H}^1$	40	0.1	4	1.5	2000	7.0186
Example 1	H_{∇_A}	40	0.1	4	1.5	2000	6.9494
Example 2	$\mathcal{H}^1$	20	0.1	2	0.95	4000	46.7124
Example 2	H_{∇_A}	20	0.1	2	0.95	2000	51.2324
Example 3	H_{∇_A}	20	0.1	4	0.9	2000	17.1803

Table 4.1. *Parameters, Hilbert space H_ψ and energy of the final state in Examples 1-3*

- *Example 1*: we consider the square $\left[-\frac{5}{2}, \frac{5}{2}\right]$. We set $\kappa = 4$ and $H = 1.5$. We use a uniform mesh with $M = 40$. Figures 4.1-4.3 show the results.

  For the case $H_\psi = \mathcal{H}^1$ the vortex pattern (Fig. 4.1 left) is similar to the one obtained by Kazemi (2008). Relative energy differences (Fig. 4.2 left) indicate that the state is converged.

  For the case $H_\psi = H_{\nabla_A}$, the vortex pattern (Fig. 4.1 right) appear to be of lower energy (see Tab. 4.1). In addition we notice two successive rearrangements of vortices: they corresponds to rises of relative energy differences (see Fig. 4.2 right).

  The TDGL results are shown in Fig. 4.3. The vortex pattern is similar to the case $H_\psi = H_{\nabla_A}$, with almost the same final energy $\mathcal{G}_{t_{max}} = 6.9476$. Moreover, from the relative energy differences curve, the convergence appear to be faster; however our computation for the TDGL uses a mixed scheme that require 528527 degrees of freedom to compute $\mathbf{A}$ whereas the Sobolev gradient method use a Lagrange scheme that requires 77440 degrees of freedom for $\mathbf{A}$. As a consequence, Sobolev gradient methods are much less resource consuming.

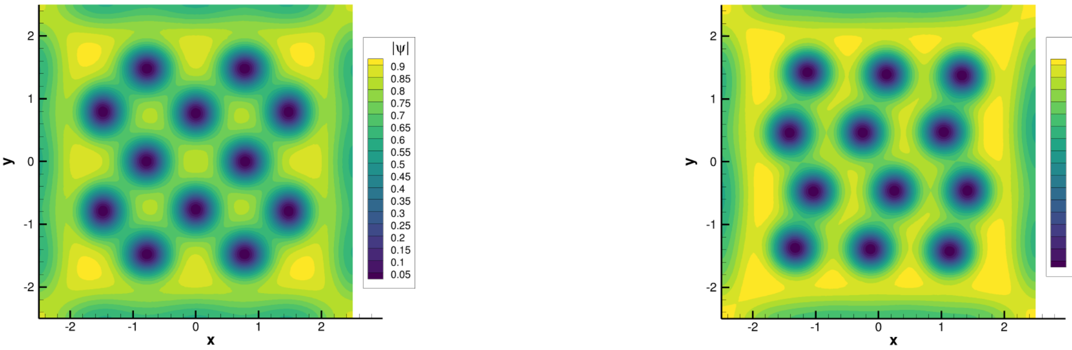

Figure 4.1. *Example 1. Density* $|\psi|$ *at* $t = 2000$ *with* $H_\psi = \mathcal{H}^1$ *(left) and* $H_\psi = H_{\nabla_A}$ *(right).*

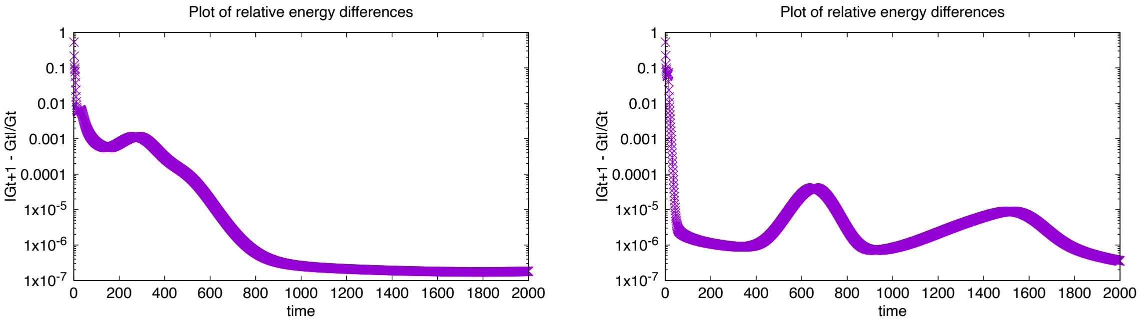

Figure 4.2. *Example 1. Relative energy differences corresponding to* $H_\psi = \mathcal{H}^1$ *(left) and* $H_\psi = H_{\nabla_A}$ *(right).*

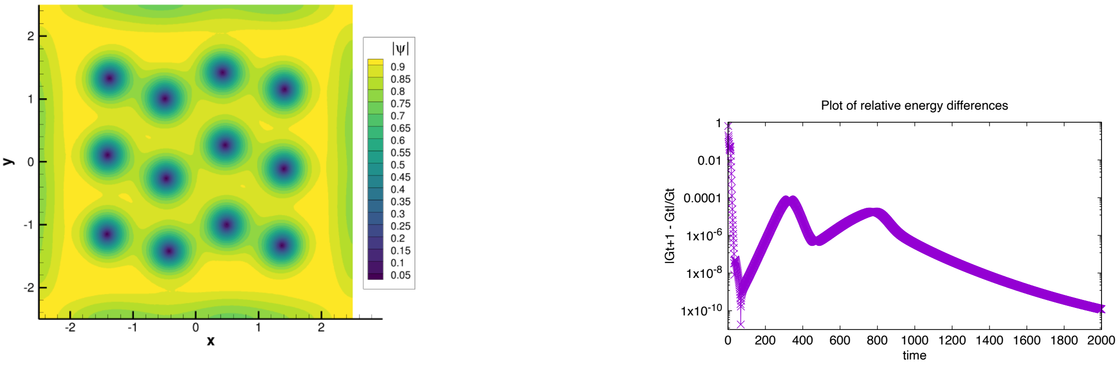

Figure 4.3. *Example 1. TDGL results at* $t = 2000$. *Density* ψ *(left) and relative energy differences (right).*

- *Example 2*: we consider the square $[-6, 6]$. We set $\kappa = 2$ and $H = 0.95$. We use a uniform mesh with $M = 20$. Figures 4.4-4.5 show the results. In Fig. 4.4 we observe two very different outcomes.

  For $H_\psi = \mathcal{H}^1$ we observe 24 vortices that may appear randomly organised; but if we look carefully, the pattern is composed by 4 chains of 6 vortices each.

  For $H_\psi = H_{\nabla_A}$ we recover the TDGL result (see Fig. 3.10). What is surprising is that the energy $\mathcal{G}_{t_{max}}$ in Tab. 4.1 is much larger. This is rather unexpected since from our experience the choice $H_\psi = H_{\nabla_A}$ usually gives the best result.

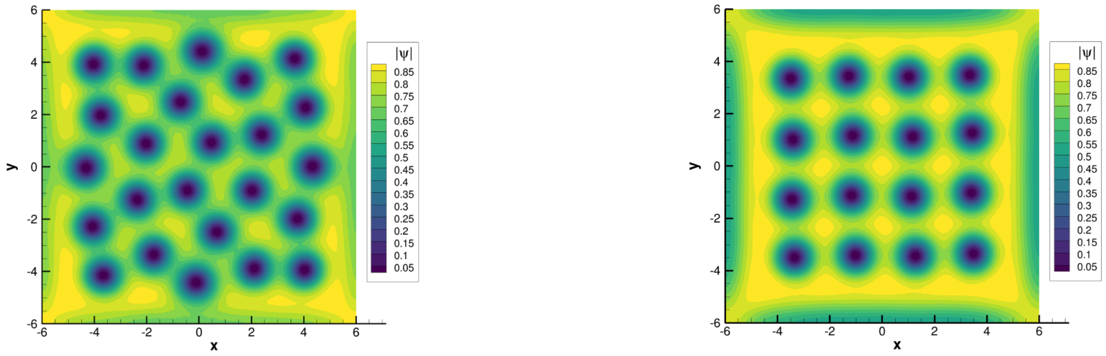

Figure 4.4. *Example 2. Density $|\psi|$ with $H_\psi = \mathcal{H}^1$ (left) and $H_\psi = H_{\nabla_A}$ at $t = 2000$ (right).*

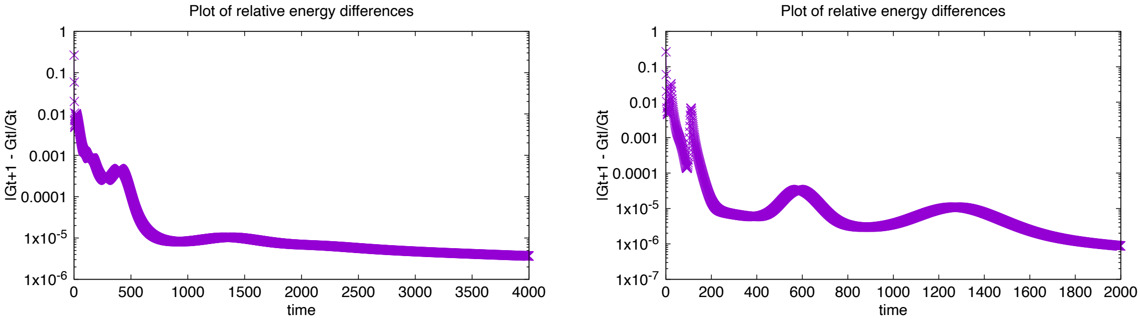

Figure 4.5. *Example 2. Relative energy differences corresponding to $H_\psi = \mathcal{H}^1$ (left) and $H_\psi = H_{\nabla_A}$ (right).*

- *Example 3*: we consider a disk with a boundary defect (3.13). We set $\kappa = 4$ and $H = 0.9$. We use a uniform mesh with $M = 20$. Fig. 4.6 shows the results. We observed 21 vortices arranged in concentric circles. This pattern is close to the TDGL results in the Lorentz gauge (see Fig. 3.36).

  We note that the choice $H_\psi = \mathcal{H}^1$ leads to a pattern with large normal zones for the same parameters. As we have already seen in Section 3.7.1, this indicates bad convergence properties of the scheme. We emphasize that, in this example, the boundary condition $\mathbf{A} \cdot \mathbf{n} = 0$ is not imposed due to the use of Lagrange finite elements (see Remark 3.5.1). This may explain the encountered difficulties.

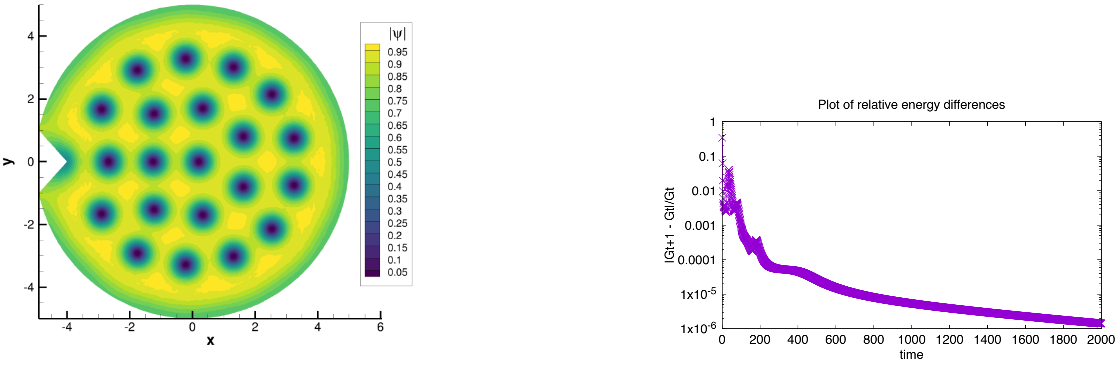

Figure 4.6. *Example 3. Density $|\psi|$ with $H_\psi = H_{\nabla_A}$ at $t = 2000$ (left) and energy relative differences (right).*

During our investigations on this example, we have discovered original equilibrium states of lower energy than the ones already presented. We know that the TDGL is equivalent (via a gauge transformation) to a descent method in L^2 (see Eqs. (3.32)). As a consequence the final result, if correct, is a minimizer of the Gibbs free energy (4.1) and therefore a solution to the steady state GL model. This has been shown rigorously by Fleckinger-Pellé et al. (1997). However numerics only capture critical points of the Gibbs free energy (i.e. solutions of $\nabla \mathcal{G} = 0$), that are usually not the state of lowest energy. To find it, we can apply a perturbation of the numerical result (e.g. a change in the mesh, a perturbation of the solution or a change of the initial conditions). Two new configurations are shown in Fig. 4.7. On the left, the pattern contains 23 vortices and the Gibbs energy value is 15.7694; on the right, the pattern contains 24 vortices and its energy is 15.5547. The latter does not have a symmetry with respect to the x-axis. Moreover, we observe a similar structure with the minimizer of the following energy w_n for $n = 24$ introduced by Sandier and Serfaty (2008) and computed in Gueron and Shafrir (1999): under the constraint $\displaystyle\sum_{i=1}^{n} |x_i|^2 = 1$,

$$w_n(x_1, \ldots, x_n) = -\pi \sum_{i \neq j} \log|x_i - x_j| + C\pi n \sum_{i=1}^{n} |x_i|^2. \tag{4.37}$$

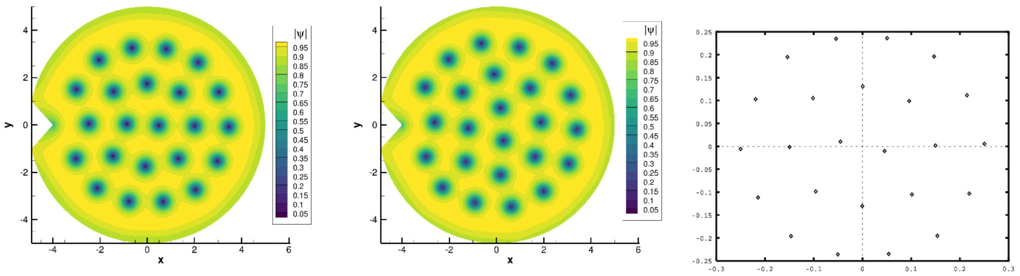

Figure 4.7. *The two configurations of lowest energy with 23 and 24 vortices (left and middle). Minimizer of w_{24} (Gueron and Shafrir, 1999) (right).*

5. An Abelian-Higgs model

In Nielsen and Olesen (1973), it is shown that vortex line solutions can be obtained from a Higgs type of Lagrangian. The Higgs model can also be considered as a relativistic generalisation of the GL phenomenological theory of type II superconductors.

5.1. Definition

The Higgs Lagrangian in SI units, as written in Nielsen and Olesen (1973) is:

$$\mathcal{L} = -\frac{1}{4\mu_0}F_{\mu\nu}F^{\mu\nu} + \frac{1}{2m_s}|(-i\hbar\partial_\mu + e_s A_\mu)\psi|^2 - \alpha|\psi|^2 - \frac{\beta}{2}|\psi|^4, \tag{5.1}$$

where α and β are the usual temperature dependent GL parameters, with $\alpha < 0$; m_s and e_s are the mass and charge of the superconducting particle respectively.

Notation $F_{\mu\nu}F^{\mu\nu}$ follows the Einstein's convention of summation over repeated index

$$F_{\mu\nu}F^{\mu\nu} = \sum_{\mu,\nu\in\{t,x,y,z\}} F_{\mu\nu}F^{\mu\nu}. \tag{5.2}$$

$F_{\mu\nu}$ and $F^{\mu\nu}$ are called *covariant* and *contravariant* tensors of the electromagnetic field:

$$F_{\mu\nu} = \begin{pmatrix} 0 & \frac{E_x}{c} & \frac{E_y}{c} & \frac{E_z}{c} \\ -\frac{E_x}{c} & 0 & -B_z & B_y \\ -\frac{E_y}{c} & B_z & 0 & -B_x \\ -\frac{E_z}{c} & -B_y & B_x & 0 \end{pmatrix}, \quad F^{\mu\nu} = \begin{pmatrix} 0 & -\frac{E_x}{c} & -\frac{E_y}{c} & -\frac{E_z}{c} \\ \frac{E_x}{c} & 0 & -B_z & B_y \\ \frac{E_y}{c} & B_z & 0 & -B_x \\ \frac{E_z}{c} & -B_y & B_x & 0 \end{pmatrix}. \tag{5.3}$$

The second term in (5.1) is computed following the rule for a vector field X_μ of components (X_t, X_x, X_y, X_z):

$$\begin{aligned} |X_\mu|^2 = X_\mu \bar{X}^\mu &= X_t\bar{X}^t + X_x\bar{X}^x + X_y\bar{X}^y + X_z\bar{X}^z \\ &= |X_t|^2 - |\mathbf{X}|^2. \end{aligned} \tag{5.4}$$

Using rules (5.2), (5.4) and the following classical definitions of the 4-vector potential and 4-derivatives:

$$\begin{cases} A_\mu = (\frac{V}{c}, -\mathbf{A}), & A^\mu = (\frac{V}{c}, \mathbf{A}), \\ \partial_\mu = (\frac{1}{c}\frac{\partial}{\partial t}, \nabla), & \partial^\mu = (\frac{1}{c}\frac{\partial}{\partial t}, -\nabla), \end{cases} \tag{5.5}$$

Lagrangian (5.1) can be rewritten as:

$$\mathcal{L} = \frac{1}{2\mu_0}\left(\frac{E^2}{c^2} - B^2\right) + \frac{1}{2m_s c^2}\left|\left(-i\hbar\frac{\partial}{\partial t} + e_s V\right)\psi\right|^2 - \frac{1}{2m_s}\left|\left(i\hbar\nabla + e_s\mathbf{A}\right)\psi\right|^2 - \alpha|\psi|^2 - \frac{\beta}{2}|\psi|^4. \tag{5.6}$$

5.2. Scaling

In this section we derive a dimensionless form of the Lagrangian (5.6). We introduce the following non-dimensional quantities:

$$\begin{aligned} &\mathbf{x}' = \frac{\mathbf{x}}{x_0}, \quad t' = \frac{t}{t_0}, \quad \psi' = \frac{\psi}{\psi_0}, \\ &\mathbf{A}' = \frac{\mathbf{A}}{A_0}, \quad V' = \frac{V}{V_0}. \end{aligned} \tag{5.7}$$

Substituting in (5.6) and omitting primes we obtain:

$$\begin{aligned} \mathcal{L} = {} & \frac{A_0^2}{2\mu_0 x_0^2}\left(\frac{x_0^2}{c^2 t_0^2}\left(\frac{\partial \mathbf{A}}{\partial t} + \frac{V_0 t_0}{A_0 x_0}\nabla V\right)^2 - |\nabla\times\mathbf{A}|^2\right) \\ & -\alpha\psi_0^2\left[-\frac{\hbar^2}{2mc^2\alpha t_0^2}\left|\left(-i\frac{\partial}{\partial t} + \frac{qV_0 t_0}{\hbar}V\right)\psi\right|^2\right. \\ & \left. + \frac{\hbar^2}{2m\alpha x_0^2}\left|\left(-i\nabla - \frac{qA_0}{\hbar}\mathbf{A}\right)\psi\right|^2 + |\psi|^2 + \frac{\beta}{2\alpha}|\psi|^4\right]. \end{aligned} \tag{5.8}$$

We make the following choices:

$$x_0 = ct_0, \quad \frac{V_0 t_0}{A_0 x_0} = 1, \quad \psi_0^2 = \frac{-\alpha}{\beta}, \quad -\alpha\psi_0^2 = \frac{A_0^2}{2\mu_0 x_0^2}. \tag{5.9}$$

We obtain:

$$\begin{aligned} \mathcal{L} = {} & \frac{\alpha^2}{\beta}\left(\left(\frac{\partial \mathbf{A}}{\partial t} + \nabla V\right)^2 - |\nabla\times\mathbf{A}|^2\right) \\ & + \frac{\alpha^2}{\beta}\left[-\frac{\hbar^2}{2m_s\alpha x_0^2}\left|\left(-i\frac{\partial}{\partial t} + \frac{e_s}{\hbar}x_0^2\sqrt{\frac{2\mu_0\alpha^2}{\beta}}V\right)\psi\right|^2\right. \\ & \left. + \frac{\hbar^2}{2m_s\alpha x_0^2}\left|\left(-i\nabla - \frac{e_s}{\hbar}x_0^2\sqrt{\frac{2\mu_0\alpha^2}{\beta}}\mathbf{A}\right)\psi\right|^2 + |\psi|^2 - \frac{1}{2}|\psi|^4\right]. \end{aligned} \tag{5.10}$$

Introducing the London length $\lambda = \sqrt{\dfrac{m_s\beta}{-e_s^2\mu_0\alpha}}$ and the coherence length $\xi = \dfrac{\hbar}{\sqrt{-2m_s\alpha}}$, we obtain:

$$\begin{aligned}\mathcal{L} = \frac{\alpha^2}{\beta}&\left(\left(\frac{\partial \mathbf{A}}{\partial t} + \nabla V\right)^2 - |\nabla \times \mathbf{A}|^2\right)\\ +\frac{\alpha^2}{\beta}&\left[\frac{\xi^2}{x_0^2}\left|\left(-i\frac{\partial}{\partial t} + \frac{x_0^2}{\xi\lambda}V\right)\psi\right|^2\right.\\ &\left.-\frac{\xi^2}{x_0^2}\left|\left(-i\nabla - \frac{x_0^2}{\xi\lambda}\mathbf{A}\right)\psi\right|^2 + |\psi|^2 - \frac{1}{2}|\psi|^4\right].\end{aligned} \tag{5.11}$$

We can choose $x_0 = \lambda$ as the unit of length, and rescale the energy density $\mathcal{L}$ in units of $\dfrac{\alpha^2}{\beta}$. Denoting as usually $\kappa = \dfrac{\lambda}{\xi}$, we obtain the final expression of the dimensionless Lagrangian:

$$\mathcal{L} = \left(\frac{\partial \mathbf{A}}{\partial t} + \nabla V\right)^2 - |\nabla \times \mathbf{A}|^2 + \left|\left(-\frac{i}{\kappa}\frac{\partial}{\partial t} + V\right)\psi\right|^2 - \left|\left(-\frac{i}{\kappa}\nabla - \mathbf{A}\right)\psi\right|^2 + |\psi|^2 - \frac{1}{2}|\psi|^4. \tag{5.12}$$

5.3. Equations of motion

To obtain the equation of motion from the Lagrangian (5.12), we use the least action principle. It states that the *action* of the system defined by

$$S = \int \mathcal{L}(\mathbf{A}, \frac{\partial \mathbf{A}}{\partial x^i}, \psi, \frac{\partial \psi}{\partial x^i})\mathrm{d}\Omega, \tag{5.13}$$

where $\mathrm{d}\Omega = \mathrm{d}t\mathrm{d}x\mathrm{d}y\mathrm{d}z$, is extremal. Hence, its derivatives with respect to ψ and $\mathbf{A}$ are equal to zero.

5.3.1. Equation of motion for the order parameter ψ

We take the Fréchet derivative (see Definition 4.2.2) of (5.13) with respect to ψ and we equal it to zero:

$$\begin{aligned}&\int \left(-\frac{i}{\kappa}\frac{\partial}{\partial t} + V\right)\psi\left(\frac{i}{\kappa}\frac{\partial}{\partial t} + V\right)\tilde{\psi}^* + \left(-\frac{i}{\kappa}\frac{\partial}{\partial t} + V\right)\tilde{\psi}\left(\frac{i}{\kappa}\frac{\partial}{\partial t} + V\right)\psi^*\\ &+\int \left(-\frac{i}{\kappa}\nabla - \mathbf{A}\right)\psi\cdot\left(\frac{i}{\kappa}\nabla - \mathbf{A}\right)\tilde{\psi}^* + \left(-\frac{i}{\kappa}\nabla - \mathbf{A}\right)\tilde{\psi}\cdot\left(\frac{i}{\kappa}\nabla - \mathbf{A}\right)\psi^*\\ &+\int \left(\psi\tilde{\psi}^* + \tilde{\psi}\psi^*\right) - \int \left(|\psi|^2\tilde{\psi} + |\psi|^2\tilde{\psi}^*\right) = 0,\end{aligned} \tag{5.14}$$

for every test function $\tilde{\psi}$. Integrating by parts with respect to time in the first integral, and with respect to space in the second integral, we obtain the equation of motion and the boundary condition for the order parameter:

$$\begin{aligned}&\left(-\frac{i}{\kappa}\frac{\partial}{\partial t}+V\right)^2\psi-\left(-\frac{i}{\kappa}\nabla-\mathbf{A}\right)^2\psi+\psi-|\psi|^2\psi=0 \quad \text{in } \Omega,\\ &\left(-\frac{i}{\kappa}\nabla-\mathbf{A}\right)\psi\cdot\mathbf{n}=0 \quad \text{on } \Gamma.\end{aligned} \tag{5.15}$$

5.3.2. Equation of motion for the vector potential A

We take the Fréchet derivative of (5.13) with respect to **A** and we equal it to zero:

$$\begin{aligned}&\int 2\frac{\partial\mathbf{B}}{\partial t}\cdot\left(\frac{\partial\mathbf{A}}{\partial t}+\nabla V\right)-\int 2\nabla\times\mathbf{B}\cdot\nabla\times\mathbf{A}\\ &\quad+\int\mathbf{B}\cdot\frac{1}{i\kappa}\left(\psi^*\nabla\psi-\psi\nabla\psi^*\right)+\int 2\mathbf{B}\cdot\mathbf{A}|\psi|^2=0,\end{aligned} \tag{5.16}$$

for every test function **B**. An integration by parts with respect to time in the first integral, and space in the second, gives the equation of motion and the boundary condition for the vector potential:

$$\begin{aligned}&\nabla\times\nabla\times\mathbf{A}+\left(\frac{\partial^2\mathbf{A}}{\partial t^2}+\frac{\partial}{\partial t}\nabla V\right)\\ &=\frac{1}{2i\kappa}\left(\psi^*\nabla\psi-\psi\nabla\psi^*\right)-\mathbf{A}|\psi|^2+\nabla\times\mathbf{H}, \quad \text{in } \Omega,\\ &\nabla\times\mathbf{A}\times\mathbf{n}=\mathbf{H}\times\mathbf{n} \quad \text{on } \Gamma.\end{aligned} \tag{5.17}$$

Remark 5.3.1. *The terms in red are added to the original model to take into account an applied field* ***H****.*

5.3.3. Constraint on the electric potential

To derive the constraint on the electric potential V, we take the Fréchet derivative of (5.13) with respect to V and equal it to zero; we obtain:

$$\begin{aligned}&\int 2\nabla\tilde{V}\cdot\left(\frac{\partial\mathbf{A}}{\partial t}+\nabla V\right)+\int\left(\frac{i}{\kappa}\frac{\partial\psi^*}{\partial t}+V\psi^*\right)\psi\tilde{V}\\ &\quad+\left(-\frac{i}{\kappa}\frac{\partial\psi}{\partial t}+V\psi\right)\psi V=0,\end{aligned} \tag{5.18}$$

for every test function $\tilde{V}$. Integrating by parts with respect to space in the first integral, we deduce the following constraint and boundary condition for the electric potential:

$$\begin{aligned}&-\text{div}\left(\frac{\partial\mathbf{A}}{\partial t}+\nabla V\right)+V|\psi|^2+\frac{1}{\kappa}\Im\left(\psi^*\frac{\partial\psi}{\partial t}\right)=0 \quad \text{in } \Omega.,\\ &\left(\frac{\partial\mathbf{A}}{\partial t}+\nabla V\right)\cdot\mathbf{n}=0 \quad \text{on } \Gamma.\end{aligned} \tag{5.19}$$

Since we have $\mathbf{E} = -\left(\frac{\partial \mathbf{A}}{\partial t} + \nabla V\right)$ where $\mathbf{E}$ is the electric field, (5.19) can be rewritten as:

$$\begin{aligned} &\operatorname{div} \mathbf{E} + V|\psi|^2 + \frac{1}{\kappa}\Im\left(\psi^* \frac{\partial \psi}{\partial t}\right) = 0 \quad \text{in } \Omega., \\ &\mathbf{E}\cdot\mathbf{n} = 0 \quad \text{on } \Gamma \end{aligned} \tag{5.20}$$

Equations (5.16), (5.17) and (5.20) constitute the Abelian-Higgs model in its most general form. For simplicity we concentrate on a 1D model.

5.4. One-dimensional model

We start by making a few hypotheses to rewrite the 3D Lagrangian (5.12) in a 1D form. We make the following assumptions.

1. The vector potential can be written as $\mathbf{A} = (A, 0, 0)$, where A depends on x and t.
2. The order parameter ψ depends on x and t; it is complex valued.
3. $\nabla \times \mathbf{A}$ is replaced by $\frac{\partial A}{\partial x}$.
4. The electric potential V is zero.

With these hypotheses the Lagrangian (5.12) can be written as:

$$\mathcal{L} = \left(\frac{\partial A}{\partial t} + \frac{\partial V}{\partial x}\right)^2 - \left(\frac{\partial A}{\partial x}\right)^2 + \left[\left|-\frac{i}{\kappa}\frac{\partial \psi}{\partial t} + V\psi\right|^2 - \left|-\frac{i}{\kappa}\frac{\partial}{\partial x}\psi - A\psi\right|^2 + |\psi|^2 - \frac{1}{2}|\psi|^4\right] I(x), \tag{5.21}$$

where $I(x) = \mathbb{1}_{[-L,L]}$ and $[-L, L]$ is the domain of the superconductor. Considering the hypothesis on V and developing (5.21) we obtain:

$$\mathcal{L} = \left(\frac{\partial A}{\partial t}\right)^2 - \left(\frac{\partial A}{\partial x}\right)^2 + I(x)\left[\frac{1}{\kappa^2}\left|\frac{\partial \psi}{\partial t}\right|^2 - \frac{1}{\kappa^2}\left|\frac{\partial \psi}{\partial x}\right|^2 + i\frac{1}{\kappa}A\left(\psi\frac{\partial \psi^*}{\partial x} - \psi^*\frac{\partial \psi}{\partial x}\right) + |\psi|^2(1 - A^2) - \frac{1}{2}|\psi|^4\right]. \tag{5.22}$$

The least action principle is equivalent to the following Euler-Lagrange system:

$$\begin{aligned} \frac{\partial}{\partial t}\left(\frac{\partial \mathcal{L}}{\partial \frac{\partial A}{\partial t}}\right) + \frac{\partial}{\partial x}\left(\frac{\partial \mathcal{L}}{\partial \frac{\partial A}{\partial x}}\right) - \frac{\partial \mathcal{L}}{\partial A} &= 0, \\ \frac{\partial}{\partial t}\left(\frac{\partial \mathcal{L}}{\partial \frac{\partial \psi^*}{\partial t}}\right) + \frac{\partial}{\partial x}\left(\frac{\partial \mathcal{L}}{\partial \frac{\partial \psi^*}{\partial x}}\right) - \frac{\partial \mathcal{L}}{\partial \psi^*} &= 0. \end{aligned}$$

The equation for A is:

$$\frac{\partial^2 A}{\partial t^2} - \frac{\partial^2 A}{\partial x^2} = I(x)\left[i\frac{1}{2\kappa}\left(\psi\frac{\partial \psi^*}{\partial x} - \psi^*\frac{\partial \psi}{\partial x}\right) - A|\psi|^2\right]. \tag{5.23}$$

For ψ we obtain:

$$\begin{aligned}&I(x)\left[-\frac{1}{\kappa^2}\frac{\partial^2\psi}{\partial t^2}+\frac{1}{\kappa^2}\frac{\partial^2\psi}{\partial x^2}-\frac{i}{\kappa}\left(\frac{\partial A}{\partial x}\psi+2A\frac{\partial\psi}{\partial x}\right)+\psi(1-|\psi|^2-A^2)\right]\\&+\delta(x)\left(-\frac{i}{\kappa}A\psi+\frac{1}{\kappa^2}\frac{\partial\psi}{\partial x}\right)=0,\end{aligned} \tag{5.24}$$

where $\delta(x)$ is the Dirac distribution corresponding to the x-derivative of the characteristic function $I(x)$.

To obtain the boundary conditions, we integrate (5.23) over one of the edges of the domain. For example, for $x=-L$ we obtain:

$$\int_{-L-\epsilon}^{-L+\epsilon}\frac{\partial^2 A}{\partial t^2}-\left[\frac{\partial A}{\partial x}\right]_{-L-\epsilon}^{-L+\epsilon}=\int_{-L}^{-L+\epsilon}\left[i\frac{1}{2\kappa}\left(\psi\frac{\partial\psi^*}{\partial x}-\psi^*\psi_x\right)-A|\psi|^2\right].$$

Taking the limit $\epsilon\to 0$ and assuming bounded variations of the integrands, we obtain that $\frac{\partial A}{\partial x}$ is continuous at the interface $x=-L$. The second equation gives:

$$\int_{-L-\epsilon}^{-L+\epsilon}\left[-\frac{1}{\kappa^2}\frac{\partial^2\psi}{\partial t^2}+\frac{1}{\kappa^2}\frac{\partial^2\psi}{\partial x^2}+\dots\right]+\left(-\frac{i}{\kappa}A\psi+\frac{1}{\kappa^2}\frac{\partial\psi}{\partial x}\right)_{x=-L}=0.$$

Taking the limit $\epsilon\to 0$ and assuming that the bracket in the integral is bounded, we recover the classical boundary condition at the edge of the superconductor:

$$-iA\psi+\frac{1}{\kappa}\frac{\partial\psi}{\partial x}=0. \tag{5.25}$$

To summarize, we rewrite the system of equations of our 1D Abelian-Higgs model:

$$\begin{aligned}&-\frac{1}{\kappa^2}\frac{\partial^2\psi}{\partial t^2}+\frac{1}{\kappa^2}\frac{\partial^2\psi}{\partial x^2}-\frac{i}{\kappa}\left(\frac{\partial A}{\partial x}\psi+2A\frac{\partial\psi}{\partial x}\right)+\psi(1-|\psi|^2-A^2)=0\quad\text{in } [-L,L],\\&\frac{\partial^2 A}{\partial t^2}-\frac{\partial^2 A}{\partial x^2}=I(x)\left[i\frac{1}{2\kappa}\left(\psi\frac{\partial\psi^*}{\partial x}-\psi^*\frac{\partial\psi}{\partial x}\right)-A|\psi|^2\right]\quad\text{in } \mathbb{R},\\&\frac{\partial A}{\partial x}\text{ is continuous at the interface } x=\pm L,\\&-iA\psi+\frac{1}{\kappa}\frac{\partial\psi}{\partial x}=0\quad\text{at } x=\pm L.\end{aligned} \tag{5.26}$$

We can rewrite the system (5.26) using hydrodynamic variables. We set $\psi=\rho e^{i\theta}$, then (5.26) becomes

$$\begin{aligned}&\frac{\partial^2\rho}{\partial t^2}-\frac{\partial^2\rho}{\partial x^2}=\rho\left(\left(\frac{\partial\theta}{\partial t}\right)^2-\left(\frac{\partial\theta}{\partial x}\right)^2\right)+2\kappa A\rho\frac{\partial\theta}{\partial x}+\kappa^2\rho(1-\rho^2-A^2)\quad\text{in } [-L,L],\\&\frac{\partial^2\theta}{\partial t^2}-\frac{\partial^2\theta}{\partial x^2}=\frac{2}{\rho}\left(\frac{\partial\theta}{\partial x}\frac{\partial\rho}{\partial x}-\frac{\partial\theta}{\partial t}\frac{\partial\rho}{\partial t}\right)-\kappa\frac{\partial A}{\partial x}-2\kappa A\frac{1}{\rho}\frac{\partial\rho}{\partial x}\quad\text{in } [-L,L],\\&\frac{\partial^2 A}{\partial t^2}-\frac{\partial^2 A}{\partial x^2}=I(x)\rho^2\left(\frac{1}{\kappa}\frac{\partial\theta}{\partial x}-A\right)\quad\text{in } \mathbb{R}.\end{aligned} \tag{5.27}$$

The interface condition at $x = \pm L$ is

$$\frac{\partial \rho}{\partial x} = 0, \quad \frac{\partial \theta}{\partial x} = \kappa A. \tag{5.28}$$

We have not used that standard notation $\psi = \sqrt{\rho} e^{i\theta}$ since in this case the system for ρ and θ is more complex.

We notice from $(5.27)_1$ and $(5.27)_3$ that, apart from the trivial solution $\rho = 1$, $A = 0$, $\theta = \theta_0$ where θ_0 is a constant, we have the solution:

$$A = A_\infty, \quad \rho = 1, \quad \frac{\partial \theta}{\partial x} = \kappa A_\infty, \tag{5.29}$$

where A_∞ is a constant.

5.5. Numerical results

In this section, we study numerically the 1D Abelian-Higgs model (5.26). In the first paragraph we describe, the finite difference scheme and construct a *manufactured* system to validate the convergence of the scheme. We call manufactured system, a system of partial differential equations of which we know the exact solution, called a manufactured solution. In the second paragraph, we analyse the response of the model to a Gaussian pulse and highlight the importance of defects to get a non trivial solution of type (5.29).

5.5.1. Study of a manufactured solution

Preliminary analysis

In this section, we construct a family of solutions for the simpler following system (it corresponds to (5.26) where ψ is real so that we set all imaginary terms to zero):

$$\left\{ \begin{array}{lll} \dfrac{\partial^2 A}{\partial t^2} & = \dfrac{\partial^2 A}{\partial x^2} - A|\psi|^2 & \text{in } \mathbb{R}, \\ \dfrac{1}{\kappa^2}\dfrac{\partial^2 \psi}{\partial t^2} & = \dfrac{1}{\kappa^2}\dfrac{\partial^2 \psi}{\partial x^2} + \psi(1 - \psi^2 - A^2) & \text{in } \mathbb{R}, \\ A(t=0) & = A_0(x), & \end{array} \right. \tag{5.30}$$

where A_0 is a given initial state.

We have found a particular solution of the Abelian-Higgs system (5.30). Our method is inspired from the one used in Di Bartolo and Dorsey (1996) for the TDGL model. We search solutions of the following form:

$$\begin{array}{l} A(x,t) = Q(X), \\ \psi(x,t) = F(X), \\ \text{with } X = x - ct \text{ and } F + Q = 1. \end{array} \tag{5.31}$$

We have the following result:

Proposition 5.5.1. *The Abelian-Higgs* (5.30) *system is consistent with* (5.31) *if* $\kappa^2 = \dfrac{1}{2}$.

Proof. With our notations, (5.30) becomes

$$\begin{aligned} \frac{\partial^2 A}{\partial t^2} &= \frac{\partial^2 A}{\partial x^2} - A|\psi|^2 \Rightarrow F^3 - F^2 + (c^2-1)F'' = 0, \\ \frac{1}{\kappa^2}\frac{\partial^2 \psi}{\partial t^2} &= \frac{1}{\kappa^2}\frac{\partial^2 \psi}{\partial x^2} + \psi(1-\psi^2-A^2) \Rightarrow F^3 - F^2 + \frac{1}{2\kappa^2}(c^2-1)F'' = 0. \end{aligned} \tag{5.32}$$

And the result follows. □

In the above proof we see that if $\kappa^2 = \dfrac{1}{2}$ then finding a solution of system (5.30) amounts to solving the differential equation $F^3 - F^2 + (c^2-1)F'' = 0$. The following proposition gives a particular solution.

Proposition 5.5.2. *A particular solution for* $F^3 - F^2 + (c^2-1)F'' = 0$ *is given by* $F(X) = \dfrac{6(c^2-1)}{X^2 + \frac{9}{2}(c^2-1)}$.

Proof. We use the classical method for a conservative system: we multiply by F' then integrate. We find:

$$F'^2 = -\frac{1}{2(c^2-1)}F^4 + \frac{2}{3(c^2-1)}F^3 + K, \tag{5.33}$$

where K is an arbitrary constant; we choose $K = 0$ for convenience. Provided $F \leq \dfrac{4}{3}$ we can take the square root of both sides and obtain:

$$\frac{dF}{dX} = \frac{1}{\sqrt{2(c^2-1)}}\sqrt{-F^4 + \frac{4}{3}F^3}. \tag{5.34}$$

We now separate variable F and X and integrate both sides:

$$X - X_0 = \sqrt{2(c^2-1)}\int_{X_0}^{X} \frac{\mathrm{d}F}{F\sqrt{F(\frac{4}{3}-F)}}. \tag{5.35}$$

We observe that a first integral of $\dfrac{1}{F\sqrt{F(\frac{4}{3}-F)}}$ is given by $-\dfrac{3}{2}\sqrt{\dfrac{\frac{4}{3}-F}{F}}$. Then taking $F(X_0) = \dfrac{4}{3}$ we deduce:

$$X - X_0 = -\frac{3\sqrt{2(c^2-1)}}{2}\sqrt{\frac{\frac{4}{3}-F}{F}}. \tag{5.36}$$

Choosing $X_0 = 0$ and raising (5.36) to the power of two we finally obtain:

$$F(X) = \frac{6(c^2-1)}{X^2 + \frac{9}{2}(c^2-1)}. \tag{5.37}$$

□

We deduce from proposition (5.5.2) the following particular solution of the Abelian-Higgs system in the real case:

$$(A(x,t), \psi(x,t)) = \left(\frac{(x-ct)^2 - \frac{3}{2}(c^2-1)}{(x-ct)^2 + \frac{9}{2}(c^2-1)}, \frac{6(c^2-1)}{(x-ct)^2 + \frac{9}{2}(c^2-1)} \right). \tag{5.38}$$

We now turn to the numerical solving of (5.30). It is discretized:

- in space using a second order centred finite difference scheme,
- in time using a Runge-Kutta 4 scheme.

We approximate the real line by a finite domain $[-L, L]$ and take absorbing boundary conditions at $x = \pm L$.
The parameters are the following :

- $\kappa = \dfrac{1}{\sqrt{2}}$,
- $c = \sqrt{2}$,
- $\Delta t = 5 \times 10^{-4}$,
- $(A_0(x), \psi_0(x)) = (A(0,x), \psi(0,x))$ from (5.38).

Figure (5.1) left shows the evolution of the solution, a solitary wave called *soliton* between $t = 0$ and $t = 40$ when $L = 60$. Figure 5.1 right shows the convergence analysis results, for different choices of L. We see that the order in space is two, which is consistent with our space discretization. In addition, we see that L has to be sufficiently large to ensure good convergence properties at a given final time.

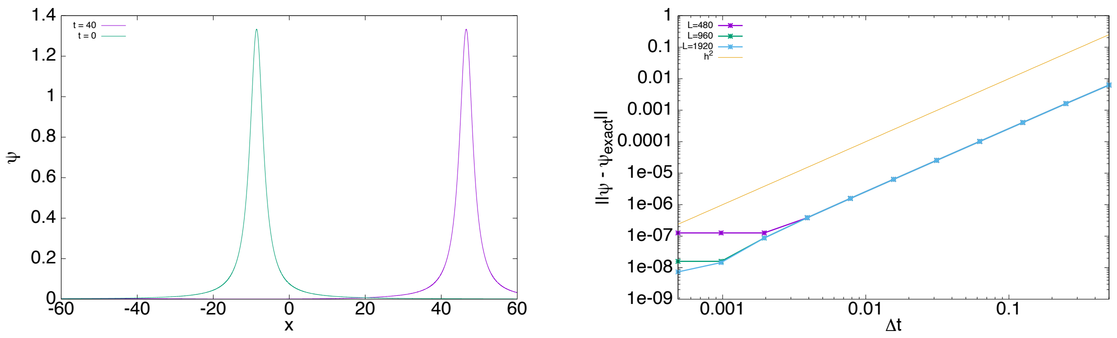

Figure 5.1. *Evolution of the particular solution ψ at $t = 0$ and $t = 40$ with a domain of length $L = 60$ (left). Error $||\psi - \psi_{exact}||_\infty$ between exact and computed solution in logarithmic scale at $t = 1$, for three lengths, $L = 480, 960, 1920$ (right).*

Derivation of a manufactured system

In this section, we try to find a manufactured solution of (5.27). This system can be formally written as $\mathcal{F}(A, \psi) = 0$. No exact solution has been found, but it is possible to use a similar method as in the previous section. We cast the system in the form $\mathcal{F}(A, \psi) = \mathcal{F}(A_0, \psi_0)$ where $\mathcal{F}(A_0, \psi_0)$ is a non zero right-hand-side term and (A_0, ψ_0) a particular solution. We also want $\mathcal{F}(A_0, \psi_0)$ to be as simple as possible.

We set

$$\begin{aligned}
&A(x,t) = Q(X),\\
&\rho(x,t) = F(X),\\
&\Theta(X) = \int Q(X),\\
&\text{with } X = x - ct \text{ and } F + Q = 1.
\end{aligned} \tag{5.39}$$

We denote $\theta : (x,t) \mapsto \Theta(x-ct)$. In the rest of the section, for clarity, we use the index notation for derivatives (e.g. u_x means $\frac{\partial u}{\partial x}$).

Proposition 5.5.3. *Written with the variable Q, the system (5.27) becomes:*

$$\begin{aligned}
&(i) \quad (c^2-1)Q'' = Q^2(2\kappa + 2\kappa^2) - Q^3(2\kappa^2 + 2\kappa + 1 - c^2),\\
&(ii) \quad Q'(3c^2 - 3\kappa - 3) = -2\kappa\frac{Q'}{Q},\\
&(iii) \quad (c^2-1)Q'' = Q^2 - Q^3\left(\frac{1}{\kappa}+1\right).
\end{aligned} \tag{5.40}$$

We cannot find (Q, c, κ) such that the system (5.40) is satisfied exactly but we can make it consistent for (i) and (iii). For (i) and (iii) to be identical, we have to find (c, κ) such that

$$\begin{aligned}
&2\kappa^2 + 2\kappa = 1,\\
&2\kappa^2 + 2\kappa + 1 - c^2 = 1 + \frac{1}{\kappa}.
\end{aligned} \tag{5.41}$$

A solution of (5.41) is:

$$\begin{aligned}
&c = 3^{\frac{1}{4}},\\
&\kappa = \frac{-1-\sqrt{3}}{2}.
\end{aligned} \tag{5.42}$$

The equation to solve is:

$$Q'' = \frac{Q^3}{2}(-2+\sqrt{3})(1+\sqrt{3}) + \frac{Q^2}{2}(1+\sqrt{3}). \tag{5.43}$$

A similar analysis as in the previous section leads to the manufactured solution:

$$Q(X) = \frac{12(2+\sqrt{3})}{(1+\sqrt{3})(2+\sqrt{3})X^2 + 9}. \tag{5.44}$$

From (5.39) and (5.44) we deduce an explicit form of a particular solution (A_0, ψ_0):

$$\begin{aligned}
&A_0 = \frac{2X^2 + 15\sqrt{3} - 33}{2X^2 + 27\sqrt{3} - 45},\\
&\rho_0 = \frac{12(2+\sqrt{3})}{(1+\sqrt{3})(2+\sqrt{3})X^2 + 9},\\
&\theta_0 = \frac{4\sqrt{2+\sqrt{3}}}{\sqrt{1+\sqrt{3}}}\arctan\left(\frac{1}{3}\sqrt{(1+\sqrt{3})(2+\sqrt{3})}X\right),
\end{aligned} \tag{5.45}$$

where $X = x - 3^{0.25}t$.

Equations (5.27)$_1$ and (5.27)$_3$ are verified exactly by solution (5.45). Equation (5.27)$_2$ is not verified, so we have additional terms. After calculation we end up with the following manufactured system, written in hydrodynamic variables (A, ρ, θ):

$$\begin{aligned}
&\rho_{tt} - \theta_t^2\rho - \rho_{xx} + \theta_x^2\rho - 2\kappa A\rho\theta_x - \rho\kappa^2(1 - A^2 - \rho^2) = 0,\\
&\theta_{tt} + 2\theta_t\frac{\rho_t}{\rho} - (\theta_{xx} - 2\frac{\theta_x\rho_x}{\rho}) + 2\kappa A\frac{\rho_x}{\rho} + \kappa A_x = -Q'\left(\frac{3}{2}(1 - 3\sqrt{3}) + \frac{1+\sqrt{3}}{Q}\right),\\
&A_{tt} - A_{xx} - \frac{1}{\kappa}\rho^2\theta_x + A\rho^2 = 0.
\end{aligned} \tag{5.46}$$

From (5.46) and (5.26) the manufactured system written in ordinary variables (A, u, v) where $\psi = u + iv$ is:

$$\begin{aligned}
&u_{tt} - u_{xx} - \kappa(A_x v + 2Av_x) - \kappa^2 u(1 - |\psi|^2 - A^2) = -\rho_0\sin(\theta_0) \times RHS,\\
&v_{tt} - v_{xx} + \kappa(A_x u + 2Au_x) - \kappa^2 v(1 - |\psi|^2 - A^2) = \rho_0\cos(\theta_0) \times RHS,\\
&A_{tt} - A_{xx} - \frac{1}{2i\kappa}(\psi^*\psi_x - \psi\psi_x^*) + A|\psi|^2 = 0,
\end{aligned} \tag{5.47}$$

where $RHS := -Q'\left(\frac{3}{2}(1 - 3\sqrt{3}) + \frac{1+\sqrt{3}}{Q}\right)$ denotes the non-zero right-hand-side term obtained in (5.46)$_2$.

Numerical results

In this paragraph, we compute solutions of (5.47) and compare them to the exact solutions (5.45). We study the convergence in time of three different schemes: explicit Euler, Runge-Kutta 2 and Runge-Kutta 4. We use a second order centred scheme in space. Our goal is to retrieve the classical convergence orders for these schemes. The computational domain is shown in Fig. 5.2.

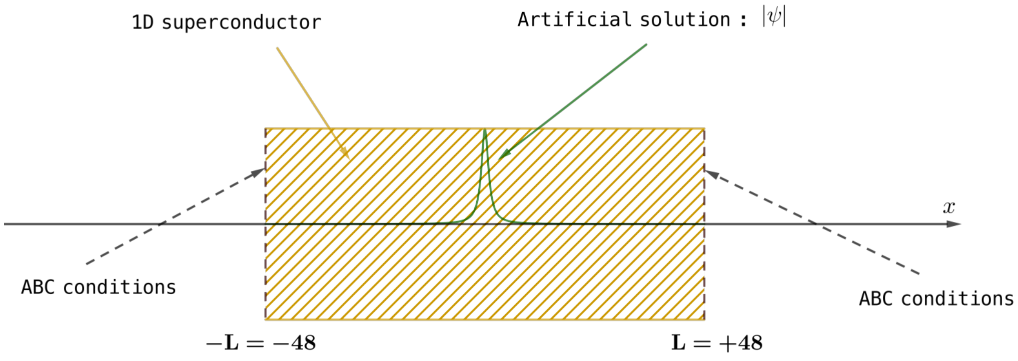

Figure 5.2. *Computational domain for the manufactured system* (5.47)*. The amplitude of* ψ *at initial time is shown.*

The results are shown in Figs. 5.3. The order in space is two, as expected from our discretization. In time, the expected orders are correctly retrieved. We emphasize that we have to resort to a higher order in space in order to show the order for Runge-Kutta 4. More specifically, if a quantity u is to be computed and we denote u_h its discretised value, then in the Runge-Kutta 4 case, we have:

$$||u - u_h|| = \mathrm{O}(\Delta t^4 + \Delta x^q), \tag{5.48}$$

where q depends on the discretization in space and $q > 4$. In this case we choose a sixth-order compact scheme Lele (1992) ($q = 6$).

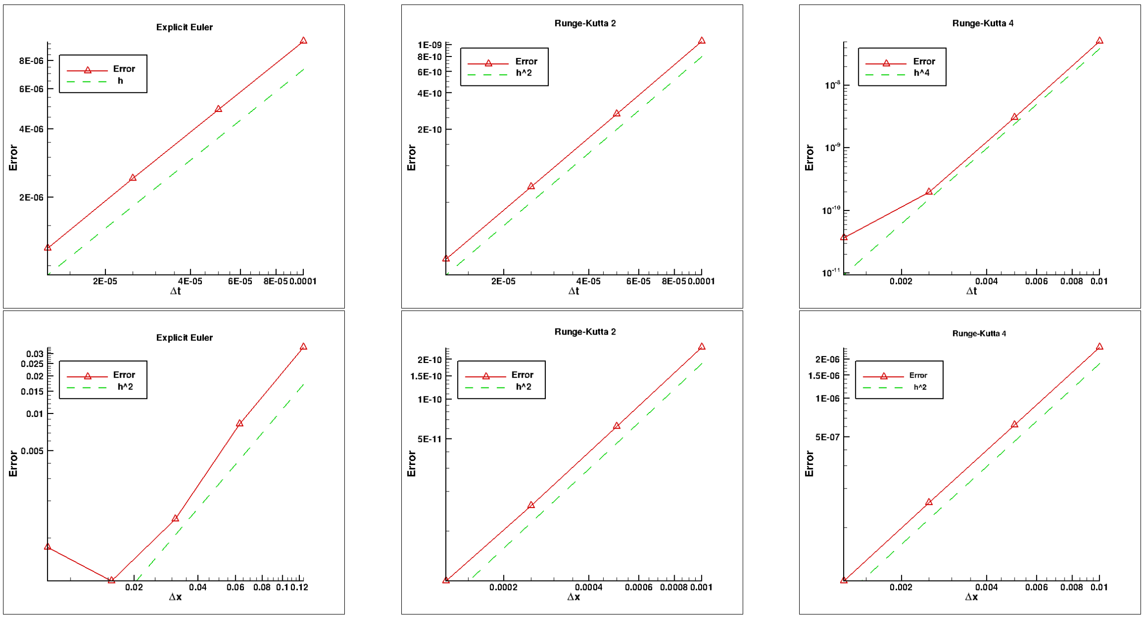

Figure 5.3. *Convergence curves. In red, convergence curves in time (above) and space (below) for the three schemes. Dashed lines are the expected orders. All errors are computed with the infinite norm.*

In the next section we use our scheme to analyse the response of the model to a Gaussian pulse.

5.5.2. Response to a Gaussian pulse

As already mentioned in the introduction, the trapped flux property is central in applications. One way to achieve it is to apply and remove a large applied magnetic field. If the field is applied via a pulse on a pre-cooled material then we speak of pulse field magnetization (PFM). Our goal is to describe the response of our model to such a pulse.

Defects

To make the model (5.26) more realistic we introduce defects. In our case, this amounts to choose α in (5.1) as space dependent (Sørensen et al., 2017). Then the equation for ψ takes the form:

$$\frac{\partial^2\psi}{\partial t^2}=\frac{\partial^2\psi}{\partial x^2}-i\kappa\left(\frac{\partial A}{\partial x}\psi+2A\frac{\partial\psi}{\partial x}\right)+\kappa^2\psi\left(s-|\psi|^2-A^2\right), \tag{5.49}$$

where $s(x)$ is a defect function. It takes the value -1 at nodes where there is a defect otherwise its value is 1. We suppose that the defect consists of one node and that the defects are regularly spaced.

The applied pulse is of the form $A_0(x) = a_0\exp(-\frac{x^2}{2w_0})$. By making the change of variable $A = A' + A_0(x-t)$ the model becomes:

$$\begin{aligned}
&\frac{\partial^2 A'}{\partial t^2}-\frac{\partial^2 A'}{\partial x^2}=I(x)\left[i\frac{1}{2\kappa}\left(\psi\frac{\partial\psi^*}{\partial x}-\psi^*\frac{\partial\psi}{\partial x}\right)-(A'+A_0)|\psi|^2\right],\\
&\frac{\partial^2\psi}{\partial t^2}-\frac{\partial^2\psi}{\partial x^2}=-i\kappa\left(\frac{\partial A'}{\partial x}\psi+2(A'+A_0)\frac{\partial\psi}{\partial x}\right)+\kappa^2\psi\left(s(x)-|\psi|^2-(A'+A_0)^2\right),\\
&-i(A'+A_0)\psi+\frac{1}{\kappa}\frac{\partial\psi}{\partial x}=0,\quad x=\pm L.
\end{aligned} \tag{5.50}$$

Numerical results

Figure 5.4 shows the influence of defects on the average in space of the vector potential. We see that defects trigger a non zero trapped A_∞. In addition, the gradient of the phase verifies $\frac{\partial\theta}{\partial x}=\kappa A_\infty$. In Fig. 5.5, we report the average of ψ both in time and space. We observe a monotonic decrease with respect to the density of defects (here defined as the ratio between the number of nodes with a defect and the number of nodes without a defect). In a real material, defects are known to pin vortices, so more defects mean more pinned vortices and as a consequence the mean value of ψ is reduced; our results are consistent with this intuitive picture. We report below details about the chosen parameters:

- ⋆ GL parameter: $\kappa = 1$,
- ⋆ $x_{min} = -15$, $x_{max} = +15$, $L = 11.53$,
- ⋆ Abscissa of the pulse: $x_0 = -200$,
- ⋆ Width of the pulse: $w_0 = 50$,
- ⋆ Amplitude of the pulse = $a_0 = 3$,
- ⋆ Space step: $\Delta x = 7.69\mathrm{e}-3$,

- ⋆ Time step: $\Delta t = 0.001$,
- ⋆ End time: $t = 40000$,
- ⋆ size of the defect: 1 node,
- ⋆ (for Fig. 5.5) number of nodes between defects: from 26 (3.8%) to 1 (50%),
- ⋆ (for Fig. 5.4) number of nodes between defects: 6,
- ⋆ Discretization in time: RK4 scheme.

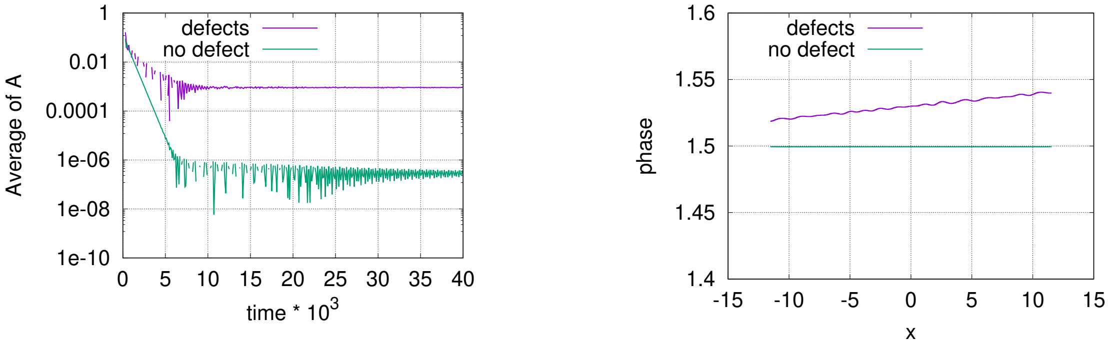

Figure 5.4. *Time evolution of the averaged A (left) and the phase θ (right) considering the presence or the absence of defects.*

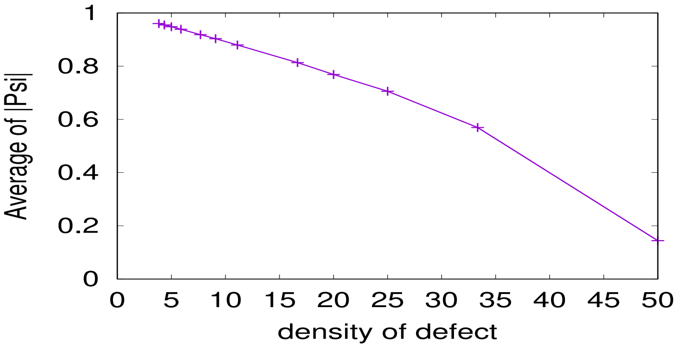

Figure 5.5. *Space and time average of $|\psi|$ as a function of the density of defects (%).*

6. Conclusion

In this study, we have addressed the problem of modelling type II superconductors. Four models have been tackled: the London model, the TDGL model, the steady state GL model and the Abelian-Higgs model.

For the London model, we have focused on a problem with cylindrical symmetry. In 2D, the introduction of an hydrodynamic variable, called stream function, has enabled to simplify the expression of the London equation written originally with the vector potential. This has led us to prove a mathematical result about existence and uniqueness of a solution for our problem. This formulation has also provided an alternative way to model the magnetic field outside the superconductor. We have shown remarkable agreement between the two methods. We have also conducted a 3D study. A classical path was first followed by considering a bounded external box where conditions at infinity are applied. Second, an alternative formulation was used to tackle the conditions at infinity by introducing boundary elements. These elements have been recently added to FreeFEM. We have shown that the BEM method indeed improves the results.

Out aim by studying the TDGL model was to provide efficient finite element discretizations in view of an implementation with FreeFEM. We have first proposed a numerical scheme using only Lagrange finite elements. It has been tested successfully in 2D for both convex and non convex geometries. The drawback is that it has not been possible to consider a general curved polygonal domain due to the condition $\mathbf{A} \cdot \mathbf{n} = 0$ on the boundary. The second scheme was proposed by Gao and Sun (2015). It is a mixed finite element formulation of the TDGL equations. The introduction of Raviart-Thomas finite elements makes it simple to treat the condition $\mathbf{A} \cdot \mathbf{n} = 0$. Moreover, defining a complex mesh structure is not difficult with FreeFEM. We have been able to solve the TDGL equations in a sphere or a sphere with a geometrical defect, for example. The codes have been written in the general ω-gauge framework. Besides, we have conducted a detailed analysis on the influence of the gauge parameter ω on the convergence properties of the numerical scheme. This has lead us to conclude in the existence of an optimal gauge. However, this result depends on the size of the mesh and in practice the Lorentz gauge gives the best convergence properties. Finally, a change of the gauge parameter can serve as a perturbation of the final state; in this way we have discovered new vortex patterns for a 2D classical benchmark.

The steady state GL model was an opportunity to look into more advanced numerical tools like the Sobolev gradient flow techniques. These methods were introduced by the mathematical community (Neuberger and Renka, 1998). These ideas were applied successfully to Gross-Pitaevskii equation by Danaila and Kazemi (2010). We have extended this method to GL equations. In most cases, we have retrieved the equilibrium patterns given by the classical TDGL model. However, a new pattern has been discovered for a classical benchmark. The Sobolev Gradient method is an imaginary time technique, i.e. that we lose the real physical dynamics and focus on the final state. The advantage is that we can use Lagrange finite elements even in a curved polygonal domain as we have shown in the case of a disk with a boundary defect. Another benefit is the low computational cost of the method compared to TDGL simulations.

In investigating the Abelian-Higgs model, we have developed an original 1D model and a finite differences code in Fortran. To validate our scheme, we have constructed a manufactured solution which is actually a soliton. Our goal was to predict a magnetization effect, which is standard in PFM experiments. We reached the conclusion that a non zero vector potential can be trapped if we introduce defects in the domain.

Future work

In the London model, we have fixed the London length to be $\lambda = 1.6 \times 10^{-7}$. It means we cannot actually see the penetration of the magnetic field in the superconducting domain. We could vary λ and analyse for instance the regularity of the fields (vector potential, magnetic field) near the edges of the superconductor. We could also go further with the hydrodynamic approach, in particular with the analogy with vortex rings. Explicit formula might be found for the stream function in some special cases as is done in Danaila et al. (2021). Finally, one could try to extend these ideas to the GL equations.

In the TDGL simulations, we did not consider the coupling with the exterior as we have done for the London model. This approach would be more rigorous since the external field is actually uniform only at infinity due to the demagnetization field.

Sobolev gradient techniques have proven to be effective to solve steady state GL equations with a very low computational cost. We could wonder if these ideas can extend to the TDGL model. In addition we could improve the method itself by applying the descent method to the discretized energy in the spirit of Kazemi and Renka (2013).

In conclusion, the dynamics of vortices have proven to be rich and complex both in 2D and 3D. It could be of great interest to investigate cases with more vortices and see how they move, arrange and possibly interact as is the case in quantum turbulence observed in superfluids (Brachet et al., 2023).

A. Appendix A

A.1. Feynman's model for superconductivity

In this section, we present the model for superconductors introduced by Feynman (1998). First we show the correspondence between Feynman's constants and GL coefficients α and β. Then, we compare Feynman's model with the Gross-Pitaevskii equation used to model superfluids and in particular Bose-Einstein condensates (Pitaevskii and Stringari, 2003). Our goal is to highlight formal links between these different models.

A.1.1. Comparison of Feynman's model with Ginzburg-Landau

We start with the Lagrangian for a charged particle q of mass m moving in a magnetic field and an electric potential ϕ

$$\begin{aligned}\mathcal{L}_f = \frac{1}{2m}\left[\left(\frac{\hbar}{i}\nabla - q\mathbf{A}\right)\psi\right]\left[\left(\frac{\hbar}{i}\nabla - q\mathbf{A}\right)\psi\right]^* \\ +q\phi\psi^*\psi + \frac{\hbar}{i}\psi^*\dot{\psi} + \frac{\alpha_f}{2}(|\psi|^2 - \rho_s)^2.\end{aligned} \tag{A.1}$$

where the f in α_f means *Feynman* so as not to confuse it with the α from GL theory. It leads to the following nonlinear Schrödinger equation, called Feynman's model:

$$i\hbar\frac{\partial\psi}{\partial t} = \frac{1}{2m}\left[-i\hbar\nabla - q\mathbf{A}\right]^2\psi + q\phi\psi + \alpha_f\psi(|\psi|^2 - \rho_s). \tag{A.2}$$

The TDGL model $(3.8)_1$ reads:

$$-\frac{\hbar^2}{2mD}\frac{\partial\psi}{\partial t} = \frac{1}{2m}\left[-i\hbar\nabla - q\mathbf{A}\right]^2\psi + \frac{\hbar}{2mD}q\phi\psi + \alpha\psi + \beta|\psi|^2\psi, \tag{A.3}$$

The comparison between (A.2) and (A.3) in the steady state case and $\phi = 0$ gives the formal equivalence:

$$\begin{cases}\alpha_f = \beta, \\ -\alpha_f\rho_s = \alpha.\end{cases} \tag{A.4}$$

A.1.2. Comparison of Feynman's model with the Gross-Pitaevskii equation

The GL model and the Feynman's model are very close to the GP equation. In Abid et al. (2003) the following Lagrangian is introduced (to avoid confusion we add the index *gp* refering to Gross-

Pitaevskii)

$$\mathcal{L}_{gp} = \alpha_{gp} i \left(\psi^* \frac{\partial \psi}{\partial t} - \psi \frac{\partial \psi^*}{\partial t} \right) - 2\alpha_{gp}^2 |\nabla \psi|^2 - 2\alpha_{gp} f(|\psi|^2), \tag{A.5}$$

where $\alpha_{gp} = \dfrac{\hbar}{2m}$ and $f(|\psi|^2) = -\Omega|\psi|^2 + \dfrac{\beta_{gp}}{2}|\psi|^4$.

The non linear Schrödinger equation associated with (A.5) is called the *Gross-Pitaevskii* equation. It is given by:

$$i\hbar \frac{\partial \psi}{\partial t} = -\frac{\hbar^2}{2m}\Delta\psi - \hbar\Omega\psi + \hbar\beta_{gp}|\psi|^2\psi. \tag{A.6}$$

The correspondence between (A.2) and (A.6) is achieved provided that $q = 0$ and

$$\begin{cases} \Omega = \dfrac{\alpha_f \rho_s}{\hbar}, \\ \beta_{gp} = \dfrac{\alpha_f}{\hbar}. \end{cases} \tag{A.7}$$

Equations (A.4) and (A.7) link the three models (Feynman, Ginzburg-Landau and Gross-Pitaevskii) from a formal point of view.

A.2. Proof that $H^1(\omega)$ is a Hilbert space

In this section we prove the following proposition.

Proposition A.2.1. *$H^1(\omega)$ defined by (2.36) is a Hilbert space for the following scalar product:*

$$(\Phi, \Psi)_{H^1(\omega)} := \int_\Omega \frac{1}{r}\Phi\Psi + \int_\Omega \frac{1}{r}\nabla\Phi \cdot \nabla\Psi. \tag{A.8}$$

Proof. The bilinear form $(\cdot,\cdot)_{H^1(\omega)}$ is clearly positive. If we have $(\Psi,\Psi)_{H^1(\omega)} = 0$, then $||\Psi||^2_{L^2_\omega} = 0$, and since $\omega > 0$, we have a.e. $\Psi = 0$. The bilinear form $(\cdot,\cdot)_{H^1(\omega)}$ is thus a scalar product. We now prove that $H^1(\omega)$ is complete for the associated norm.

Let $(u_n) \subset H^1(\omega)$ a Cauchy sequence for the norm $||\cdot||_{H^1(\omega)}$, then by definition (2.38), $\omega^{\frac{1}{2}}u_n$ and $\omega^{\frac{1}{2}}\bar{\nabla}u_n$ are Cauchy sequences in L^2. Since L^2 is complete they converge towards v and g in L^2 respectively. We set

$$\begin{aligned} \tilde{v} &= \omega^{-\frac{1}{2}}v, \\ \tilde{g} &= \omega^{-\frac{1}{2}}g. \end{aligned} \tag{A.9}$$

We have the following inequalities:

$$\int_\Omega (u_n - \tilde{v})^2 \leq R_{max}\int_\Omega (\omega^{\frac{1}{2}}u_n - v)^2, \tag{A.10}$$

$$\int_\Omega (\bar{\nabla}u_n - \tilde{g})^2 \leq R_{max}\int_\Omega (\omega^{\frac{1}{2}}\bar{\nabla}u_n - g)^2. \tag{A.11}$$

From which we infer that:

$$u_n \longrightarrow \tilde{v}, \tag{A.12}$$

$$\bar{\nabla}u_n \longrightarrow \tilde{g}. \tag{A.13}$$

Now we verify that $\bar{\nabla}\tilde{v} = \tilde{g}$, which is equivalent to

$$\frac{\partial \tilde{v}}{\partial x_i} = \tilde{g}_i \quad i = 1, 2. \tag{A.14}$$

Let ϕ in $\mathcal{D}(\Omega)$. We have from the definition of weak derivatives

$$\int_\Omega \frac{\partial u_n}{\partial x_i}\phi = -\int_\Omega u_n\frac{\partial \phi}{\partial x_i}. \tag{A.15}$$

Passing to the limit, using (A.12) and (A.13), we obtain:

$$\int_\Omega \tilde{g}_i\phi = -\int_\Omega \tilde{v}\frac{\partial \phi}{\partial x_i}, \tag{A.16}$$

which proves that $\dfrac{\partial \tilde{v}}{\partial x_i} = \tilde{g}_i$.

From (A.9) and (A.14), we have $\tilde{v} \in H^1(\omega)$. In addition

$$||u_n - \tilde{v}||_{H^1(\omega)} = \int_\Omega (\omega^{\frac{1}{2}}u_n - \omega^{\frac{1}{2}}\tilde{v})^2 + \int_\Omega (\omega^{\frac{1}{2}}\bar{\nabla}u_n - \omega^{\frac{1}{2}}\bar{\nabla}\tilde{v})^2. \tag{A.17}$$

Passing to the limit, we have that $u_n \longrightarrow \tilde{v}$ for $|| \cdot ||_{H^1(\omega)}$, which concludes the proof. $\square$

Bibliography

M. Abid, C. Huepe, S. Metens, C. Nore, C. T. Pham, L. S. Tuckerman and M. E. Brachet. Gross–Pitaevskii dynamics of Bose–Einstein condensates and superfluid turbulence. *Fluid Dynamics Research*, 33(5-6):509, 2003.

A. A. Abrikosov. On the Magnetic properties of superconductors of the second group. *Sov. Phys. JETP*, 5:1174–1182, 1957.

R. A. Adams and J. J. F. Fournier. *Sobolev spaces*. Elsevier, 2003.

M. Ainslie and H. Fujishiro. *Numerical Modelling of Bulk Superconductor Magnetisation*. 2053-2563. IOP Publishing, 2019.

T. S. Alstrom, M. P. Sorensen, N. F. Pedersen and S. Madsen. Magnetic Flux Lines in Complex Geometry Type-II Superconductors Studied by the Time Dependent Ginzburg-Landau Equation. *Acta Applicandae Mathematicae*, 115 (1):63–74, 2011.

J. Barba-Ortega, E. Sardella and J. A. Aguiar. Superconducting boundary conditions for mesoscopic circular samples. *Superconductor Science and Technology*, 24(1):015001, 2010.

J. Barba-Ortega, E. Sardella and J. A. Aguiar. Superconducting properties of a parallelepiped mesoscopic superconductor: A comparative study between the 2D and 3D Ginzburg–Landau models. *Physics Letters A*, 379(7):732–737, 2015.

J. Bardeen, L. N. Cooper and J. R. Schrieffer. Theory of Superconductivity. *Phys. Rev.*, 108: 1175–1204, Dec 1957.

C. P. Bean. Magnetization of High-Field Superconductors. *Rev. Mod. Phys.*, 36:31–39, Jan 1964.

P. Bernstein and J. Noudem. Superconducting magnetic levitation: principle, materials, physics and models. *Superconductor Science and Technology*, 33(3):033001, jan 2020.

F. Bethuel, H. Brezis, F. Hélein et al. *Ginzburg-landau vortices*, volume 13. Springer, 1994.

J. Bielak and R. C. MacCamy. An exterior interface problem in two-dimensional elastodynamics. *Quarterly of Applied Mathematics*, 41(1):143–159, 1983.

D. Boffi, F. Brezzi, M. Fortin et al. *Mixed finite element methods and applications*, volume 44. Springer, 2013.

M. Brachet, G. Sadaka, Z. Zhang, V. Kalt and I. Danaila. Coupling Navier-Stokes and Gross-Pitaevskii equations for the numerical simulation of two-fluid quantum flows. *Journal of Computational Physics*, 488:112193, 2023.

E. H. Brandt and G. P. Mikitik. Meissner-London currents in superconductors with rectangular cross section. *Physical review letters*, 85(19):4164, 2000.

J.-G. Caputo, L. Gozzelino, F. Laviano, G. Ghigo, R. Gerbaldo, J. Noudem, Y. Thimont and P. Bernstein. Screening magnetic fields by superconductors: A simple model. *Journal of Applied Physics*, 114(23), 2013.

C. Caroli and K. Maki. Motion of the Vortex Structure in Type-II Superconductors in High Magnetic Field. *Phys. Rev.*, 164:591–607, Dec 1967.

S. J. Chapman. A hierarchy of models for type-II superconductors. *Siam Review*, 42(4):555–598, 2000.

Z. Chen, K.-H. Hoffman and J. Liang. On a Non-Stationary Ginzburg-Landau Superconductivity Model. *Mathematical Methods in the Applied Sciences*, 16:855–875, 1993.

P. G. Ciarlet. *The finite element method for elliptic problems*. SIAM, 2002.

D. Cioranescu, P. Donato and M. P. Roque. *An Introduction to Second Order Partial Differential Equation*. World Scientific, 2018.

M. Cyrot. Ginzburg-Landau theory for superconductors. *Reports on Progress in Physics*, 36(2):103, 1973.

I. Danaila, F. Kaplanski and S. S. Sazhin. *Vortex ring models*. Springer, 2021.

I. Danaila and P. Kazemi. A new Sobolev gradient method for direct minimization of the Gross–Pitaevskii energy with rotation. *SIAM Journal on Scientific Computing*, 32(5):2447–2467, 2010.

P. G. de Gennes. *Superconductivity in Metals and Alloys*. Benjamin, New York, 1966.

B. S. Deaver Jr and W. M. Fairbank. Experimental evidence for quantized flux in superconducting cylinders. *Physical Review Letters*, 7(2):43, 1961.

S. J. Di Bartolo and A. T. Dorsey. Velocity Selection for Propagating Fronts in Superconductors. *Phys. Rev. Lett.*, 77:4442–4445, 1996.

Q. Du. Finite Element Methods for the Time-Dependent Ginzburg-Landau Model of Superconductivity. *Computers Math. Applic.*, 27(12):119–133, 1994a.

Q. Du. Global existence and uniqueness of solutions of the time-dependent ginzburg-landau model for superconductivity. *Applicable Analysis*, 53(1-2):1–17, 1994b.

Q. Du. Numerical approximations of the Ginzburg–Landau models for superconductivity. *Journal of mathematical physics*, 46(9), 2005.

Q. Du, M. D. Gunzburger and J. S. Peterson. Analysis and Approximation of the Ginzburg–Landau Model of Superconductivity. *SIAM Review*, 34(1):54–81, 1992.

Ame en Science. Supraconductivité. 2011. URL `http://www.supraconductivite.fr`.

E. B. Fabes, C. E. Kenig and R. P. Serapioni. The local regularity of solutions of degenerate elliptic equations. *Communications in Statistics-Theory and Methods*, 7(1):77–116, 1982.

R. P. Feynman. *Statistical mechanics: a set of lectures*. Westview press, 1998.

R. P. Feynman, R. B. Leighton, M. Sands et al. *The Feynman lectures on physics*, volume 1. Addison-Wesley Reading, MA, 1971.

M. C. N. Fiolhais and H. Essén. Magnetic field expulsion from an infinite cylindrical superconductor. *Physica C: Superconductivity and its Applications*, 497:54–57, 2014.

J. Fleckinger-Pellé, H. G. Kaper and P. Takác. *Dynamics of the Ginzburg-Landau equations of superconductivity*. Rapport technique, Argonne National Lab.(ANL), Argonne, IL (United States), 1997.

H. Frahm, S. Ullah and A. T. Dorsey. Flux Dynamics and the Growth of the Superconducting Phase. *Physical Review Letters*, 66(23), 1991.

H. Gao. Efficient numerical solution of dynamical Ginzburg-Landau equations under the Lorentz gauge. *Communications in Computational Physics*, 22(1):182–201, 2017.

H. Gao, B. Li and W. Sun. Optimal error estimates of linearized Crank-Nicolson Galerkin FEMs for the time-dependent Ginzburg–Landau equations in superconductivity. *SIAM Journal on Numerical Analysis*, 52(3):1183–1202, 2014.

H. Gao and W. Sun. An efficient fully linearized semi-implicit Galerkin-mixed FEM for the dynamical Ginzburg–Landau equations of superconductivity. *Journal of Computational Physics*, 294:329–345, 2015.

H. Gao and W. Sun. A new mixed formulation and efficient numerical solution of Ginzburg–Landau equations under the temporal gauge. *SIAM Journal on Scientific Computing*, 38(3):A1339–A1357, 2016.

H. Gao and W. Sun. Analysis of linearized Galerkin-mixed FEMs for the time-dependent Ginzburg-Landau equations of superconductivity. *Advances in Computational Mathematics*, 44:923–949, 2018.

H. Gao and W. Xie. A Finite Element Method for the Dynamical Ginzburg–Landau Equations under Coulomb Gauge. *Journal of Scientific Computing*, 97(1):19, 2023.

V. L. Ginzburg and L. D. Landau. On the Theory of superconductivity. *Zh. Eksp. Teor. Fiz.*, 20: 1064–1082, 1950.

L. P. Gorkov. Microscopic derivation of the Ginzburg-Landau equations in the theory of superconductivity. *Sov. Phys. JETP*, 9(6):1364–1367, 1959.

L. P. Gorkov and G. M. Eliashburg. Generalization of the Ginzburg-Landau equations for non-stationary problems in the case of alloys with paramagnetic impurities. *Sov. Phys. (JETP)*, 27(2): 328, 1968.

I. V. Grigorieva, W. Escoffier, J. Richardson, L. Y. Vinnikov, S. Dubonos and V. Oboznov. Direct observation of vortex shells and magic numbers in mesoscopic superconducting disks. *Physical review letters*, 96(7):077005, 2006.

W. D. Gropp, H. G. Kaper, G. K. Leaf, D. L. Levine, M. Palumbo and V. M. Vinokur. Numerical Simulation of Vortex Dynamics in Type-II Superconductors. *Journal of Computational Physics*, 123 (0022):254–266, 1996.

S. Gueron and I. Shafrir. On a discrete variational problem involving interacting particles. *SIAM Journal on Applied Mathematics*, 60(1):1–17, 1999.

F. Hecht. BAMG: bidimensional anisotropic mesh generator. *User Guide. INRIA, Rocquencourt*, 17, 1998.

F. Hecht. New development in FreeFem++. *J. Numer. Math.*, 20(3-4):251–265, 2012. ISSN 1570-2820. URL `https://freefem.org/`.

K. H. Hoffmann and Q. Tang. *Ginzburg-Landau Phase Transition Theory and Superconductivity*. Springer Basel AG, 2001.

Q. Hong, L. Ma, J. Xu and L. Chen. An efficient iterative method for dynamical Ginzburg-Landau equations. *Journal of Computational Physics*, 474:111794, 2023.

R. Huebener. *Magnetic flux structures in superconductors: extended reprint of a classic text*, volume 6. Springer Science & Business Media, 2001.

J. D. Jackson. *Classical electrodynamics*. American Association of Physics Teachers, 1999.

R. Kato, Y. Enomoto and S. Maekawa. Effects of the surface boundary on the magnetization process in type-II superconductors. *Physical Review B*, 47(13), 1993.

P. Kazemi. *A Constructive Method for Finding Critical Point of the Ginzburg-Landau Energy Functional*. Theses, University of North Texas, August 2008.

P. Kazemi and R. J. Renka. Minimization of the Ginzburg–Landau energy functional by a Sobolev gradient trust-region method. *Applied Mathematics and Computation*, 219(11):5936–5942, 2013.

C. Kittel. *Introduction to Solid State Physics. (8th Ed.)*. John Wiley and Sons, 2005.

W. H. Kleiner, L. M. Roth and S. H. Autler. Bulk solution of Ginzburg-Landau equations for type II superconductors: upper critical field region. *Physical Review*, 133(5A):A1226, 1964.

V. G. Kogan and N. Nakagawa. Dissipation of moving vortices in thin films. *Physical Review B*, 105 (2):L020507, 2022.

S. K. Lele. Compact Finite Difference Schemes with Spectral-like Resolution. *Journal Of Computational Physics*, 103:16–42, 1992.

B. Li and Z. Zhang. A new approach for numerical simulation of the time-dependent Ginzburg–Landau equations. *Journal of Computational Physics*, 303:238–250, 2015.

B. Li and Z. Zhang. Mathematical and Numerical Analysis of Time-Dependent Ginzburg–landau Equations in Nonconvex Polygons Based on Hodge Decomposition. *Mathematics of Computation*, 86:1579–1608, 2017.

A. Loseille and F. Alauzet. Continuous mesh framework part II: validations and applications. *SIAM Journal on Numerical Analysis*, 49(1):61–86, 2011.

K. Maki. Motion of the vortex lattice in a dirty type II superconductor. *Journal of Low Temperature Physics*, 1:45–58, 1969.

M. Mu and Y. Huang. An Alternating Crank-Nicolson Method for Decoupling the Ginzburg-Landau Equations. *SIAM Journal on Numerical Analysis*, 35(5):1740–1761, 1998.

J. Neuberger. *Sobolev gradients and differential equations*. Springer Science & Business Media, 2009.

J. W. Neuberger and R. J. Renka. Sobolev Gradients and the Ginzburg–Landau Functional. *SIAM Journal on Scientific Computing*, 20(2):582–590, 1998.

J. W. Neuberger and R. J. Renka. Critical Points of the Ginzburg–Landau Functional on Multiply-Connected Domains. *Experimental Mathematics*, 9(4):523–533, 2000.

J. W. Neuberger and R. J. Renka. Numerical determination of vortices in superconductors: simulation of cooling. *Superconductor Science and Technology*, 16(12):1413, 2003.

H. B. Nielsen and P. Olesen. Vortex-line models for dual strings. *Nuclear Physics B*, 61:45 – 61, 1973.

A. B. Pippard and W. L. Bragg. An experimental and theoretical study of the relation between magnetic field and current in a superconductor. *Proceedings of the Royal Society of London. Series A. Mathematical and Physical Sciences*, 216(1127):547–568, 1953.

L. P. Pitaevskii and S. Stringari. *Bose-Einstein condensation*. Clarendon Press, Oxford, 2003.

R. Prozorov. Meissner-London susceptibility of superconducting right circular cylinders in an axial magnetic field. *Physical Review Applied*, 16(2):024014, 2021.

R. Prozorov and V. G. Kogan. Effective demagnetizing factors of diamagnetic samples of various shapes. *Physical review applied*, 10(1):014030, 2018.

W. B. Richardson, A. L. Pardhanani, G. F. Carey and A. Ardelea. Numerical effects in the simulation of Ginzburg–Landau models for superconductivity. *International Journal for Numerical Methods in Engineering*, 59(9):1251–1272, 2004.

W. Rudin. Real and complex analysis. 1987. *Cited on*, 156:16, 1987.

I. A. Sadovskyy, Y. Jia, M. Leroux, J. Kwon, H. Hu, L. Fang, C. Chaparro, S. Zhu, U. Welp, J.-M. Zuo et al. Toward superconducting critical current by design. *Advanced Materials*, 28(23): 4593–4600, 2016.

I. A. Sadovskyy, A. E. Koshelev, C. L. Phillips, D. A. Karpeyev and A. Glatz. Stable large-scale solver for Ginzburg–Landau equations for superconductors. *Journal of Computational Physics*, 294: 639–654, 2015.

E. Sandier. Lower bounds for the energy of unit vector fields and applications. *Journal of functional analysis*, 152(2):379–403, 1998.

E. Sandier and S. Serfaty. *Vortices in the magnetic Ginzburg-Landau model*, volume 70. Springer Science & Business Media, 2008.

A. Schmid. A time dependent Ginzburg-Landau equation and its application to the problem of resistivity in the mixed state. *Physik der kondensierten Materie*, 5(4):302–317, 1966.

M. P. Sørensen, N. F. Pedersen and M. Ögren. The dynamics of magnetic vortices in type II superconductors with pinning sites studied by the time dependent Ginzburg–Landau model. *Physica C: Superconductivity and its applications*, 533:40–43, 2017.

Q. Tang and S. Wang. Time dependent Ginzburg-Landau equations of superconductivity. *Physica D: Nonlinear Phenomena*, 88(3-4):139–166, 1995.

R. Temam. *Navier-Stokes equations: theory and numerical analysis*, volume 343. American Mathematical Soc., 2001.

D. R. Tilley. Superfluidity and superconductivity. 2019.

M. Tinkham. *Introduction to Superconductivity. (2nd Ed.)*. Dover, 2004.

B. O. Turesson. *Nonlinear potential theory and weighted Sobolev spaces*, volume 1736. Springer Science & Business Media, 2000.

D. Y. Vodolazov, I. L. Maksimov and E. H. Brandt. Vortex entry conditions in type-II superconductors.: Effect of surface defects. *Physica C: Superconductivity*, 384(1-2):211–226, 2003.

R. Willa, A. E. Koshelev, I. A. Sadovskyy and A. Glatz. Strong-pinning regimes by spherical inclusions in anisotropic type-II superconductors. *Superconductor Science and Technology*, 31(1): 014001, 2017.

T. Winiecki and C. S. Adams. A Fast Semi-Implicit Finite-Difference Method for the TDGL Equations. *Journal of Computational Physics*, 179(1):127–139, 2002.

C. Yang. A linearized Crank–Nicolson–Galerkin FEM for the time-dependent Ginzburg–Landau equations under the temporal gauge. *Numerical Methods for Partial Differential Equations*, 30(4):1279–1290, 2014.

E. J. Yarmchuk, M. J. V. Gordon and R. E. Packard. Observation of stationary vortex arrays in rotating superfluid helium. *Physical Review Letters*, 43(3):214, 1979.

W. B. J. Zimmerman. *Multiphysics modeling with finite element methods*, volume 18. World Scientific Publishing Company, 2006.